WP14ER-PR(17) 17915

F van Wyk et al.

Ion-scale turbulence in MAST: anomalous transport, subcritical transitions, and comparison to BES measurements

Preprint of Paper to be submitted for publication in
Plasma Physics and Controlled Fusion

This work has been carried out within the framework of the EUROfusion Consortium and has received funding from the Euratom research and training programme 2014-2018 under grant agreement No 633053. The views and opinions expressed herein do not necessarily reflect those of the European Commission.

Ion-scale turbulence in MAST: anomalous transport, subcritical transitions, and comparison to BES measurements

F. van Wyk*[1,2,3], E. G. Highcock†[1,4], A. R. Field[2], C. M. Roach[2], A. A. Schekochihin‡[1,5], F. I. Parra[1], and W. Dorland[1,6]

[1]Rudolf Peierls Centre for Theoretical Physics, University of Oxford, Oxford OX1 3NP, UK
[2]CCFE, Culham Science Centre, Abingdon OX14 3DB, UK
[3]STFC Daresbury Laboratory, Daresbury WA4 4AD, UK
[4]Chalmers University of Technology, Department of Physics, SE-412 96, Gotëborg, Sweden
[5]Merton College, Oxford OX1 4JD, UK
[6]Department of Physics, University of Maryland, College Park, MD 20742-4111, USA

Abstract

We investigate the effect of varying the ion temperature gradient (ITG) and toroidal equilibrium scale sheared flow on ion-scale turbulence in the outer core of MAST by means of local gyrokinetic simulations. We show that nonlinear simulations reproduce the experimental ion heat flux and that the experimentally measured values of the ITG and the flow shear lie close to the turbulence threshold. We demonstrate that the system is subcritical in the presence of flow shear, i.e., the system is formally stable to small perturbations, but transitions to a turbulent state given a large enough initial perturbation. We propose that the transition to subcritical turbulence occurs via an intermediate state dominated by low number of coherent long-lived structures, close to threshold, which increase in number as the system is taken away from the threshold into the more strongly turbulent regime, until they fill the domain and a more conventional turbulence emerges. We show that the properties of turbulence are effectively functions of the distance to threshold, as quantified by the ion heat flux. We make quantitative comparisons of correlation lengths, times, and amplitudes between our simulations and experimental measurements using the MAST BES diagnostic. We find reasonable agreement of the correlation properties, most notably of the correlation time, for which significant discrepancies were found in previous numerical studies of MAST turbulence.

*ferdinand.vanwyk@physics.ox.ac.uk
†highcock@chalmers.se
‡alex.schekochihin@physics.ox.ac.uk

1 Introduction

Understanding and controlling turbulence is crucial to the realisation of fusion as an energy source [1]. Numerical studies of turbulence in the Mega Ampere Spherical Tokamak (MAST) [2, 3] have found that ion-scale turbulence can be driven by a combination of the ion temperature gradient (ITG) $\kappa_T = -\,\mathrm{d}\ln T_i/\mathrm{d}r$ (T_i is the ion temperature and r is a dimensionless radial coordinate defined later), which drives the well-known ITG instability [4, 5], and the electron temperature and density gradients, which drive the trapped-electron-mode (TEM) instability [6]. In this work, we will focus on the nature of turbulence caused by the combination of these two drives. As well as being affected by the profiles of temperatures and densities, the turbulence can also be affected by the profile of the toroidal rotation, which is driven by the neutral beam injection (NBI) heating system [3]. The plasma flow associated with toroidal rotation, which is sheared, has components both parallel and perpendicular to the direction of the magnetic field. Perpendicular flow shear, quantified by $\gamma_E = (r/q)\,\mathrm{d}\omega/\mathrm{d}r\ \ (a/v_{\mathrm{th}i})$ (q is the safety factor, ω is the frequency of toroidal rotation, a is the minor radius of the device, $v_{\mathrm{th}i} = \sqrt{2T_i/m_i}$ is the thermal velocity, and m_i is the ion mass), has been shown to reduce, or even eliminate, turbulence in tokamaks [7]. Parallel flow shear has also been shown to drive a linear instability [8], which can increase the level of turbulence, although, at the levels of flow shear considered in this work, we do not expect the destabilising effect of the parallel flow shear to be significant. Thus, there is a competition in fusion plasmas between the destabilising effects of ITG and the parallel flow shear, and the stabilising effect of the perpendicular flow shear.

It has been shown that perpendicular flow shear can render the plasma completely linearly stable [9]. However, this may still entail substantial transient growth of perturbations and, given a large enough initial perturbation, can lead to a saturated nonlinear state – a phenomenon known as "subcritical" turbulence [2, 10, 11, 12, 13]. We have previously studied this transition to subcritical turbulence in Ref. [14], and proposed the following transition scenario: close to the turbulence threshold, the nonlinear state is dominated by coherent, long-lived structures; as the system is taken away from the threshold, the number of these structures increases until they fill the simulation domain and a conventional turbulent state is recovered. In this paper, we will present a more comprehensive view of the changes in turbulence that occur as the system is taken away from the threshold, including analysis of the turbulence structure and detailed comparisons with experimental measurements.

At the temperatures and densities found in fusion experiments such as MAST, it can be shown that the conditions for a fluid description are rarely satisfied and that a kinetic description must be used. Gyrokinetics [15, 16, 17] has emerged as the most appropriate first-principles description in the context of plasma turbulence in the core of tokamaks. In this paper, we use the local gyrokinetic code GS2[1] [18, 19] to solve the gyrokinetic equation. GS2 includes a large number of physical effects relevant to experimental plasmas, such as realistic magnetic-surface geometries, arbitrary numbers of kinetic species, realistic Fokker-Planck collision operators, and so on. This has allowed simulations of sufficient realism to be compared quantitatively to experimental measurements. Local gyrokinetic codes, such as GS2, take as input the values and first derivatives of equilibrium quantities at a particular

[1] `http://gyrokinetics.sourceforge.net`

radial location and predict a host of quantities that could theoretically be measured by an experimental diagnostic, for example, the flux of particles, momentum, and heat, or, indeed, the full density and temperature fluctuation fields.

In conjunction with increasingly realistic modelling, more sophisticated diagnostic techniques have been developed, which aid in our understanding of the conditions inside the reactor and allow us to make comparisons with modelling results. The beam-emission-spectroscopy (BES) diagnostic in MAST is one such diagnostic that measures ion-scale density fluctuations [20, 21]. More specifically, the BES diagnostic infers ion-scale density fluctuations from D_α emission (the emission of light resulting from the dominant (n=3-2) visible transition of ionised deuterium), which is generated as a result of the injection of neutral particles by the NBI system. The BES diagnostic takes measurements in a two-dimensional radial-poloidal plane. From the BES measurements, it is possible to estimate a number of useful correlation properties of the turbulence: the correlation time τ_c, via the cross-correlation time delay (CCTD) method [22, 23, 24]; the radial and poloidal correlation lengths l_R and l_Z; and the relative density-fluctuation field $\delta n_i/n_i$ [25, 24]. Measurements of fluctuating quantities allow more extensive quantitative comparisons between experiment and simulations. However, meaningful comparisons are only possible via the use of "synthetic diagnostics" that take account of the measurement characteristics of the particular diagnostic and modify the simulation output accordingly [23, 26, 24].

A recent experimental study [26] of MAST turbulence used the BES diagnostic to measure turbulent density fluctuations in the outer core of an L-mode plasma and compared their correlation properties with those inferred from global gyrokinetic simulations. While there was some agreement at mid-radii, significant discrepancies were found in the ion heat flux and turbulence correlation time at outer radii, where ITG-driven turbulence may not be fully suppressed by flow shear. Previous gyrokinetic modelling of similar MAST L-mode plasmas showed that electron-scale turbulence can play a relatively significant role [2, 3]. In this work, we assume that ion-scale turbulence dominates, and we use high-resolution local gyrokinetic simulations to study such turbulence in the outer core of the MAST discharge considered in [26]. We shall see that local gyrokinetic modelling does produce turbulent fluctuations whose correlation properties are consistent with experimental measurements.

In simulating experimentally relevant plasmas using gyrokinetic codes, we aim to achieve the following. First, we want to understand better the physical mechanisms that most strongly influence turbulence and the associated enhanced transport. Specifically, we wish to know how turbulence characteristics (such as transport, spatial scales, time scales, etc.) change in the outer core of MAST with the equilibrium parameters κ_T and γ_E. Secondly, in light of newly available experimental data from the MAST BES diagnostic [26], we want to establish whether the turbulence characteristics found in local gyrokinetic GS2 simulations agree with experimental BES measurements within the experimental uncertainties in measurements of the ITG and flow shear. Such quantitative comparisons with experimental results are essential in developing confidence in our theoretical models and numerical implementations. In understanding the properties of turbulence, we ultimately aim to guide the optimisation and design of future experiments and fusion reactors by acquiring the ability to predict and control the turbulence.

The rest of this paper is organised as follows. In section 2, we give an overview of the MAST discharge that we will be considering, as well as of gyrokinetics and of the numerical tools that we will use for our study. Our main results are split into two sections.

In section 3, we study numerically the effect on turbulence in MAST of changing κ_T and γ_E by performing a two-dimensional parameter scan in these two equilibrium parameters. We map out the turbulence threshold and show that the experimentally measured ion heat flux is close to the numerical values found near this threshold, thus suggesting that the turbulence in MAST is near-marginal (section 3.1). We demonstrate that the turbulence is subcritical (section 3.2), with large initial perturbations required to ignite it (a phenomenon not previously observed for an experimentally relevant plasma) and estimate the conditions necessary for the onset of turbulence. We then show that the near-threshold state is one dominated by long-lived, coherent structures, which exist against a background of much smaller fluctuations (section 3.3). These structures are shown to be regions of increased density, radial flow, and temperature fluctuations. Sufficiently far from the turbulence threshold in parameter space, we recover a more conventional turbulent state consisting of many strongly interacting eddies while being sheared apart by the perpendicular flow shear. We demonstrate that many of the properties of the system (e.g. the number of structures, their amplitude, shear due to zonal flows, etc.) are effectively functions only of the distance from the turbulence threshold, as quantified by the ion heat flux.

In section 4, we make comparisons with experimental measurements from the BES diagnostic. We present two types of correlation analysis of our simulations: of the numerical data processed through a synthetic diagnostic (section 4.3) and of raw GS2 data, with no modelling of the diagnostic (section 4.4). We show that there is reasonable agreement with experimental measurements in the case of the analysis with the synthetic diagnostic. However, radial correlation lengths predicted by GS2 are shown to be below the resolution threshold of the BES diagnostic in MAST (an issue discussed in detail in [24]). This conclusion stems from studying correlation parameters of the raw GS2 density fluctuations and suggests that care must be taken when interpreting BES measurements. Comparison between results of analysis with and without the synthetic diagnostic shows that the synthetic diagnostic has a measurable effect on several turbulence characteristics, including the poloidal correlation length and the fluctuation amplitude, consistent with the conclusions of Ref. [24]. Finally, we present the correlation lengths and times as functions of the ion heat flux and again show that the structure of the turbulence in our simulations is effectively only a function of this parameter, which measures the distance to the turbulence threshold.

2 Experimental and numerical details

2.1 MAST discharge #27274

MAST is a medium-sized, low-aspect-ratio (≈ 1.5) tokamak with a major radius $R_0 \approx 0.9$ m and a minor radius $a \approx 0.6$ m. In this work, we will focus on the MAST discharge #27274, one of a set of three nominally identical experiments (i.e. having identical profiles and equilibria) previously reported in [26] and differing only in the radial viewing location of the BES system. These three discharges were #27272, #27268, and #27274, wherein the centre of the BES was located at 1.05 m, 1.2 m, and 1.35 m, respectively. The MAST BES diagnostic [20, 21] observes an area of approximately 16×8 cm^2 in the radial and poloidal directions, respectively, corresponding approximately to one third of the minor radius of the plasma. Thus, the combination of these three discharges provided a complete radial profile of BES measurements on the outboard side of the plasma.

Each discharge produced an L-mode plasma with strong toroidal rotation and, therefore, with mean flow shear perpendicular and parallel to the magnetic field [26]. Previous investigations of MAST turbulence for similar configurations [2, 3] found that ion-scale turbulence is suppressed in the core region by strong flow shear. However, the flow shear is weaker in the outer-core region, where ITG modes are not completely suppressed, making it possible to study ion-scale turbulence. In this work, we will restrict our attention to the time window $t = 0.250 \pm 0.002$ s and the radial location[2] $r = D/2a = 0.8$ ($\equiv r_0$) of discharge #27274, where D is the diameter of the flux surface and a is the half diameter of the last closed flux surface (LCFS), both measured at the height of the magnetic axis. Importantly, there is no large-scale and disruptive magnetohydrodynamic (MHD) activity at this time and radial location [26]; such activity would interfere with the quality of BES measurements. The normalized radial location $r = 0.8$ corresponds to a major radius of approximately 1.32 m and, therefore, falls within the viewing area covered by discharge #27274 [see figure 1(b)].

2.2 Equilibrium profiles

MAST has a range of diagnostics that allow us to extract the equilibrium parameters required to conduct a numerical transport study. The ion temperature, T_i, and toroidal flow velocity, $u_\phi = R\omega$, where ω is the toroidal angular rotation frequency, were obtained from charge-exchange-recombination spectroscopy (CXRS) measurements of C^{+6} impurity ions with a spatial resolution of ~ 1 cm [28]. The electron density, n_e, and temperature, T_e, were obtained from a Thomson-scattering diagnostic [29] with resolution comparable to the CXRS system. These measured profiles were mapped onto flux-surface coordinates by the pre-processing code MC^3 using a motional-Stark-effect-constrained EFIT equilibrium [30]. These equilibrium profiles served as input to the transport analysis code TRANSP[3] [31], which calculates the transport coefficients of particles, momentum, and heat. Figure 1(a) shows a three-dimensional view of the axisymmetric nested flux surfaces and figure 1(b) shows the poloidal cross-section of the flux surfaces extracted from an EFIT equilibrium. The $r = 0.8$ surface is highlighted in both plots. The measurement window of the BES diagnostic for discharge #27274 is also shown in figure 1(b). The chosen flux surface at $r = 0.8$ intersects the measurement window at the outboard midplane, allowing comparisons of turbulence characteristics between our numerical predictions of turbulence and experimental measurements.

The important experimental quantities needed to conduct a numerical study are the

[2] We use $r = D/2a$ as the definition of the radial location because it corresponds to the radial coordinate used by the Miller specification of the flux-surface geometry [27]. In terms of other commonly used radial coordinates, $r = 0.8$ corresponds to $\rho_{\mathrm{tor}} = \sqrt{\psi_{\mathrm{tor}}/\psi_{\mathrm{tor,LCFS}}} = 0.7$ and $\rho_{\mathrm{pol}} = \sqrt{\psi_{\mathrm{pol}}/\psi_{\mathrm{pol,LCFS}}} = 0.87$, where $\psi_{\mathrm{tor}} = (1/2\pi)^2 \int_0^V dV \boldsymbol{B} \cdot \nabla\phi$ is the toroidal magnetic flux, V is the volume enclosed by the flux surface, $\boldsymbol{B}$ is the magnetic field, ϕ is the toroidal angle, and $\psi_{\mathrm{tor,LCFS}}$ is the toroidal flux enclosed by the last closed flux surface [see figure 1(b)], $\psi_{\mathrm{pol}} = (1/2\pi)^2 \int_0^V dV \boldsymbol{B} \cdot \nabla\theta$ is the poloidal magnetic flux, θ is the poloidal angle, and $\psi_{\mathrm{pol,LCFS}}$ is the poloidal flux enclosed by the LCFS.

[3] `http://w3.pppl.gov/transp/`

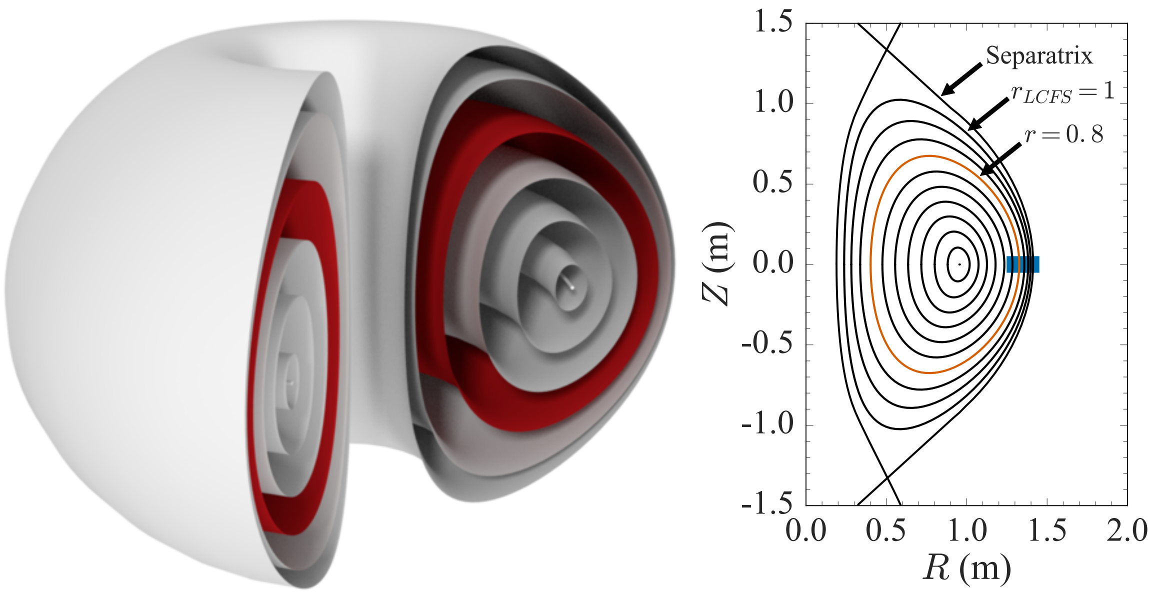

(a) (b)

Figure 1: (a) A three-dimensional view of the nested flux surfaces. (b) The poloidal cross-section of the magnetic geometry along with the LCFS and the separatrix, which separates closed field lines from open ones. The flux surface of interest is at $r = 0.8$, shown in red. It was chosen so that this surface intersects the BES measurement plane for discharge #27274 (blue shaded region).

radial profiles of T_i, T_e, n_i (the ion density), n_e, and ω. There are no direct measurements of n_i in MAST, but we assume that it is equal to n_e, as measured by the Thomson-scattering diagnostic, due to quasineutrality (in MAST, we typically have an effective ion charge $Z_{\text{eff}} \lesssim 1.5$). To conduct a numerical study of turbulence at $r = 0.8$ (using the local formulation of gyrokinetics; see section 2.3), we need the equilibrium quantities listed above and their first derivatives (gradient length scales). The (normalised) gradient length scales of T_i, T_e, and n_e, and flow shear (gradient of ω) are, by definition,

$$\frac{1}{L_{Ti}} = -\frac{\mathrm{d}\ln T_i}{\mathrm{d}r} \equiv \kappa_T, \tag{1}$$

$$\frac{1}{L_{Te}} = -\frac{\mathrm{d}\ln T_e}{\mathrm{d}r}, \tag{2}$$

$$\frac{1}{L_{ne}} = -\frac{\mathrm{d}\ln n_e}{\mathrm{d}r}, \tag{3}$$

$$\text{and} \qquad \gamma_E = \frac{r_0}{q_0}\frac{\mathrm{d}\omega}{\mathrm{d}r}\frac{a}{v_{\mathrm{th}i}}, \tag{4}$$

where $q(\psi) = \partial\psi_{\text{tor}}/\partial\psi_{\text{pol}}$ is the safety factor and q_0 is its value at r_0. The flow-shear parameter γ_E can be interpreted as the (non-dimensionalised) shear of the component of the toroidal rotation that is perpendicular to the local magnetic field.

The left-hand column of figure 2 shows the radial profiles of T_i, T_e, n_e, and ω as functions of r. The gradient scale lengths (1)–(3) and flow shear (4) are plotted as functions of r in the right-hand column in figure 2. The dashed lines indicate $r = 0.8$. The profiles in figure 2 represent a 20-ms time average around $t = 0.25$ s and the shaded areas indicate the standard deviations. The nominal experimental values of the quantities that we will vary in this study are $\kappa_T = 5.1 \pm 1$ and $\gamma_E = 0.16 \pm 0.02$.

The profile of the ion heat flux Q_i^{exp} was calculated by using the equilibrium profiles and magnetic geometry as input to a TRANSP analysis, which calculated Q_i^{exp} as a function of r by equating it to the net deposited power within the flux surface labelled by r. The profile of Q_i^{exp} as a function of r is shown in figure 3. In this work, we normalise the heat flux to the gyro-Bohm value defined by

$$Q_{\mathrm{gB}} = n_i T_i v_{\mathrm{th}i} \frac{\rho_i^2}{a^2}. \tag{5}$$

The experimental level of heat flux at $r = 0.8$ is $Q_i^{\mathrm{exp}}/Q_{\mathrm{gB}} = 2 \pm 1$.

2.3 Local gyrokinetic description

We model the turbulence in MAST using gyrokinetic theory [15, 16, 17]. For a detailed review, the reader is referred to [17] and references therein, while only a brief overview is given here. The gyrokinetic equation describes the evolution of the non-Boltzmann part of the perturbed (from a background Maxwellian F_s) particle distribution function, $h_s(t, \boldsymbol{R}_s, \varepsilon_s, \mu_s, \sigma)$, of a species s, where $\boldsymbol{R}_s$ is the guiding-centre coordinate, ε_s is the particle energy, μ_s is the magnetic moment of species s, and σ is the sign of the (peculiar) parallel velocity $v_\parallel$. The gyrokinetic equation is[4]

$$\begin{aligned}\left(\frac{\partial}{\partial t} + \boldsymbol{u}\cdot\nabla\right)\left(h_s - \frac{Z_s e \langle\varphi\rangle_{\boldsymbol{R}_s}}{T_s} F_s\right) + \left(v_\parallel \boldsymbol{b} + \boldsymbol{V}_{\mathrm{D}s} + \langle \boldsymbol{V}_E\rangle_{\boldsymbol{R}_s}\right)\cdot\nabla h_s - \langle C[h_s]\rangle_{\boldsymbol{R}_s} \\ = -\langle \boldsymbol{V}_E\rangle_{\boldsymbol{R}_s}\cdot\nabla r\left[\frac{\mathrm{d}\ln n_s}{\mathrm{d}r} + \left(\frac{\varepsilon_s}{T_s} - \frac{3}{2}\right)\frac{\mathrm{d}\ln T_s}{\mathrm{d}r} + \frac{m_s v_\parallel}{T_s}\frac{R B_\phi}{B}\frac{\mathrm{d}\omega}{\mathrm{d}r}\right] F_s,\end{aligned} \tag{6}$$

where $\boldsymbol{u} = \omega(r) R^2 \nabla\phi$ is the toroidal rotation velocity, $\omega(r)$ is the toroidal angular frequency, ϕ is the toroidal angle, φ is the electrostatic potential perturbation, $\langle \ldots \rangle_{\boldsymbol{R}_s}$ is an average over the particle orbit at constant $\boldsymbol{R}_s$, $F_s = n_s(r)[m_s/2\pi T_s(r)]^{3/2} e^{-\varepsilon_s/T_s(r)}$ is the background Maxwellian, $\boldsymbol{V}_{\mathrm{D}s} = (c/Z_s e B)\boldsymbol{b}\times\left[m_s v_\parallel^2 \boldsymbol{b}\cdot\nabla\boldsymbol{b} + \mu\nabla B\right]$ is the magnetic drift velocity,

$$\boldsymbol{V}_E = \frac{c}{B}\boldsymbol{b}\times\nabla\varphi \tag{7}$$

is the $\boldsymbol{E}\times\boldsymbol{B}$ drift velocity, $C[h_s]$ is the linearised collision operator [32, 33], and B_ϕ is the toroidal component of the magnetic field.

[4]The equilibrium quantities n_s, T_s, and ω are functions only of the poloidal magnetic flux ψ. For the purposes of this work, we have converted this dependence from ψ to the Miller coordinate $r = D/2a$ introduced previously. Since r is also a flux-surface label, we can use the following equation to relate gradients in ψ and r: $\nabla r = \mathrm{d}r/\mathrm{d}\psi\ \nabla\psi$.

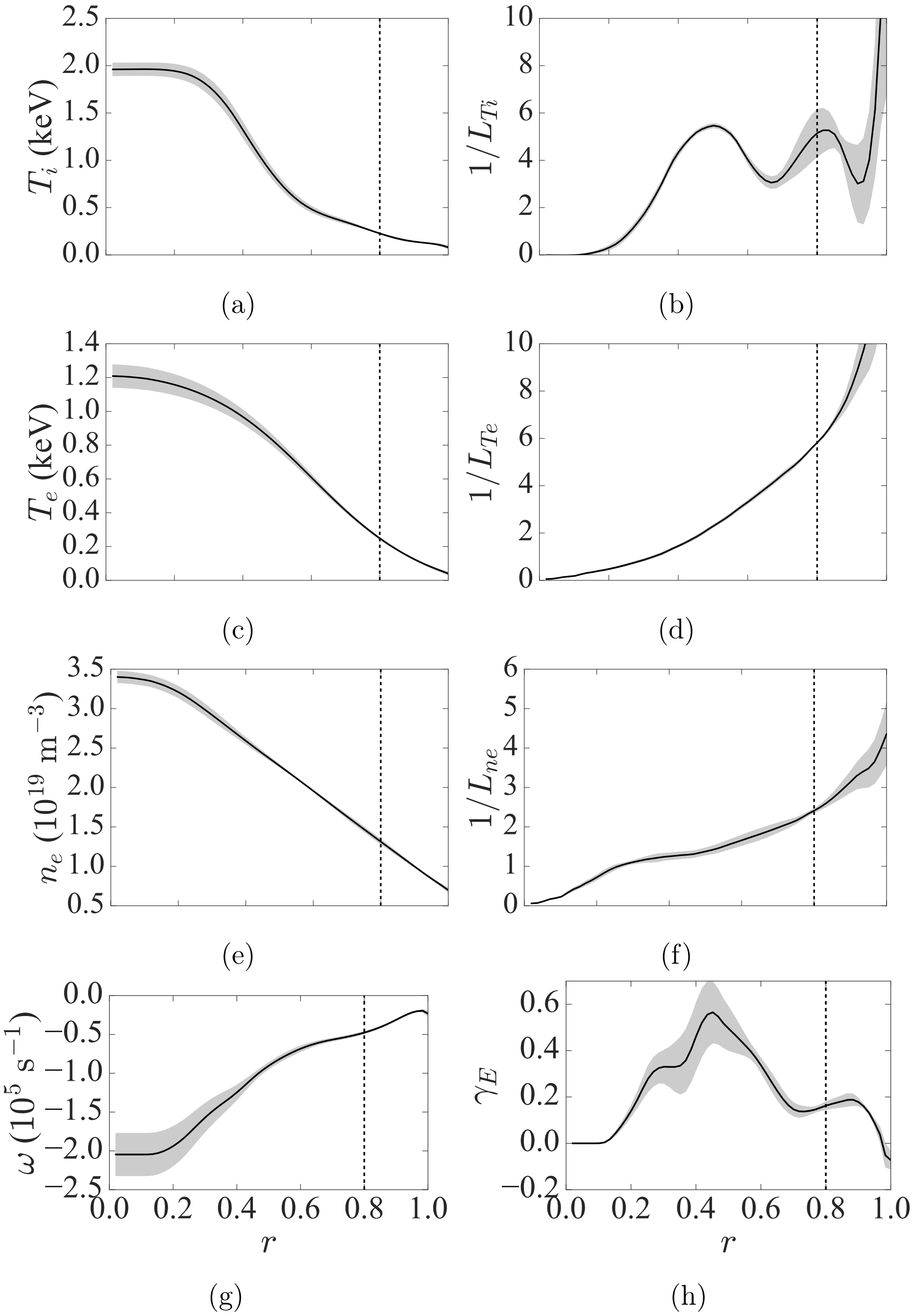

Figure 2: Radial profile measurements from MAST discharge #27274 of (a) the ion temperature, T_i, (b) the ion temperature gradient, $1/L_{Ti}$, calculated using (1), (c) the electron temperature, T_e, (d) the electron temperature gradient, $1/L_{Te}$, calculated using (2), (e) the electron density, n_e, (f) the electron density gradient, $1/L_{ne}$, calculated using (3), (g) the toroidal angular frequency, ω, and (h) the flow shear, γ_E, calculated using (4). The dashed line in each plot indicates $r = 0.8$ and the shaded regions indicate the standard deviation of the profiles over a 20-ms time window around $t = 0.25$ s.

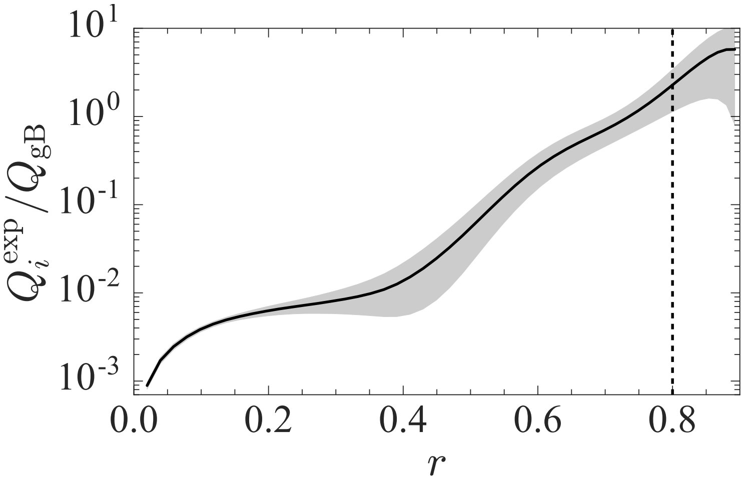

Figure 3: Experimental ion heat flux as a function of r determined from power balance by TRANSP analysis. The dashed line indicates $r = 0.8$ and the shaded region indicates the uncertainty estimated by TRANSP.

To close our system of equations we use the quasineutrality condition

$$\sum_s Z_s \delta n_s = 0 \quad \Rightarrow \quad \sum_s \frac{Z_s^2 e\varphi}{T_s} n_s = \sum_s Z_s \int d^3\boldsymbol{v}\, \langle h_s \rangle_{\boldsymbol{r}}\,, \tag{8}$$

where $\langle \ldots \rangle_{\boldsymbol{r}}$ indicates a gyroaverage at constant particle position $\boldsymbol{r}$, to calculate φ using h_s.

In adopting equations (6) and (8) we have formally assumed that the Mach number M of the plasma rotation is small, but that the flow shear is large enough to affect the plasma dynamics:

$$\frac{R\omega}{v_{\mathrm{th}i}} = M \ll 1, \quad |a\nabla \ln \omega| \sim \frac{1}{M}. \tag{9}$$

This allows us to formulate local gyrokinetics in a rotating surface, neglecting effects such as the Coriolis and centrifugal force, but retaining the effect of flow shear [17]. We have also assumed that the fluctuations are purely electrostatic, i.e., there are no fluctuating magnetic fields.

2.4 Numerical set-up

In this work, we have used the local gyrokinetic code GS2[5] [18, 19, 34] to solve the system of equations (6) and (8) to give us the time evolution of h_s and φ. GS2 solves the gyrokinetic equation in a region known as a "flux tube", shown in figure 4. The GS2 flux tube follows a central magnetic field line once around in the poloidal direction (represented in figure 4 by the field line highlighted in red).

The MAST local equilibrium parameters used in our simulations, extracted from the MAST diagnostics and EFIT equilibrium, are given in table 1. We have included electrons in our simulations as a kinetic species. Our GS2 simulations had resolution of $85 \times 32 \times 20$

[5] `http://gyrokinetics.sourceforge.net`

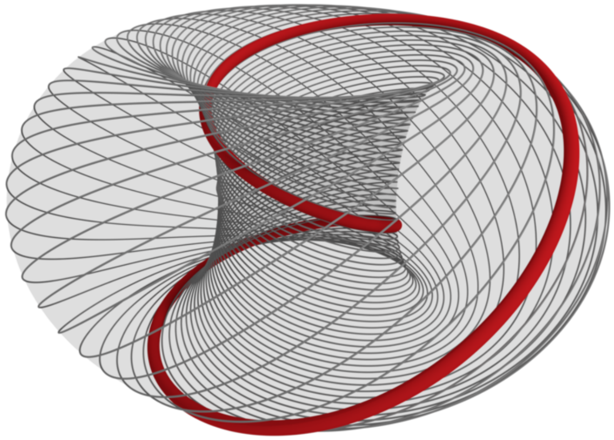

Figure 4: Magnetic field lines that lie on the flux surface at $r = 0.8$ (setting $q = 2$ for visualisation purposes, so that field lines are closed). The field line marked in red is the centre line of the GS2 flux tube that we use as the simulation domain. The flux tube follows the field line once around the flux surface in the poloidal direction.

grid points in the radial $\times$ binormal $\times$ parallel directions, and 27×16 pitch-angle $\times$ energy-grid points, respectively. The corresponding box sizes were $L_x \approx 200\rho_i$ in the radial direction (with maximum wavenumber $k_{x,\max}\rho_i \simeq 1.3$) and $L_y \approx 62\rho_i$ in the binormal direction (with maximum wavenumber $k_{y,\max}\rho_i \simeq 3$). We note that the radial box size is larger than the minor radius of MAST, however, this is required to achieve sufficient k_x resolution to resolve the effect of the flow shear (see appendix D). Artificial numerical dissipation was used to damp electron modes at small scales.

GS2 solves (6) for h_s, from which one can calculate a range of physical characteristics of the turbulence, e.g., the density-, flow-, temperature-fluctuation fields, as well as particle, momentum, and heat fluxes, and so on. Of particular importance in this work are the ion density fluctuation field,

$$\frac{\delta n_i}{n_i} = \frac{1}{n_i} \int \mathrm{d}^3\boldsymbol{v} \, \langle h_i \rangle_{\boldsymbol{r}} \,, \tag{10}$$

where $\delta n_i / n_i$ is an order-unity quantity, and the radially outward, time-averaged turbulent heat flux carried by the ions,

$$Q_i = \left\langle \frac{1}{V} \int \mathrm{d}^3\boldsymbol{r} \int \mathrm{d}^3\boldsymbol{v} \frac{m_i v^2}{2} h_i \boldsymbol{V}_E \cdot \nabla r \right\rangle_{\mathrm{fs}}, \tag{11}$$

where V is the volume of the flux tube and $\langle \ldots \rangle_{\mathrm{fs}}$ denotes a flux-surface average. The heat flux Q_i can be normalised to the gyro-Bohm heat flux given by (5).

3 Numerical results

In this section, we present the results of a two-dimensional scan in the two local equilibrium parameters, κ_T and γ_E, that have been identified to have a strong effect on the properties of the turbulence. We demonstrate that GS2 simulations are able to match the experimental

Table 1: GS2 equilibrium parameters calculated from diagnostic measurements and from the EFIT equilibrium of the MAST discharge #27274 and appropriately normalised. The nominal experimental values for κ_T and γ_E are $\kappa_T = 5.1 \pm 1$ and $\gamma_E = 0.16 \pm 0.02$. The reference magnetic field is the toroidal magnetic field strength at the magnetic axis, i.e., $B_{\text{ref}} = B_\phi(r = 0)$.

Quantity	GS2 variable	Value
$\beta = 8\pi n_i T_i / B_{\text{ref}}^2$	`beta`	0.0047
$\beta' = \partial\beta/\partial r$	`beta_prime_input`	-0.12
Eff. ion charge for collisions $Z_{\text{eff}} = \sum_i n_i Z_i^2 / \lvert \sum_i n_i Z_i \rvert$	`zeff`	1.59
Elec.-ion collisionality ν_{ei}	`vnewk_2`	0.59
Elec. density $n_{eN} = n_e/n_i$	`dens_2`	1.00
Elec. density grad. $1/L_{ne} = -\,\mathrm{d}\ln n_e/\mathrm{d}r$	`fprim_2`	2.64
Elec. mass $m_{eN} = m_e/m_i$	`mass_2`	$1/(2 \times 1836)$
Elec. temp. $T_{eN} = T_e/T_i$	`temp_2`	1.09
Elec. temp. grad. $1/L_{Te} = -\,\mathrm{d}\ln T_e/\mathrm{d}r$	`tprim_2`	5.77
Elongation κ	`akappa`	1.46
Elongation derivative $\kappa' = \mathrm{d}\kappa/\mathrm{d}r$	`akappri`	0.45
Flow shear $\gamma_E = (r_0/q_0)\,\mathrm{d}\omega/\mathrm{d}r\ (a/v_{\text{th}i})$	`g_exb`	[0, 0.19]
Ion collisionality ν_i	`vnewk_1`	0.02
Ion density $n_{iN} = n_i/n_i$	`dens_1`	1.00
Ion density grad. $1/L_{ni} = -\,\mathrm{d}\ln n_i/\mathrm{d}r$	`fprim_1`	2.64
Ion mass $m_{iN} = m_i/m_i$	`mass_1`	1.00
Ion temp. $T_{iN} = T_i/T_i$	`temp_1`	1.00
Ion temp. grad. $\kappa_T \equiv 1/L_{Ti} = -\,\mathrm{d}\ln T_i/\mathrm{d}r$	`tprim_1`	[4.3, 8.0]
Magnetic field reference point R_{geo}	`r_geo`	1.64
Magnetic shear $\hat{s} = r/q\ \mathrm{d}q/\mathrm{d}r$	`s_hat_input`	4.00
Major radius $R_N = R/a$	`rmaj`	1.49
Miller radial coordinate $r = D/2a$	`rhoc`	0.80
Safety factor $q = \partial\psi_{\text{tor}}/\partial\psi_{\text{pol}}$	`qinp`	2.31
Shafranov Shift $1/a\ \mathrm{d}R/\mathrm{d}r$	`shift`	-0.31
Triangularity δ	`tri`	0.21
Triangularity derivative $\delta' = \mathrm{d}\delta/\mathrm{d}r$	`tripri`	0.46

heat flux at equilibrium-parameter values within the experimental uncertainty and that the experiment lies close to the turbulence threshold (section 3.1). We find that the turbulence is subcritical, meaning that it can be sustained in the absence of linearly growing eigenmodes: it is driven instead by transiently growing modes, provided the transient growth is sufficient and the initial amplitudes are large enough (section 3.2). We study the linear dynamics and estimate the conditions necessary to ignite turbulence, namely the transient amplification factor and time. Studying the real-space structure of turbulence (section 3.3), we detect coherent, long-lived structures close to marginality, and summarise a novel structure-counting analysis of these previously presented in [14]. Moving away from the turbulence threshold into more strongly-driven regimes, the number of turbulent structures increases rapidly. Far from the turbulence threshold, the turbulence is similar to what is encountered in the absence of flow shear, characterised by many interacting eddies. We estimate the $\boldsymbol{E} \times \boldsymbol{B}$ shear due to the zonal flows (section 3.3.5) and show that it is small compared to the background flow shear close to the turbulence threshold, but becomes comparable to, and eventually dominates over, the flow shear far from the threshold, resembling a system in the absence of flow shear. This suggests that the observed nonlinear state dominated by coherent structures is an intermediate state between completely suppressed turbulence and the zonal-flow regulated scenarios observed in conventional ITG-unstable plasmas [35].

3.1 Heat flux

A scan was performed in the parameters κ_T and γ_E to investigate the dependence of turbulent transport on them. The experimental values and associated measurement uncertainties were $\kappa_T = 5.1 \pm 1$ and $\gamma_E = 0.16 \pm 0.02$. Because of the presence of these uncertainties and of the sensitive dependence of the heat flux on κ_T and γ_E, it was necessary to cover a range of their values even just to have a meaningful comparison with the experiment. We also performed simulations outside the experimental uncertainty ranges to aid our understanding of how the nature of the turbulence changes with κ_T and γ_E and, in particular, how it is different near to, versus far from, the (nonlinear) stability threshold. Our entire study covered $\kappa_T \in [3.0, 8.0]$ and $\gamma_E \in [0, 0.19]$ and consisted of 76 simulations (see Appendix A for a table of the parameter values). All simulations were run until they reached a statistical steady state, i.e., until the running time average became independent of time. Averages were taken typically over a time period of approximately 200–400 $(a/v_{\mathrm{th}i})$, which corresponds to $\sim$ 800–1600 μs, but in many cases longer.

Figure 5 shows the turbulent ion heat flux versus κ_T and γ_E found in our simulations. Figure 5(a) shows the full parameter scan with the rectangular region indicating the extent of the experimental errors in the equilibrium parameters. The dashed line indicates the value of experimental heat flux, $Q_i^{\mathrm{exp}}/Q_{\mathrm{gB}}$, and the shaded region the experimental uncertainty in its determination. This figure demonstrates two key conclusions of this work: (i) GS2 is able to match the experimental heat flux within the experimental uncertainties of κ_T and γ_E, and (ii) the experimental regime is located close to the turbulence threshold (defined as the separating line between the regions of parameter space with $Q_i = 0$ and $Q_i > 0$).

Figure 5(b) shows Q_i/Q_{gB} as a function of κ_T strictly within the region of measurement uncertainty of κ_T and γ_E, close to the turbulence threshold. The dashed line and shaded region indicate $Q_i^{\mathrm{exp}}/Q_{\mathrm{gB}}$ and its associated uncertainty. We see that there is a range of κ_T and γ_E values where we might expect Q_i/Q_{gB} to match $Q_i^{\mathrm{exp}}/Q_{\mathrm{gB}}$. From this figure, we can also identify several simulations that represent the marginally unstable cases in our parameter scan: $(\kappa_T, \gamma_E) = (4.4, 0.14), (4.8, 0.16), (5.1, 0.18)$. We will consider these parameter values section 3.2, when studying the conditions necessary to reach a saturated turbulent state. Furthermore, we have a number of individual simulations that match the value of $Q_i^{\mathrm{exp}}/Q_{\mathrm{gB}}$. A list of these is given in table 2. We will investigate these simulations further when we make more detailed comparisons with the experiment, in section 4.

Figure 6(a) shows the values of Q_i/Q_{gB} from figure 5(a) for several values of γ_E as a function of κ_T, whereas figure 6(b) shows Q_i/Q_{gB} as a function of γ_E for several values of κ_T. We see that an $O(1)$ change in κ_T gives rise to an $O(10)$ change in Q_i/Q_{gB}, and even more dramatically for changes in γ_E, which requires only an $O(0.1)$ change to cause $O(10)$ changes in the ion heat flux. An important conclusion from this figure is that the presence of flow shear does not significantly affect the stiffness of the transport, i.e., the rate of increase of Q_i/Q_{gB} with respect to κ_T, but only changes the threshold value of κ_T above which turbulence is present. This increase in critical ITG without a change in the

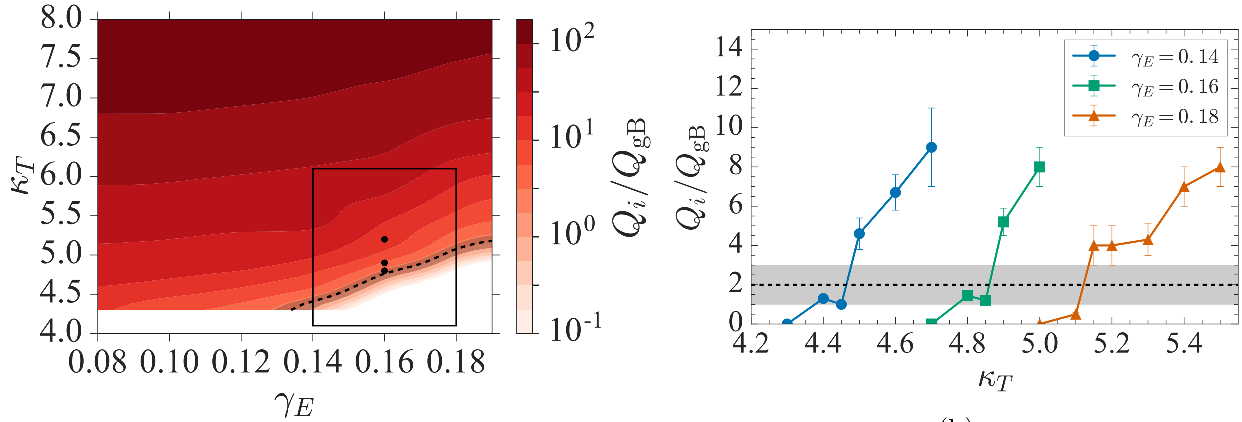

(a) (b)

Figure 5: (a) Ion heat flux $Q_i/Q_{\rm gB}$ as a function of κ_T and γ_E for all simulations with $\gamma_E > 0$. The rectangular region indicates the range in κ_T and γ_E consistent with the experiment and measurement uncertainties. The dashed line indicates the value of $Q_i^{\rm exp}/Q_{\rm gB}$ and the shaded area the experimental uncertainty. The experiment is clearly near the turbulence threshold defined by (κ_T, γ_E). The points indicate the parameter values for which the density-fluctuation fields are shown in figure 12. (b) $Q_i/Q_{\rm gB}$ as a function of κ_T strictly within experimental uncertainty of κ_T and γ_E, and close to the turbulence threshold. The shaded region indicates the experimental heat flux $Q_i^{\rm exp}/Q_{\rm gB} = 2 \pm 1$, determined from figure 3.

stiffness of $Q_i/Q_{\rm gB}$ with respect to κ_T has been observed in numerical simulations of simplified ITG-unstable plasmas in the presence of flow shear [36, 9]. It is also in agreement with experimental [37, 38] and numerical [39] findings in the outer core of the JET experiment, which also showed that ion heat transport's stiffness is not affected by an increase in γ_E, whereas the critical ITG threshold does increase with γ_E.

3.2 Subcritical turbulence

We have found that in all our simulations with $\gamma_E > 0$, small amplitude initial perturbations decayed (i.e. the system was linearly stable) and a finite initial perturbation was always required in order to ignite turbulence and reach a saturated turbulent state. Turbulence in MAST in the equilibrium configuration that we study here belongs to the class of subcritical systems [40, 12, 41, 13], where linear modes are formally stable, but may be transiently amplified by a given factor over a given time. If the transient amplification is sufficient for nonlinear interactions to become significant before the modes decay, then a turbulent state may emerge. This turbulent state persists provided the fluctuation amplitudes do not fall below some critical value (for example, by way of the chaotic evolution, with occasional large deviations from an average fluctuation level that characterises the turbulent state) below which they cannot be transiently amplified once again back to nonlinearly sustained saturated level.

In this work, we have assumed that other activity in the experiment (e.g. large-scale MHD modes or more virulent turbulence on neighbouring flux surfaces) can generate arbitrarily large perturbations as an initial condition to our system. For this reason, we have used

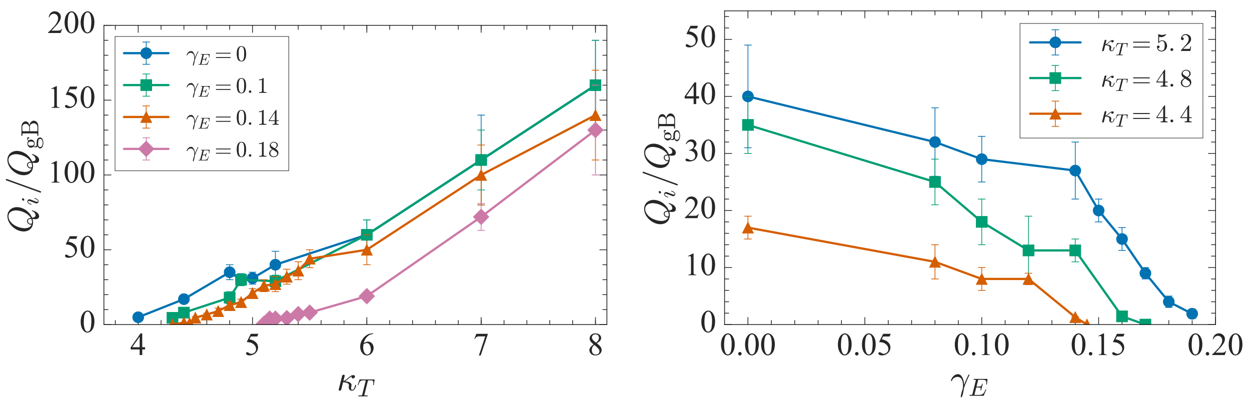

(a) (b)

Figure 6: (a) Ion heat flux $Q_i/Q_{\rm gB}$ as a function of κ_T for several values of γ_E. (b) $Q_i/Q_{\rm gB}$ as a function of γ_E for several values of κ_T.

Table 2: Parameter values for simulations that match the experimental heat flux, $Q_i^{\rm exp}/Q_{\rm gB} = 2\pm1$.

κ_T	γ_E	$Q_i/Q_{\rm gB}$
4.4	0.14	1.3 ± 0.1
4.45	0.14	1.0 ± 0.1
4.8	0.16	1.44 ± 0.05
4.85	0.16	1.2 ± 0.1
5.15	0.18	4 ± 1
5.2	0.18	4 ± 1

the largest initial perturbation allowed by the numerical algorithm used in GS2, i.e., as large as possible without forcing the system to evolve the distribution function with time steps so small that the simulations would require prohibitively long simulation times. All nonlinear simulations presented in section 3.1 were run with such large initial conditions. For the regions where we have reported $Q_i = 0$, we could not ignite turbulence using even the largest initial condition tolerated by the GS2 algorithm. In this section we will demonstrate the subcritical nature of the turbulence by investigating the effect of changing the amplitude of the initial perturbation in both linear and nonlinear simulations.

3.2.1 Minimum initial perturbation amplitude

We start by considering the nonlinear time evolution of a simulation at the nominal equilibrium parameters $(\kappa_T, \gamma_E) = (5.1, 0.16)$. Figure 7(a) shows $Q_i/Q_{\rm gB}$ as a function of time for nonlinear simulations with increasing initial amplitude. These parameter values represent a simulation somewhat away from the turbulence threshold [see figure 5(a)] and yet, for a range of initial amplitudes, we see that the system decays rapidly. This is a clear indication that the turbulence is subcritical. We see that there is a certain minimum initial perturbation amplitude starting from which it is possible for the system to reach a saturated state, rather than decay. Importantly, for simulations that do reach a saturated state, the level of

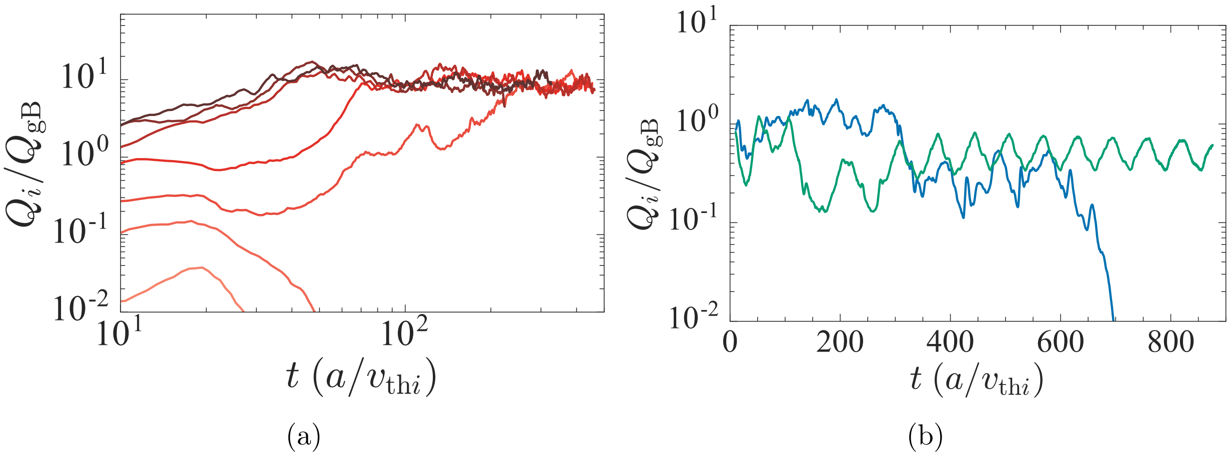

Figure 7: (a) Ion heat flux Q_i/Q_{gB} as a function of time for different initial-perturbation amplitudes for $(\kappa_T, \gamma_E) = (5.1, 0.16)$, keeping all other parameters the same. (b) Q_i/Q_{gB} as a function of time for two identical simulations at $(\kappa_T, \gamma_E) = (5.1, 0.18)$. The difference between the time series shown as the blue and green lines is the realisation of the random noise with which GS2 initialised these simulation. Beyond $t = 300$ $(a/v_{\mathrm{th}i})$, the simulations seem to converge to a similar average value before one is abruptly quenched due to the amplitudes falling below the critical values required to sustain a saturated state.

saturation does not depend on the amplitude of the initial perturbation.

3.2.2 Finite life time of turbulence

A large initial perturbation is not sufficient to guarantee that a subcritical system continues in a statistically steady state indefinitely. In simulations with equilibrium parameters close to the turbulence threshold, we found that turbulence could be quenched at a seemingly unpredictable time. For example, figure 7(b) shows the time trace of Q_i/Q_{gB} for two identical simulations at the parameter values $(\kappa_T, \gamma_E) = (5.1, 0.18)$, close to the turbulence threshold. These simulations were initialised with random noise of a given amplitude in each Fourier mode and the only difference between the two simulations is the realisation of this random noise. We see the simulations saturate at a similar level beyond $t = 300$ $(a/v_{\mathrm{th}i})$, but then one of them abruptly decays. This is another indication that the system is subcritical: the decaying simulation has fallen below the critical amplitude needed to sustain turbulence. Practically, in this study, we decided that a simulation reached a saturated state if the heat flux evolved at a roughly constant value for at least 200 $(a/v_{\mathrm{th}i})$.

The finite life time of turbulence in subcritical systems is well established in some hydrodynamic systems, such as fluid flow in a pipe [42]. By running a large number of identical pipe-flow experiments [43, 44, 45] and numerical simulations [42, 44, 46, 45], it was shown that the "life time" of subcritical turbulence (the characteristic time that elapses before turbulence decays to laminar flow) is a function of the Reynolds number. The Reynolds number in pipe flows quantifies the "distance from the turbulence threshold". In particular, it was shown that the larger its value (i.e., the further the system is from the turbulence threshold), the longer the turbulence is likely to persist. More recently, the same phenomenon of finite turbulence lifetime was observed in MHD simulations of astrophysical Keplerian shear flow systems [47], where the distance from threshold was characterised by the magnetic Reynolds number and the turbulence persists longer for large values of this parameter.

Given the above considerations, we would also expect the subcritical turbulence considered here to persist for longer times at larger values of Q_i/Q_{gB}. The pipe-flow and astrophysical studies referred to above relied on running many experiments and simulations in order to build up sufficient statistics to determine the dependence of the turbulence lifetimes on the system parameters. With the high resolutions demanded by nonlinear gyrokinetic simulations of plasmas in the core of tokamaks we are neither able to run a sufficient number of simulations nor to run them for a sufficient amount of time to determine the turbulence lifetimes for our system. However, this may be possible in future, given advances in computing and numerics or through the use of reduced models.

3.2.3 Transient growth of perturbations

A system can reach a saturated turbulent state despite being stable to infinitesimal perturbations due to transient growth of (large enough) finite perturbations. This transient growth can sustain turbulence provided perturbations reach an amplitude sufficient for nonlinear interaction. Having established the subcritical nature of the system, the question we would now like to address is how much transient growth is sufficient for the system to reach a turbulent state. We have already seen which values of κ_T and γ_E lead to a turbulent state [see figure 5(a)] and we now investigate transient growth of perturbations via linear GS2 simulations at these values of κ_T and γ_E.

We performed an extensive series of linear simulations and calculated the time evolution of the electrostatic potential φ as a function of $k_y\rho_i$, κ_T, and γ_E. Figure 8(a) shows an example of the time evolution of φ (at $k_y\rho_i = 0.2$ and $\gamma_E = 0.16$) for a range of κ_T, normalised to the value of φ at the time (called $t = 0$) when the flow shear is switched on, that is, $\varphi_N^2(t) = \varphi^2(t)/\varphi^2(0)$. We have averaged φ over k_x. Figure 8(a) illustrates the phenomenon of transient growth in a subcritical system and we see that, as κ_T is increased, the system exhibits stronger transient growth. At $\gamma_E = 0.16$, we saw in figure 5(a) that turbulence could be sustained at $\kappa_T \gtrsim 4.8$. Indeed, figure 8(a) shows that there is only a marginal amount of transient growth at $\kappa_T \approx 4.8$.

3.2.4 Characterising transient growth

For linear simulations exhibiting transient growth, one cannot define a "linear growth rate", as one does for linear simulations with $\gamma_E = 0$ where $\varphi(t)$ grows exponentially. However, methods for determining an "effective" linear growth rate have been outlined in Ref. [2] and [12]. Here, we follow Ref. [12] and use the "transient-amplification factor" as a measure of the vigour of the transient growth. For a total amplification factor e^{N_γ}, the amplification exponent N_γ is defined by

$$N_\gamma = \frac{1}{2}\ln\frac{\varphi^2(t_0)}{\varphi^2(0)} = \int_0^{t_0} \mathrm{d}t\gamma(t), \tag{12}$$

where t_0 is the time taken to reach the maximum amplification, and $\gamma(t)$ is the time-dependent growth rate. These quantities are illustrated in Figure 8(b), which shows a typical

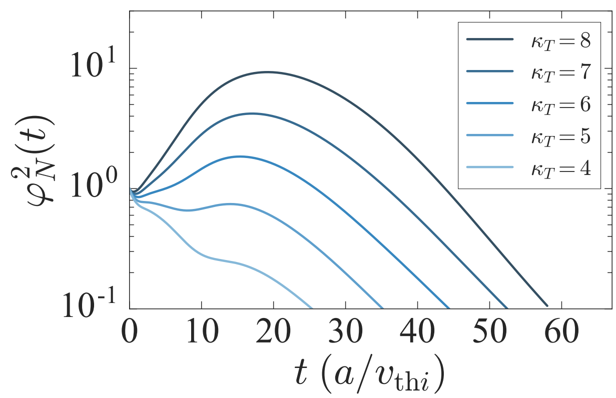

(a)

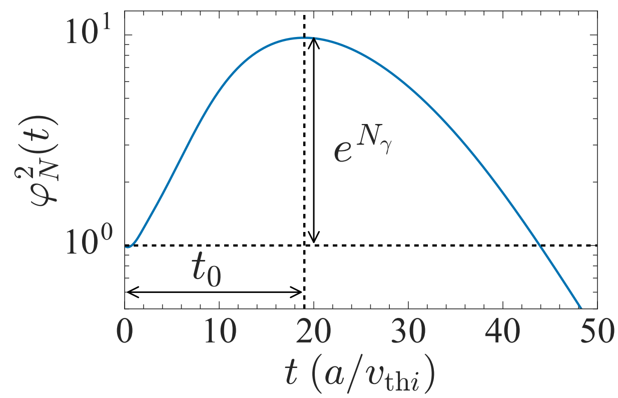

(b)

Figure 8: (a) Transient growth of initial perturbations of the electrostatic potential $\varphi_N^2(t)$ (normalised to the time at which flow shear is switched on) at $\gamma_E = 0.16$, for a range of κ_T values. These time evolutions were obtained from purely linear simulations for $k_y\rho_i = 0.2$, approximately the wavenumber that gives the largest transient growth [see figure 9(a)], and summed over k_x. As κ_T is increased, the strength of the transient growth also increases. (b) $\varphi_N^2(t)$ as a function of time for a strongly growing mode at $(\kappa_T, \gamma_E, k_y\rho_i) = (8, 0.16, 0.2)$ further illustrating transient amplification. The total amplification factor is e^{N_γ} and the time taken to reach maximal amplification is t_0.

linear simulation with strong amplification, with e^{N_γ} and t_0 indicated.

It was argued in Ref. [12] that the parameters N_γ and t_0 determine whether turbulence can be sustained, in the following way. Perturbations grow only transiently because flow shear leads to $k_x(t) = k_x(0) - \gamma_E k_y t$ being swept from the region where perturbations are unstable to larger values, where they are stabilised by dissipation. If nonlinear interactions scatter energy back into the unstable modes before perturbations decay they can be transiently amplified once again, and so on. In this way, a nonlinear saturated state can be sustained. The typical timescale for nonlinear interactions is the nonlinear decorrelation time $\tau_{\mathrm{NL}} \sim 1/k_\perp V_E$, where $k_\perp$ is the typical perpendicular wave number, and V_E is given by (7). To sustain turbulence, transient growth should last at least as long as one nonlinear decorrelation time:

$$t_0 \gtrsim \tau_{\mathrm{NL}}. \tag{13}$$

At the same time, the rate of amplification should be at least comparable to the nonlinear decorrelation rate:

$$\frac{N_\gamma}{t_0} \gtrsim \frac{1}{\tau_{\mathrm{NL}}}. \tag{14}$$

Combining (13) and (14), we see that a sustained turbulent state requires

$$N_\gamma \gtrsim 1. \tag{15}$$

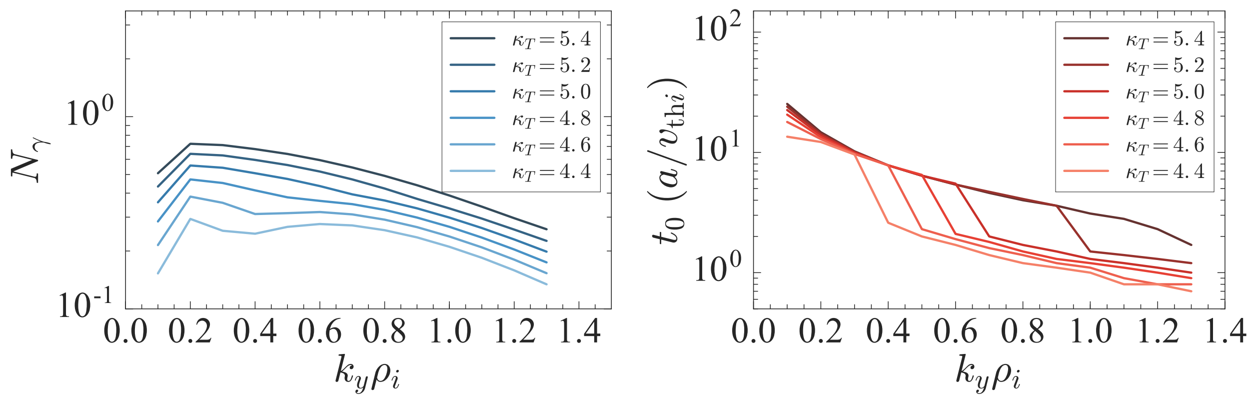

(a) (b)

Figure 9: (a) The transient-amplification factor N_γ, defined in (12), for a range of values of κ_T at $\gamma_E = 0.16$. N_γ increases smoothly with increasing κ_T as the nonlinear threshold is passed. (b) Time t_0 taken to reach maximum amplification for a range of values of κ_T, also at $\gamma_E = 0.16$. Increasing κ_T leads to transient amplification lasting for a longer time.

3.2.5 Conditions for the onset of subcritical turbulence

We now want to estimate the critical values of N_γ and t_0 above which turbulence is triggered and a saturated state can be established in our system. Figure 9 shows N_γ and t_0 as functions of $k_y\rho_i$ for a range of different κ_T values at $\gamma_E = 0.16$ (only wave numbers up to $k_y\rho_i = 1.3$ are shown, because numerical dissipation effectively suppresses transient growth beyond this value). As a point of reference, for $\gamma_E = 0.16$, the transition to turbulence occurs at $\kappa_T \approx 4.8$ [see figure 5(b)]. For the linear simulations in figure 9, we see a relatively smooth increase in N_γ and t_0 as κ_T is increased across this nonlinear threshold, with larger transient amplification and modes with smaller $k_y\rho_i$ experiencing amplification over a longer time period.

To investigate the conditions for the onset of turbulence, we consider N_γ and t_0 for the marginally unstable simulations identified in section 3.1. Figures 10(a) and (b) show N_γ and t_0 as functions of $k_y\rho_i$ for $(\kappa_T, \gamma_E) = (4.4, 0.14), (4.8, 0.16), (5.1, 0.18)$. We see that both N_γ and t_0 are roughly the same for our marginally unstable simulations, suggesting that the values shown in Figures 10(a) and (b) are indeed the critical values necessary for the onset of turbulence.

We see from figures 9(a) and 10(a) that the maximum N_γ is at $k_y\rho_i \approx 0.2$ and we consider its value here to to determine the critical condition. Figure 11 shows the maximum value $N_{\gamma,\max}$ of the transient-amplification factor as a function of κ_T. The marked simulations are for the critical values of κ_T above which turbulence can be sustained, given a sufficiently large initial perturbation amplitude. Figure 11 shows that $N_{\gamma,\max}$ scales linearly with κ_T for each γ_E, with higher values of γ_E resulting in lower values of $N_{\gamma,\max}$. The other important feature is that the values of $N_{\gamma,\max}$ at the critical values of κ_T are similar, giving an approximate critical condition: $N_{\gamma,\max} \sim 0.4$. This value of $N_{\gamma,\max}$ is comparable to that found in previous work [12, 41].

Returning to figure 10(b), and assuming that low-k_y modes are the important ones for sustaining turbulence, it is reasonable to estimate that the onset of turbulence requires

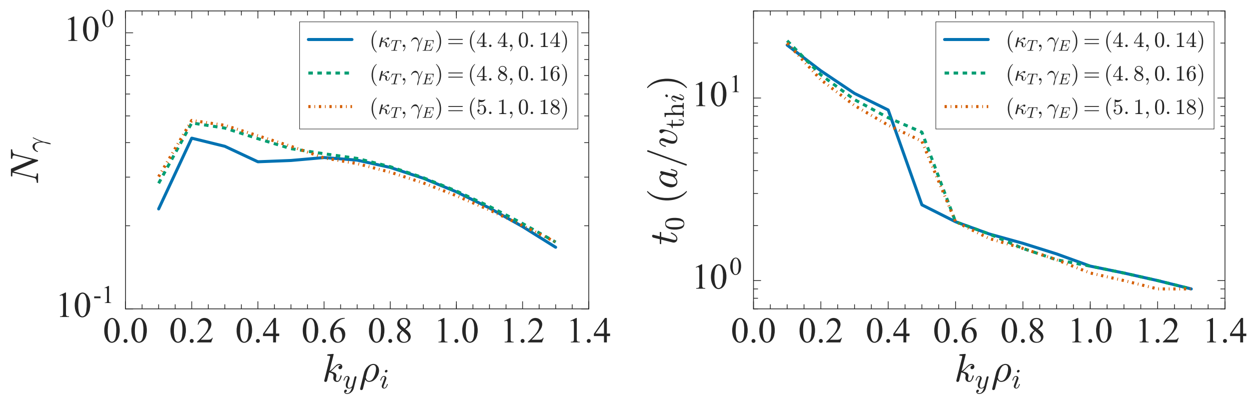

(a) (b)

Figure 10: (a) Transient-amplification factor N_γ [see equation (12)] and (b) transient-amplification time t_0 for the three marginal simulations identified in section 3.1. The values of N_γ and t_0 that correspond to the marginally unstable equilibria are approximately the same, suggesting that these represent the critical values required for the system to reach a saturated turbulent state.

$t_0 \gtrsim 10\ (a/v_{\mathrm{th}i})$. We will return to the comparison of t_0 with τ_{NL} after estimating τ_{NL} in section 4.4.4, where we confirm that $t_0 \gtrsim \tau_{\mathrm{NL}}$ and, therefore, that a sustained turbulent state requires an amplification time comparable to (or greater than) the nonlinear decorrelation time.

We have shown that the changes in N_γ and t_0 are relatively smooth as the turbulence threshold is surpassed (determined from our simulations in section 3.1), suggesting nonlinear simulations are essential in predicting the *exact* transition to turbulence. In the next section, we will investigate the nature of this transition by considering the real-space structure of the turbulence in our nonlinear simulations.

3.3 Structure of turbulence close to and far from the threshold

Having established the subcritical nature of the system, we now investigate the consequences for the structure of turbulence. We will argue that our subcritical system supports the formation of long-lived coherent structures close to the turbulence threshold, that the heat flux is proportional to the product of number of these structures and their maximum amplitude, and that the properties of the turbulence are characterised by the "distance from threshold" (as opposed to the specific values of the stability parameters κ_T and γ_E), as measured, for example, by the turbulent ion heat flux. We previously reported some of these results in Ref. [14], based on the simulations in this study, and provide a more comprehensive description here.

3.3.1 Coherent structures in the near-marginal state

Figure 12 shows the density-fluctuation field $\delta n_i/n_i$ at the outboard midplane of MAST as a function of the local GS2 coordinates x and y. The simulations shown in figures 12(a)–12(c) are marked by points in figure 5(a) and, importantly, all three are well within the region of experimental uncertainty. We have chosen four combinations of the stability parameters

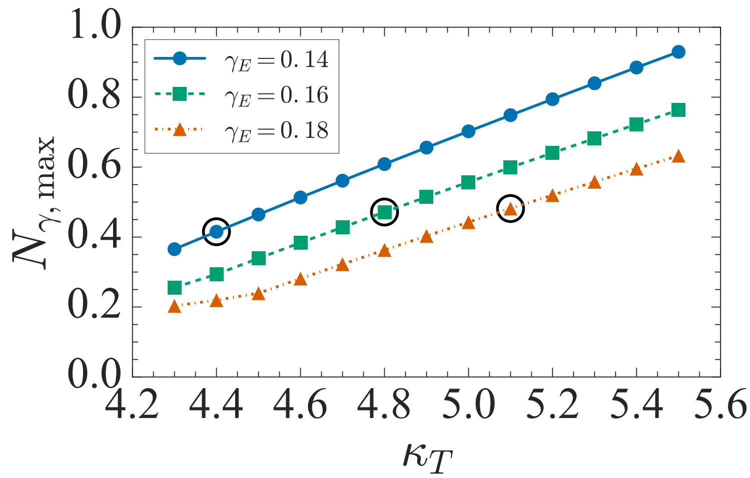

Figure 11: Maximum transient-amplification factor $N_{\gamma,\max}$ versus κ_T for three values of γ_E within the range of experimental uncertainty. The simulations circled in black represent the critical values of κ_T above which turbulence can be sustained, suggesting the onset of turbulence occurs at $N_{\gamma,\max} \simeq 0.4$.

(κ_T, γ_E) as the system is taken away from the turbulence threshold: $(4.8, 0.16)$, which is close to the turbulence threshold [figure 12(a)], $(4.9, 0.16)$, an intermediate case between the marginal and strongly driven turbulence [figure 12(b)], $(5.2, 0.16)$, a strongly driven case further from the threshold [figure 12(c)], and $(5.2, 0)$, a case without flow shear [figure 12(d)], representative of the normal, supercritical ITG turbulence that has been thoroughly studied in the past [48, 49, 50]. For the same four cases, figures 13 and 14 show the perturbed radial $\boldsymbol{E}\times\boldsymbol{B}$ velocity V_{Er} and the perpendicular temperature-fluctuation $\delta T_{\perp i}/T_{\perp i} \equiv a/\rho_i \delta T_{\perp i}/T_{\perp i}$ fields. We have calculated V_{Er} velocity by taking the radial component of (7), given by (see equation (3.42) in Ref [34])

$$V_{Er} = \frac{c}{aB_{\mathrm{ref}}} \frac{1}{|\nabla\psi|} \left|\frac{\partial\psi}{\partial r}\right|_{r_0} \frac{\partial\varphi}{\partial y}, \tag{16}$$

recalling that a is the half diameter of the LCFS, B_{ref} is the toroidal magnetic field at the magnetic axis, ψ is the poloidal magnetic flux, and $r = D/2a$.

As the system is taken away from the threshold, the nature of the fluctuation field changes as follows. The near-threshold state [figure 12(a)] is dominated by coherent, long-lived (see figure 16) structures that are at high intensity compared to the background fluctuations. As κ_T is slightly increased (in this case by only 0.1), these structures become more numerous [figure 12(b)], but have roughly the same maximum amplitude: $(\delta n_i/n_i)_{\max} \sim 0.08$. In contrast, the strongly driven state [far from threshold; figure 12(c)] exhibits a more conventional turbulence, characterised by many interacting eddies with larger amplitudes.

These simulations are typical of the cases close to and far from the turbulence threshold, i.e., in simulations near the threshold, we always find sparse but well-defined coherent structures that survive against a backdrop of weaker fluctuations [with the important exception of the case of $\gamma_E = 0$ shown in figure 12(d)]. Likewise, for all cases where the system is taken away from the threshold by increasing κ_T, or decreasing γ_E, the transition from co-

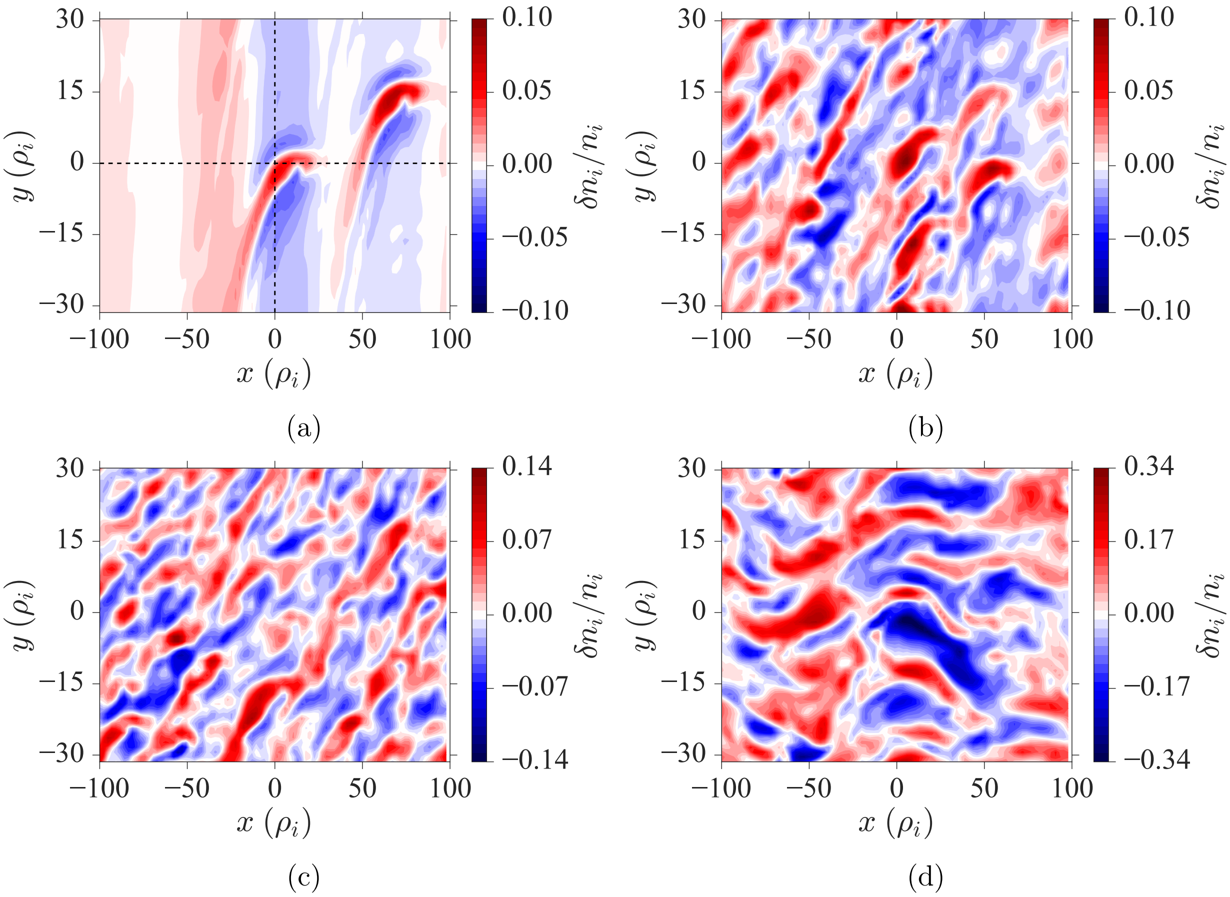

Figure 12: Density-fluctuation field $\delta n_i/n_i$ at the outboard midplane of MAST as a function of the local GS2 coordinates x and y, for four combinations of stability parameters. (a) Near-threshold turbulence, $(\kappa_T, \gamma_E) = (4.8, 0.16)$. The dashed lines indicate the planes of constant x and y used to demonstrate the parallel structure in figure 15. (b) Turbulence intermediate between the near-threshold and strongly driven cases, $(\kappa_T, \gamma_E) = (4.9, 0.16)$. (c) Strongly driven turbulence, $(\kappa_T, \gamma_E) = (5.2, 0.16)$. (d) Turbulence without flow shear, $(\kappa_T, \gamma_E) = (5.2, 0)$, showing strong zonal flows.

herent structures to strongly driven interacting eddies occurs the same way: the structures become more numerous, while maintaining roughly the same amplitude, until they fill the entire domain, interact with each other, and break up. For parameter values far from the threshold, we observe no discernible coherent structures, but rather strongly time-dependent fluctuations with amplitudes that increase with κ_T.

We complete our description of these coherent structures by examining their parallel extent and their motion. Figure 15 shows two views of the coherent structures from figure 12(a) in the parallel direction (which in GS2 is quantified by the poloidal angle θ): at constant y [figure 15(a)] and at constant x [figure 15(b)]. It is clear that the coherent structures are elongated in the parallel direction and have an amplitude much larger than the background fluctuations.

The motion of the coherent structures results from a combination of the background plasma flow, and a radial drift of the structures themselves. Importantly, they are long-lived

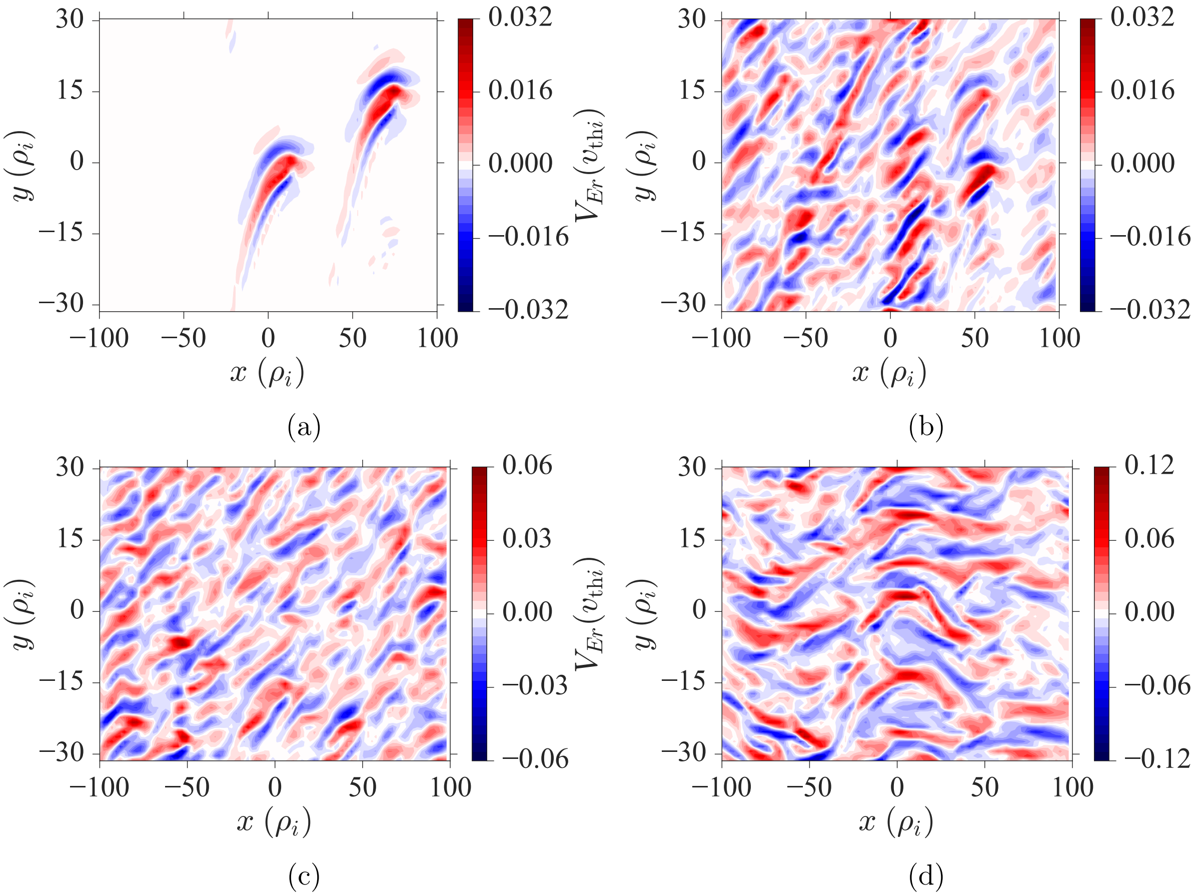

Figure 13: Radial $\boldsymbol{E}\times\boldsymbol{B}$ velocity V_{Er} at the outboard midplane of MAST as a function of the local GS2 coordinates x and y for the same equilibrium parameters as in figure 12.

as we will now show by looking at their motion in time. Figures 16(a) and 16(b) show $\delta n_i/n_i$ for a marginal nonlinear simulation at $(\kappa_T, \gamma_E) = (5.1, 0.18)$, which has only one coherent structure, as a function of (t, x) and (t, y) (taking the maximum value of $\delta n_i/n_i$ in the other direction), respectively. Figure 16(a) shows the radial motion of the structure across the domain, which the structure crosses in a time of roughly 50 $(a/v_{\mathrm{th}i})$, and illustrates the long-lived nature of coherent structures close to the turbulence threshold (recalling that the GS2 domain is periodic in x and y). We see that the structure exists for $t > 100$ $(a/v_{\mathrm{th}i})$. The radial motion of the structure in figure 16(a) has a constant velocity: fitting its trajectory with a straight line (the dashed line) gives $v_x = 3.150 \pm 0.009\ \rho_* v_{\mathrm{th}i}$ (where $\rho_* = \rho_i/a = 1/100$, given that $\rho_i = 6.08\times10^{-3}$ m and $a = 0.58$ m). Figure 16(b) shows the poloidal advection of the structure with a much shorter poloidal crossing time of roughly 5 $(a/v_{\mathrm{th}i})$. The poloidal motion of the structure is due to the combination of poloidal advection by the mean flow (remembering that, since we have moved to the rotating frame, the flow is zero at $x = 0$) and the radial drift of the structures. As we saw in figure 16(a), v_x is constant and the radial position is given by $x(t) = v_x t$. The poloidal advection due to the flow shear is given by $v_y(t) = \gamma_E x(t)$ and so the direction of the flow shear reverses at $x = 0$. Combining the expressions for $x(t)$ and $v_y(t)$ and integrating, we find that $y(t) \propto \gamma_E v_x t^2$, and, as shown by

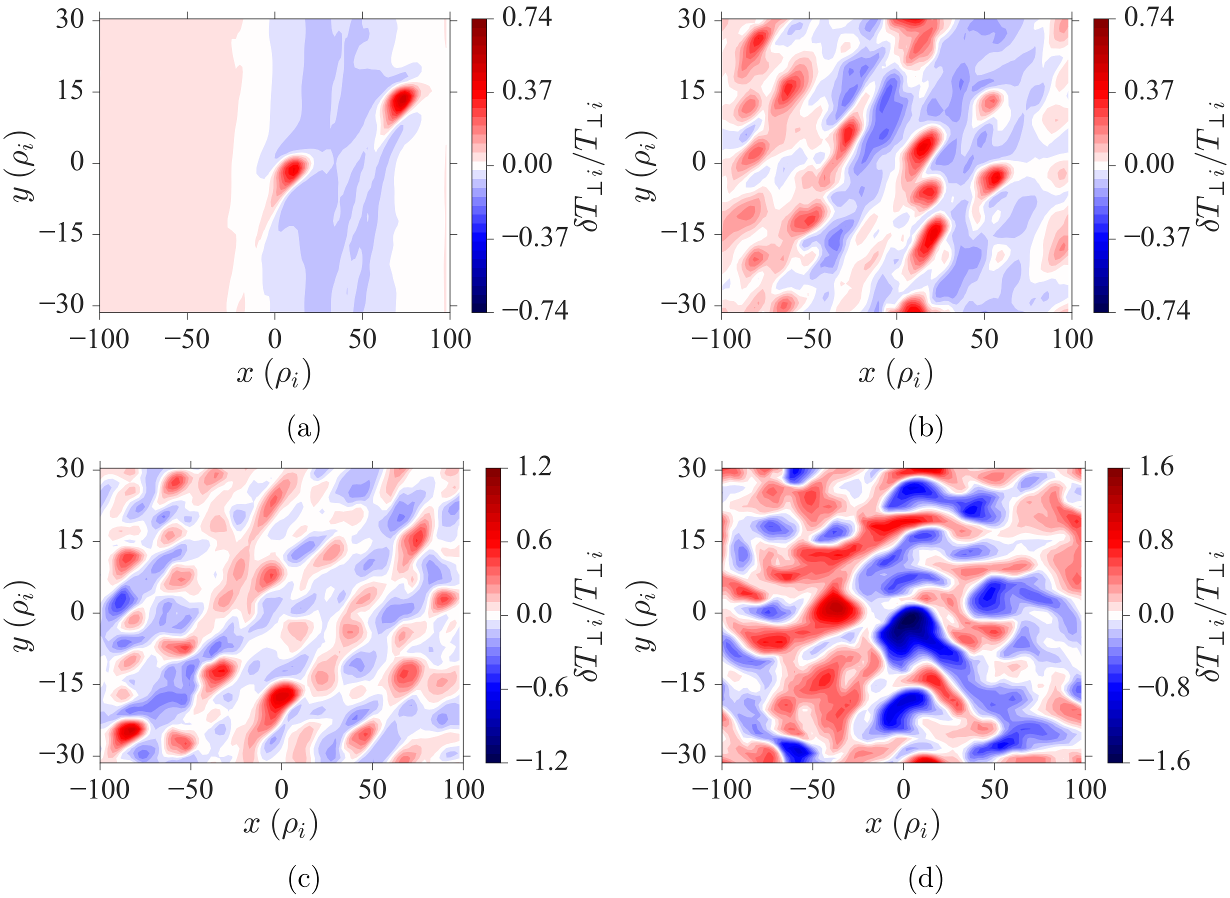

Figure 14: Perpendicular-temperature fluctuation field $\delta T_{\perp i}/T_{\perp i}$ at the outboard midplane of MAST as a function of the local GS2 coordinates x and y for the same equilibrium parameters as in figure 12.

the dashed line in figure 16(b), this describes the poloidal motion of the structures, which indeed reverses direction at $x = 0$.

The coherent structures in the marginal case, such as the one described above, are unlike the strongly interacting eddies in the cases far from the turbulence threshold and are more likely to constitute a nonlinear travelling wave (soliton-like) solution to the gyrokinetic equation. However, more work is needed to develop an analytic description of these structures.

3.3.2 Q_i/Q_{gB} as an order parameter

The results in section 3.3.1 suggest that the nature of the turbulence is determined by how far the system is from the turbulence threshold. This means perhaps that the important metric that should be used to quantify the state of the system is the "distance from threshold" and not the specific values of κ_T and γ_E (although both can be used to control the distance from threshold). The ion heat flux Q_i/Q_{gB} is a strong function of κ_T and γ_E, increasing monotonically as the system is taken away from the threshold [see figure 5(a)], so we can use Q_i/Q_{gB} as a control parameter to measure the distance from the threshold. In sections 3.3.3 and 3.3.4, we will quantify the change in the nature of the turbulence, namely, the change

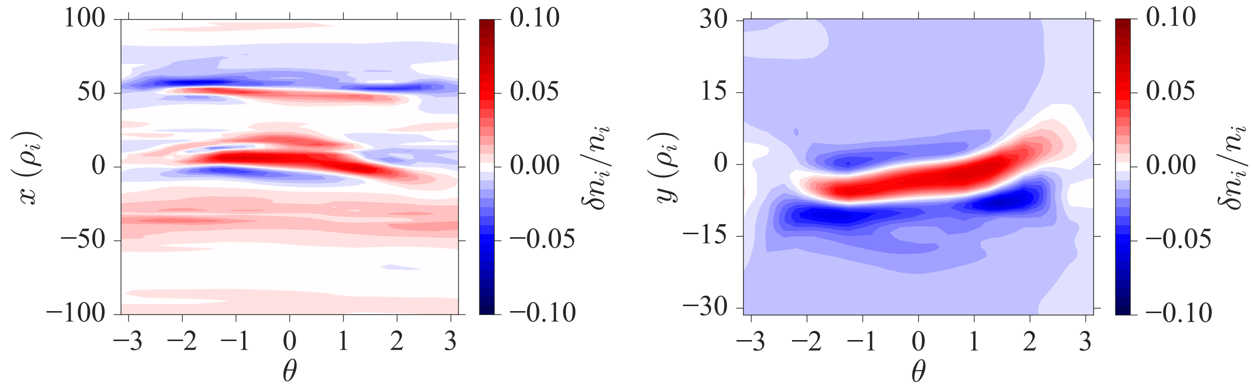

(a) (b)

Figure 15: (a) Density-fluctuation field $\delta n_i/n_i$ in the x-z plane at $y = 0$. (b) Density-fluctuation field $\delta n_i/n_i$ in the y-z plane at $x = 0$. Both plots are for the same simulation and at the same time as in figure 12(a), where the corresponding planes are indicated by the dashed lines. The parallel direction in GS2 is quantified by the poloidal angle θ.

in the amplitude and number of coherent structures, for our parameter scan and show that the distance from threshold is indeed the relevant order parameter.

3.3.3 Maximum amplitude

Here, we investigate how the amplitude of the density fluctuations change with the distance from threshold. For near-threshold cases, such as the one shown in figure 12(a), the dominant features are the coherent structures, which have high densities compared to the background fluctuations. In order to capture the amplitude of these structures, we measure the maximum amplitude of the density field, as opposed to an (x, y)-averaged one, which would be small because of the relatively small volume taken up by the coherent structures. Figure 17 shows the maximum amplitude $(\delta n_i/n_i)_{\text{max}}$, maximised over the (x, y)-plane and averaged over time, versus Q_i/Q_{gB} for the entire set of simulations in our parameter scan.

The striking feature of figure 17 is that $(\delta n_i/n_i)_{\text{max}}$ hits a finite "floor" as Q_i/Q_{gB} approaches and goes below its experimental value. This coincides with the appearance of the long-lived structures such as those shown in figure 12(a). This floor is absent in simulations with $\gamma_E = 0$, suggesting that the turbulence with $\gamma_E = 0$ is fundamentally different close to the turbulence threshold (as indeed also suggested by the absence of coherent structures).

Far from the turbulence threshold, we can construct from (11) a naive estimate of the relationship between Q_i/Q_{gB} and $\delta n_i/n_i$:

$$\frac{Q_i}{Q_{\text{gB}}} \sim \frac{a^2}{\rho_i^2}\frac{\delta T_i}{T_i}\frac{V_{Er}}{v_{\text{th}i}} \sim k_y\rho_i\left(\frac{\delta n_i}{n_i}\right)^2, \tag{17}$$

assuming that fluctuations of φ are related (by order of magnitude) to the electron (and, therefore, ion) density via the Boltzmann response $e\varphi/T_e \sim \delta n_e/n_e$ and that ion temperature and density fluctuations are approximately proportional to each other (cf. figures 12 and 14). The scaling $\delta n_i/n_i \propto Q_i^{1/2}$ that follows from (17) assuming that $k_y\rho_i$ is not a strong function

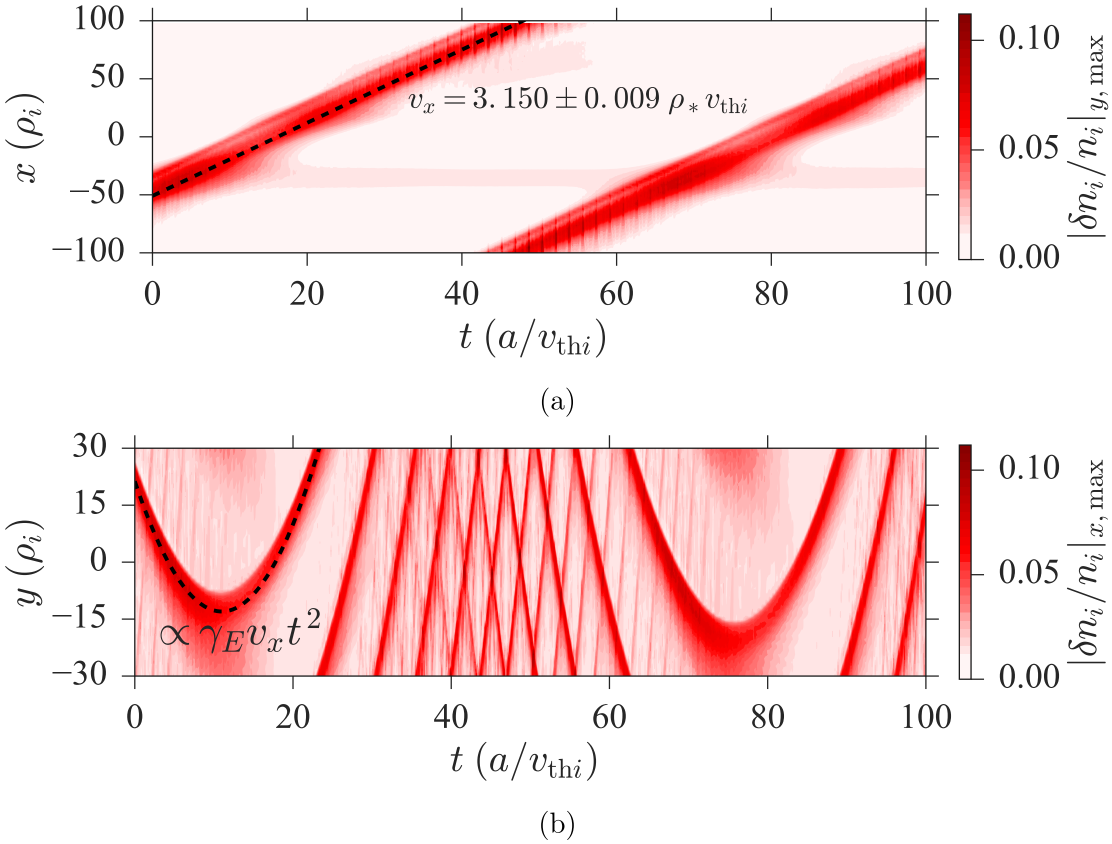

Figure 16: Density-fluctuation field $\delta n_i/n_i$ as a function of (a) x and t (taking the maximum in the y direction) and (b) y and t (taking the maximum in the x direction) for a marginally unstable case with $(\kappa_T, \gamma_E) = (5.1, 0.18)$, which contains only one coherent structure. The structure is advected both radially and poloidally. The GS2 domain is periodic in x and y and so this is the same structure throughout the entire time period shown. The dashed line in (a) indicates $x = v_x t$, and in (b) it indicates $y \propto \gamma_E v_x t$, showing that the poloidal advection is due to the flow associated with the shear γ_E.

of Q_i is indicated by the red line in figure 17, and describes well the scaling away from the threshold. We also see that $\gamma_E = 0$ and $\gamma_E > 0$ simulations are similar away from the threshold.

The above results can be understood as follows. In the case of supercritical turbulence, one typically observes smaller fluctuation amplitudes all the way to the turbulence threshold – there is no minimum amplitude required to sustain turbulence. In contrast, figure 17 shows that, for the subcritical turbulence that we are investigating, the maximum fluctuation amplitude stays constant as we approach the threshold. This is because there is a critical value required in order to sustain a saturated nonlinear state – indeex, if the amplitude dropped below a certain value in a subcritical system, all perturbations would decay. However, even as the fluctuation amplitude stays constant, the heat flux decreases as the threshold is approached. The system can satisfy the requirement of finite amplitude while simultaneously allowing the heat flux to decrease through a reduction of the volume taken up by finite amplitude turbulence. As we demonstrate in the next section, this is achieved via a reduction

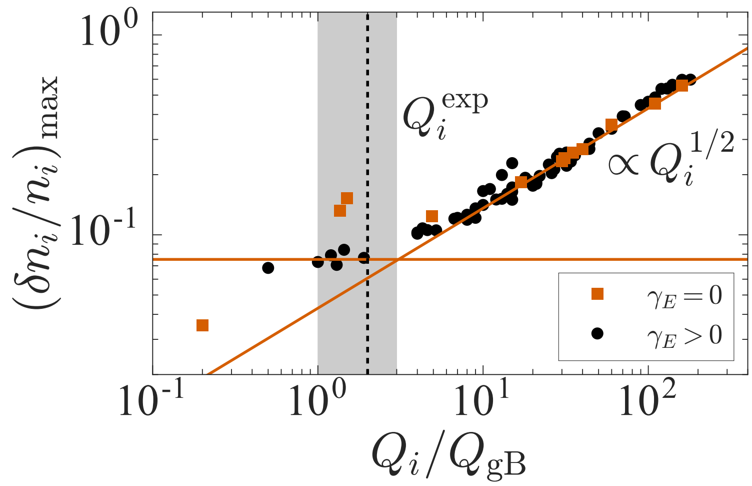

Figure 17: Maximum amplitude of the density fluctuations versus Q_i/Q_{gB}. The naive scaling (17), $\delta n_i/n_i \propto Q_i^{1/2}$, is shown for reference and holds far from threshold, whereas for small values of Q_i/Q_{gB} (around and below the experimental value $Q_i^{\exp}$), the amplitude becomes independent of Q_i/Q_{gB}.

in the number of coherent structures.

3.3.4 Structure counting

We quantify the changes in volume taken up by the finite-amplitude structures by measuring the typical number of these structures in our simulations as a function of the distance from threshold. We follow the "structure-counting" methods first described in [14], which involve the following steps, illustrated in figure 18.

As a pre-processing step we apply a Gaussian image filter with a standard deviation of the order of the grid scale. We then set all density-field values below a certain percentile (here 75% of the maximum amplitude) to 0 and above it to 1. The level of this threshold function is somewhat arbitrary and the exact number of structures will depend on this level, but not the trend as a function of our equilibrium parameters. After applying the threshold function, we are left with an array of 1s representing our structures against a background of 0s. We then remove structures below 10% of the mean structure size as a post-processing step to avoid the counting of spurious small isolated blobs of high density. To count the structures, we employ a general-purpose image processing package *scikit-image* [51], which implements an efficient labelling algorithm [52], then used by us to label connected regions. In figure 18, the image-labelling algorithm found 19 structures.

Figure 19(a) shows the results of the above analysis applied to our entire set of simulations: the number of structures N with amplitudes above the 75^{th} percentile versus the ion heat flux Q_i/Q_{gB}. As in figure 17, there are two distinct regimes: N grows with Q_i/Q_{gB} until the structures have filled the simulation domain (which happens just above the experimental value of the flux), whereupon N tends to a constant.

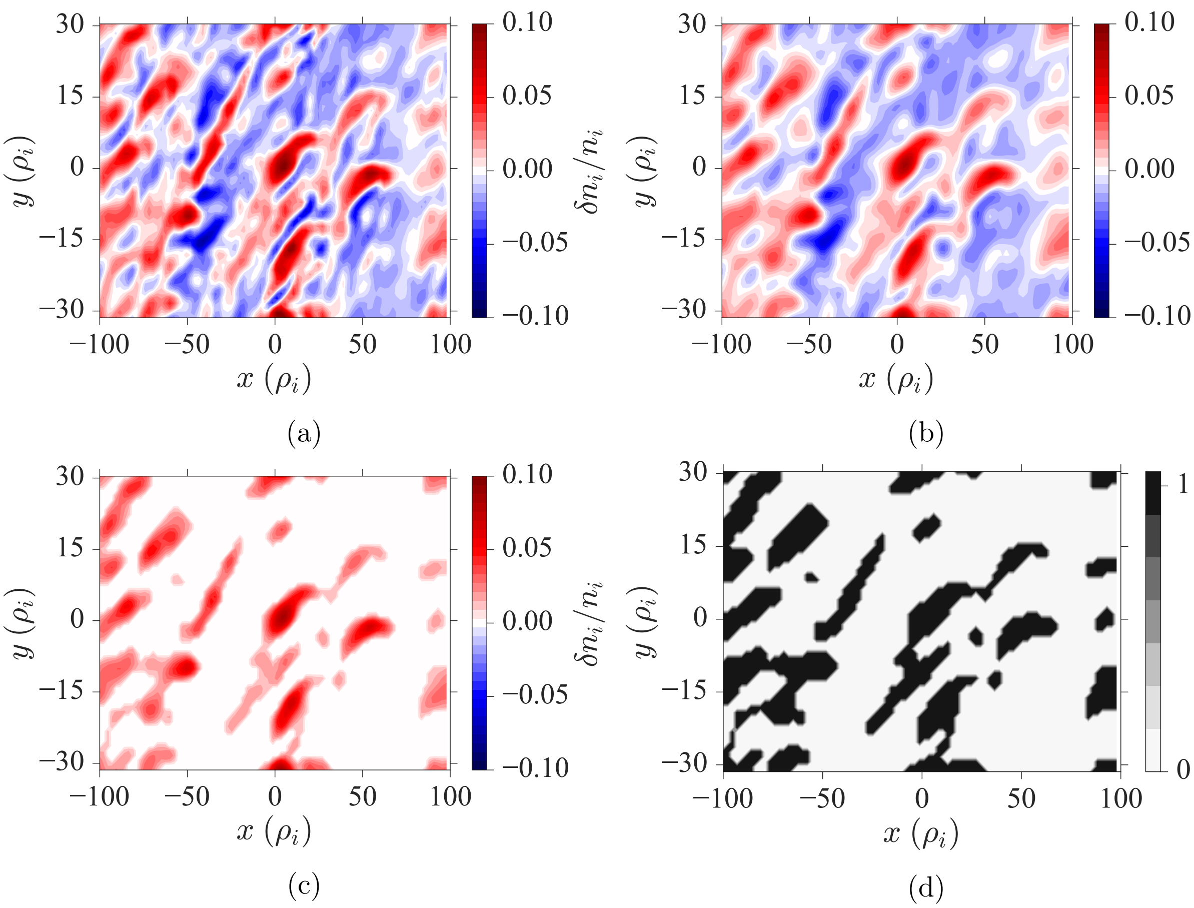

Figure 18: Stages of the structure-counting procedure: (a) the original density-fluctuation field [as in figure 12(b)]; (b) the same fieldafter the application of a Gaussian filter to smooth the structures; (c) after the application of a 75% threshold function; (d) after setting $\delta n_i/n_i > 0$ values to 1 for simplicity. The image-labelling algorithm is then applied to (d) and returns 19 structures for this case.

Taking figures 17 and 19(a) in combination, we have, roughly,

$$\frac{Q_i}{Q_{\mathrm{gB}}} \sim N\left(\frac{\delta n_i}{n_i}\right)^2_{\max}, \tag{18}$$

i.e., near the threshold, the turbulent heat flux increases because coherent structures become more numerous (but not more intense), whereas away from the threshold, it does so because the fluctuation amplitude increases (at a roughly constant number of structures). This relationship is confirmed by figure 19(b), where the scaling (18) is checked directly.

3.3.5 Shear due to zonal flows

In the conventional picture of the saturation mechanism of ITG-driven turbulence, zonal modes play a key role [53, 54, 35, 50, 55]. Zonal modes are fluctuations in the system with $k_y = k_\parallel = 0$ and $k_x > 0$, i.e., they have finite radial extent, but are poloidally symmetric.

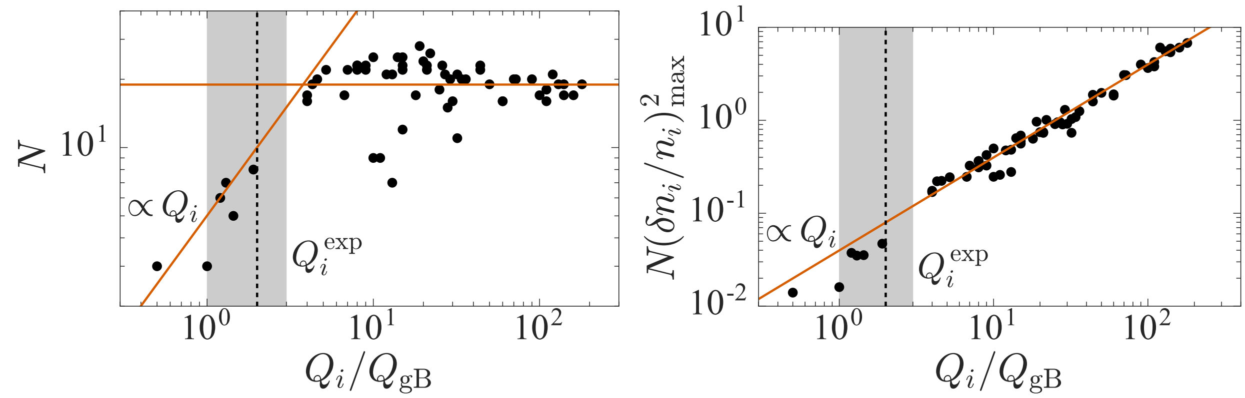

(a) (b)

Figure 19: (a) Number of structures (defined as instance of the perturbed density with an amplitude above 75% of the maximum) versus $Q_i/Q_{\rm gB}$. It grows as $Q_i/Q_{\rm gB}$ increases up to and slightly beyond the experimental value $Q_i^{\rm exp}$. Eventually the volume is filled with structures and their number tends to a constant. The scaling $Q_i \propto N$ is shown for reference. (b) Confirmation of the scaling (18), where the red line indicates a line $\propto Q_i$. We note that simulations near marginality are relatively difficult to saturate leading to the low number of simulations around $Q_i^{\rm exp}$. However, the trend is still clear even for those simulations.

They are generated by nonlinear interactions in the system. Previous work [35] on the transition to turbulence in the case of $\gamma_E = 0$ showed that near the turbulence threshold (approached by varying the equilibrium parameter κ_T), turbulence is regulated by strong zonal flows, which can cause an upshift in the critical κ_T required for a saturated strongly turbulent state. However, in our system, the near-threshold cases the background flow shear plays an important role, and also has a suppressing effect on the turbulence.

Here, we investigate the relative importance of the mean shear and the shear resulting from the self-generated zonal flows. The shear due to the zonal flows $V'_{\rm ZF}$ is calculated from (16) by considering only the poloidally symmetric component, that is

$$V'_{\rm ZF} = \frac{c}{aB_{\rm ref}} \frac{q_0}{r_0} \frac{1}{|\nabla\alpha|} \frac{\partial^2 \varphi_{\rm ZF}}{\partial x^2}, \tag{19}$$

where α is the binormal coordinate, $\varphi_{\rm ZF}$ is the poloidally symmetric component of φ and $V'_{\rm ZF}$ is a function only of t and x. To determine whether the zonal shear will dominate over the mean shear γ_E we calculate the RMS value of the zonal shear, $\gamma_{\rm ZF}$:

$$\gamma_{\rm ZF} = \left\langle V'^2_{\rm ZF} \right\rangle^{1/2}_{t,x}, \tag{20}$$

where $\langle \cdots \rangle_{t,x}$ indicates an average over t and x. We can now compare $\gamma_{\rm ZF}$ with γ_E to determine their relative size as a function of our equilibrium parameters.

Figure 20(a) shows the ratio of the zonal shear to the flow shear, $\gamma_{\rm ZF}/\gamma_E$, as a function of κ_T and γ_E over the same parameter range as shown in figure 5(a). The magnitudes of $\gamma_{\rm ZF}$ and γ_E are comparable where $\gamma_{\rm ZF}/\gamma_E \sim 1$, which is indicated by the dashed line. We see that the regime in which $\gamma_{\rm ZF}$ and γ_E become comparable occurs some distance away from

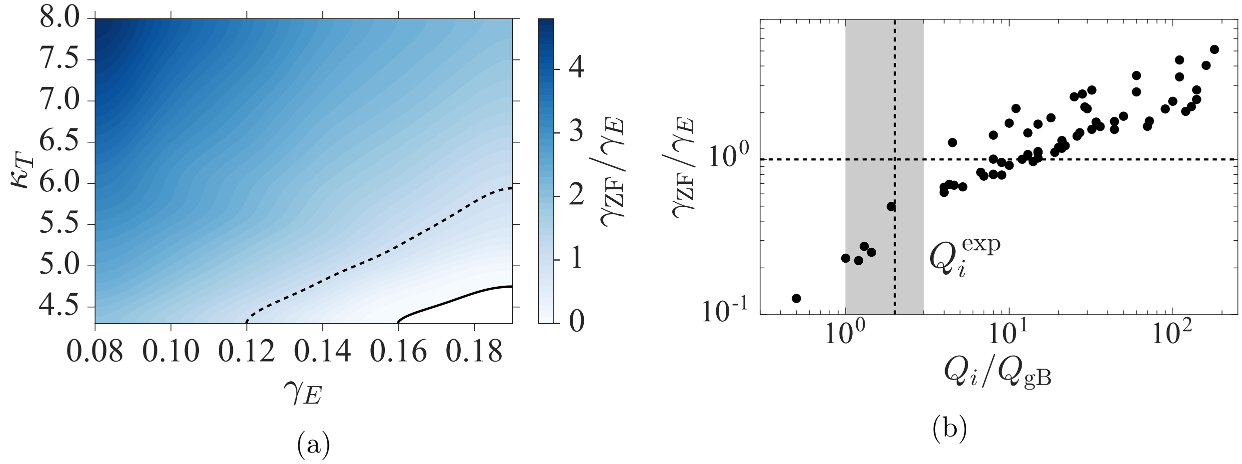

Figure 20: (a) The ratio of zonal shear to mean equilibrium flow shear $\gamma_{\rm ZF}/\gamma_E$ over the same range of κ_T and γ_E as shown in figure 5(a). The zonal shear and mean flow shear are comparable when $\gamma_{\rm ZF}/\gamma_E \sim 1$. The white region in the lower right-hand corner, separated by a solid line, indicates the region where there is no turbulence, i.e., $Q_i = 0$ [see figure 5(a)], and the dashed black line indicates $\gamma_{\rm ZF}/\gamma_E = 1$. (b) $\gamma_{\rm ZF}/\gamma_E$ as a function of $Q_i/Q_{\rm gB}$. The vertical dashed line indicates the value of the experimental heat flux and the horizontal dashed line indicates $\gamma_{\rm ZF}/\gamma_E = 1$.

the turbulence threshold (solid line). Therefore, close to the threshold (small $\gamma_{\rm ZF}/\gamma_E$), we expect the shear due to the background flow to dominate, while far from the threshold (large $\gamma_{\rm ZF}/\gamma_E$), we expect the shear due to the zonal flows to dominate.

Figure 20(a) suggests that the change in $\gamma_{\rm ZF}/\gamma_E$ is effectively a function of the distance from the turbulence threshold. Figure 20(b) shows this dependence explicitly: $\gamma_{\rm ZF}/\gamma_E$ as a function of $Q_i/Q_{\rm gB}$. The vertical dashed line indicates $Q_i^{\rm exp}/Q_{\rm gB}$ and we see that $\gamma_{\rm ZF}/\gamma_E$ is quite small at this value. This suggests that zonal shear plays a weaker role than γ_E in regulating experimentally relevant turbulence for this MAST configuration. Therefore, near-threshold and far-from-threshold turbulent states are distinguished by whether it is the mean or the zonal shear that plays a dominant role. Far from the threshold, the turbulence is likely similar to conventional ITG-driven turbulence in the absence of background flow shear. This is supported by figure 21, which shows $\gamma_{\rm ZF}$ as a function of γ_E. We see that for low γ_E and/or high κ_T (i.e. for cases far from the threshold), $\gamma_{\rm ZF}$ is approximately independent of γ_E and close to the value that it takes at $\gamma_E = 0$.

3.3.6 Summary

In summary, we can describe the behaviour of the MAST turbulence that we studied as follows. For equilibrium parameters near the turbulence threshold (including for cases that match the experiment), the density and temperature fluctuations (and hence the heat flux) are concentrated in long-lived, intense coherent structures. As the equilibrium parameters (κ_T, γ_E) depart slightly from their critical values into the more strongly driven regime, the number of the coherent structures increases rapidly while their amplitude stays roughly constant (in contrast to the conventional supercritical turbulence, where the amplitude increases with κ_T). Increasing κ_T or decreasing γ_E further leads to the structures filling the simula-

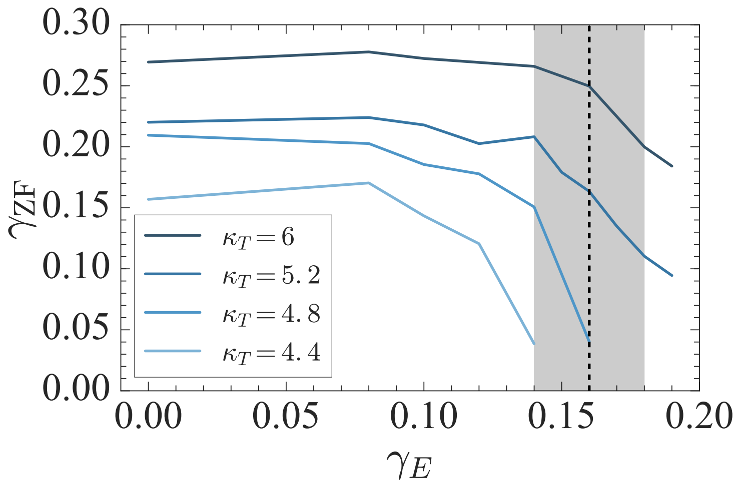

Figure 21: Zonal shear $\gamma_{\rm ZF}$ as a function of background flow shear γ_E showing that zonal shear is comparable between low γ_E (high $Q_i/Q_{\rm gB}$) cases and $\gamma_E = 0$ cases.

tion domain and any further increase in the heat flux is caused by an increase in fluctuation amplitude. The latter regime is similar to the conventional plasma turbulence, where zonal flows are the dominant mechanism for regulating turbulence. In contrast, we have demonstrated that in the near-threshold cases, the zonal shear is small compared to the mean flow shear and so is unlikely to matter.

4 Correlation analysis and comparison with BES

In the previous section, we used nonlinear simulations to demonstrate the complicated nature of the MAST turbulence that we are studying, in particular the details of a subcritical transition to turbulence. In this section, we seek to establish the experimental relevance of our simulations using quantitative comparisons between the fluctuation fields predicted numerically and those measured by the BES diagnostic. We will review the BES diagnostic and experimental results (section 4.2) from Ref. [26], and then present two types of correlation analysis of our nonlinear simulations (the correlation-analysis techniques are described in appendix B). The first analysis will be of GS2 density fluctuations with a "synthetic BES diagnostic" applied to simulate what would be measured by a real BES diagnostic (section 4.3). We will consider the results from nonlinear simulations with values of (κ_T, γ_E) within the experimental-uncertainty range and compare them with the experimental results. The second analysis will be of the raw GS2 density fluctuations, both within the experimental-uncertainty range and, as a function of $Q_i/Q_{\rm gB}$, for our entire parameter scan (section 4.4). In this latter case we will emphasise the extent to which it is the distance from the turbulence threshold rather than individual values of κ_T or γ_E that determines the statistical characteristics of the density fluctuations.

4.1 Beam emission spectroscopy diagnostic

Turbulent eddies in tokamak plasmas are anisotropic due to the strong background magnetic field. In the parallel direction, turbulent eddies have a length scale comparable to the system size, which in a torus is the *connection length* πqR [56], i.e., $l_\parallel \sim \pi qR$ (≈ 6 m for MAST). In the direction perpendicular to the magnetic field, ITG-unstable turbulent structures have a typical length scale of the order of the ion gyroradius $l_\perp \sim \rho_i \sim 1$ cm. Therefore, in the plane perpendicular to the magnetic field, we are interested in two-dimensional measurements of fluctuating quantities at approximately the scale of ρ_i. Beam emission spectroscopy is a diagnostic technique that was developed to address this need. Specifically, the BES diagnostic on MAST [20, 21] is designed to measure ion-scale density fluctuations in a radial-poloidal plane. Density fluctuations are inferred from D_α emission produced by the NBI beam as it penetrates the plasma. The measured fluctuating intensity of the D_α emission is proportional to the local plasma density at the corresponding viewing location, and the two quantities are related via point-spread functions (PSFs) [23, 26, 24]. The PSFs depend on the magnetic equilibrium, beam parameters, viewing location, and plasma profiles and as a result, have to be calculated explicitly for each measurement [23].

Recent work [24], based on a subset of simulations presented here, has shown that the PSFs play an important role in the measurement of turbulence and that the precise form that they take determines a lower bound on the BES resolution as well as affecting the measurement of the turbulent structures and density fluctuation levels – effects that we will also consider in this work. For further details on the MAST BES system the reader is referred to Refs. [20, 21, 23] and, for a detailed study of the effect of PSFs on the measurement of turbulent structures, to Ref. [24].

4.2 Experimental BES results

Before applying the correlation analysis to our simulations, we review the experimental results from MAST discharge #27274 first presented in Ref. [26], to which we will be comparing our own calculation. As discussed in section 2.2, MAST discharge #27274 forms part of a set of three discharges, which together allowed measurement of turbulence correlation properties over the whole outer radius. Figure 22 shows the experimental results obtained for the radial correlation length l_R^{EXP}, the poloidal correlation length l_Z^{EXP}, the correlation time τ_c^{EXP}, and the RMS density fluctuations $(\delta n_i/n_i)_{\mathrm{rms}}^{\mathrm{EXP}}$ as functions of $r = D/2a$. The vertical dashed line in each plot indicates the radius at which our simulations were done and the corresponding values of the correlation parameters. These target experimental values are (after interpolating between the experimental data points):

$$\begin{aligned} l_R^{\mathrm{EXP}} &= 3 \pm 0.4 \text{ cm}, \\ l_Z^{\mathrm{EXP}} &= 14.06 \pm 0.09 \text{ cm}, \\ \tau_c^{\mathrm{EXP}} &= 3.2 \pm 0.4\ \mu\text{s}, \\ \left(\frac{\delta n_i}{n_i}\right)_{\mathrm{rms}}^{\mathrm{EXP}} &= 0.0214 \pm 0.0006. \end{aligned} \tag{21}$$

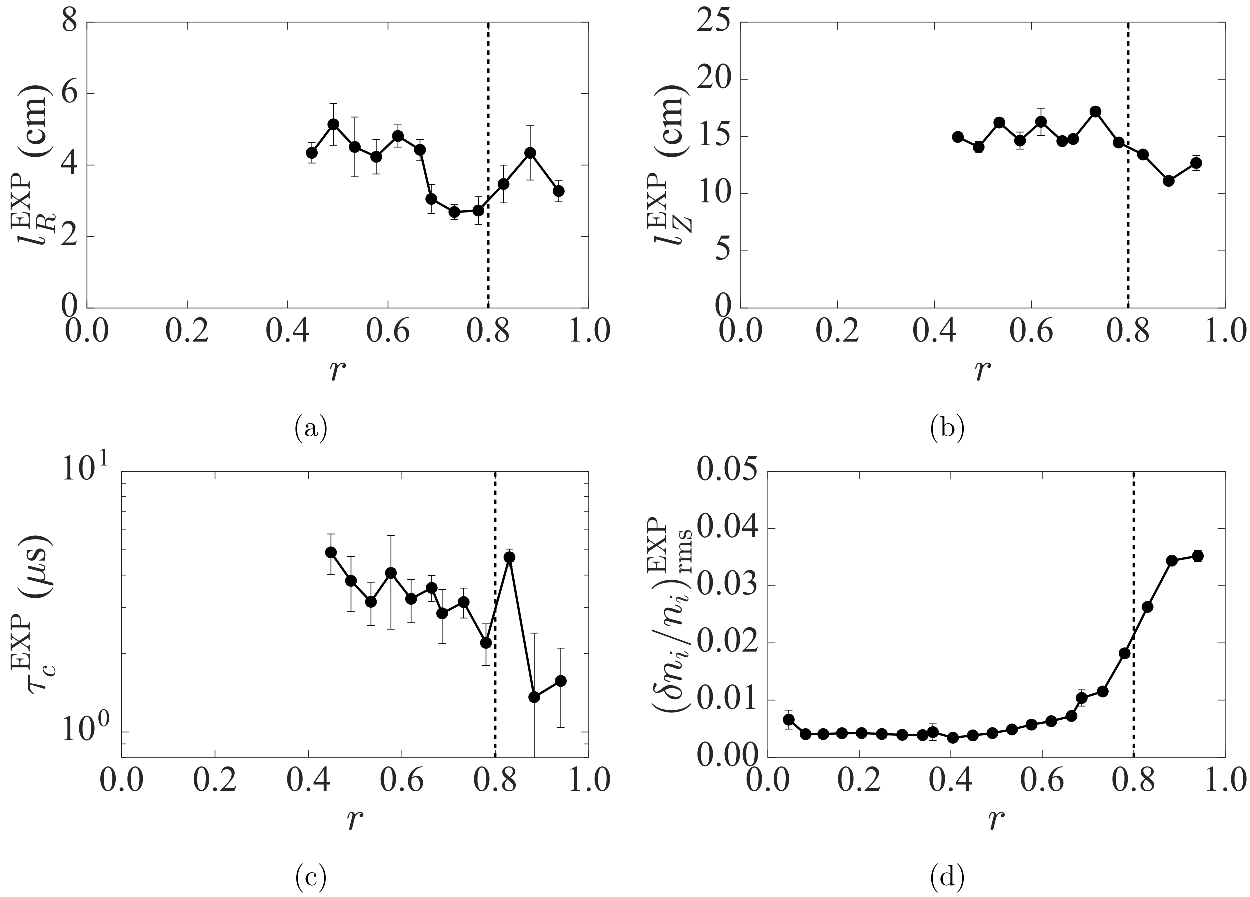

Figure 22: Results of the correlation analysis of BES data from MAST discharges #27272, #27268, and #27274 combined to give correlation properties of the turbulence as functions of $r = D/2a$: (a) radial correlation length l_R^{EXP}, (b) poloidal correlation length l_Z^{EXP}, (c) correlation time τ_c^{EXP}, and (d) RMS fluctuation amplitude $(\delta n_i/n_i)_{\mathrm{rms}}^{\mathrm{EXP}}$. These quantities are defined in appendix B. Turbulence was suppressed for $r \lesssim 0.4$. The vertical dashed line indicates the radius corresponding to the local equilibrium configurations for which we performed our simulations.

We will be comparing the correlation parameters calculated from our simulations in the following sections to those in (21).

4.3 Correlation analysis with synthetic diagnostic

In order to compare our simulated density field with the BES-measured ones, a number of data transformations were necessary. We mapped our density fluctuations "measured" in the outboard midplane (at $\theta = 0$) from GS2 (x, y) coordinates onto a poloidal (R, Z)-plane and also transformed them from the rotating plasma frame, the frame in which our simulations were performed, to the laboratory frame, as explained in appendix C. We then applied a synthetic diagnostic to our density fluctuations, including the point-spread functions (described in section 4.1), which models instrumentation effects and atomic physics, adds artificial noise similar to that found in the experiment, and maps the density-fluctuation field onto an 8×4 grid similar to the arrangement of BES channels. An important feature of the analysis of experimental data is the application of a filter to remove high-energy radiation present in the experiment. We have included this filter for consistency with experimental measurements. The results *without* this filter are presented in appendix E.

Figure 23 shows the radial correlation length l_R^{SYNTH}, poloidal correlation length l_Z^{SYNTH}, correlation time τ_c^{SYNTH}, and RMS density fluctuation $(\delta n_i/n_i)_{\mathrm{rms}}^{\mathrm{SYNTH}}$ calculated from our simulations with the synthetic diagnostic applied using the correlation analysis described in appendix B. We expect these values to agree with the experimentally measured correlation parameters in (21) because the equilibrium parameters κ_T and γ_E at which the results shown in figure 23 were obtained are strictly within the experimental-uncertainty range of these parameters. The dashed lines and shaded areas in figure 23 indicate the experimental values and associated errors given in (21). The circled points indicate the simulations that matched the experimental level of heat flux (listed in table 2).

Examining figure 23(a), we see that the values of l_R^{SYNTH} are clustered around 2 cm and below the experimental BES measurement $l_R^{\mathrm{EXP}} = 3 \pm 0.4$ cm. The approximate resolution limit in the radial and poloidal directions is ~ 2 cm, the physical separation between BES channels [20]. More recent work studying the measurement effect of the PSFs, concluded that the radial resolution limit can be between 2 and 4 cm depending on the orientation of the PSFs for a given configuration [24]. It is, therefore, likely that the results shown in figure 23(a) simply confirm the radial resolution limit of the experimental analysis and the true value of l_R may be lower than 2 cm (as suggested in appendix B.1). We will confirm this in section 4.4, where we consider the correlation properties of the raw GS2 density fluctuations.

Figures 23(b)–(d) show $l_Z^{\mathrm{SYNTH}} = 10$–$15$ cm, $\tau_c^{\mathrm{SYNTH}} = 2$–$15$ μs, and $(\delta n_i/n_i)_{\mathrm{rms}}^{\mathrm{SYNTH}} \sim 0.005$–$0.03$. We see that these values match experimental measurements (21) for certain combinations of κ_T and γ_E. The values of l_Z^{SYNTH} are scattered around the experimental value $l_Z^{\mathrm{EXP}} = 14.06 \pm 0.09$ cm, showing no clear trend. While none of the cases that match the experimental heat flux (circled cases) match l_Z^{EXP}, there are several simulations within the experimental-uncertainty ranges of κ_T and γ_E that do. Similarly, there are several values of τ_c^{SYNTH} that also match τ_c^{EXP}, including two cases that match the experimental level of heat flux. This is a considerable improvement over previous nonlinear gyrokinetic simulations of this MAST discharge [26], which overpredicted τ_c^{SYNTH} by two orders of magnitude.

Examining figure 23(d), we see that $(\delta n_i/n_i)_{\mathrm{rms}}^{\mathrm{SYNTH}}$ increases with increasing κ_T or decreasing γ_E and that increasing γ_E leads to a increase in the value of κ_T required to achieve the same $(\delta n_i/n_i)_{\mathrm{rms}}^{\mathrm{SYNTH}}$. The latter trend is consistent with figure 6(a), which showed that increasing γ_E shifted the nonlinear turbulence threshold to higher κ_T. While figure 23(d) shows that there is agreement between $(\delta n_i/n_i)_{\mathrm{rms}}^{\mathrm{SYNTH}}$ and $(\delta n_i/n_i)_{\mathrm{rms}}^{\mathrm{EXP}}$ at certain combinations of (κ_T, γ_E), we see that the circled cases, representing simulations that match the experimental heat flux, have values of $(\delta n_i/n_i)_{\mathrm{rms}}^{\mathrm{SYNTH}}$ well below $(\delta n_i/n_i)_{\mathrm{rms}}^{\mathrm{EXP}}$.

We conclude from the above results that local gyrokinetic simulations are a reasonable approximation to the experimental turbulence. We showed that l_Z^{SYNTH} and τ_c^{SYNTH} showed reasonable agreement with the experimental measurements within the experimental-uncertainty ranges, while there was a discrepancy in the predictions of l_R^{EXP} and $(\delta n_i/n_i)_{\mathrm{rms}}^{\mathrm{EXP}}$. Thus, at least as far as BES measurements are concerned, the experimental turbulence and the synthetic turbulence are comparable.

One phenomenon that was not present in our simulations but is present in the experiment

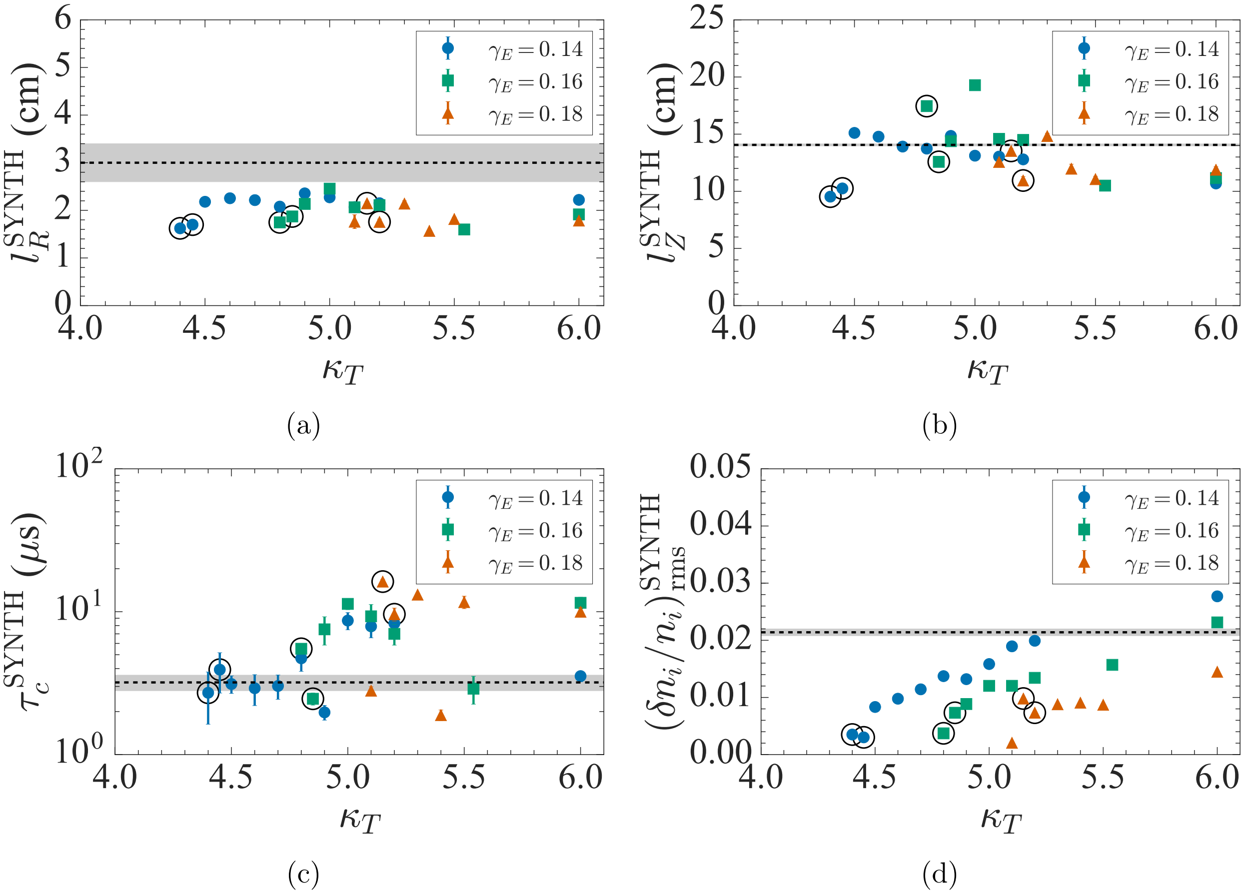

Figure 23: Comparison of correlation parameters obtained via synthetic BES measurements of GS2-simulated density field: (a) radial correlation length l_R^{SYNTH}, (b) poloidal correlation length l_Z^{SYNTH}, (c) correlation time τ_c^{SYNTH}, and (d) RMS fluctuation amplitude $(\delta n_i/n_i)_{\mathrm{rms}}^{\mathrm{SYNTH}}$ as functions of κ_T and for several values of γ_E within experimental uncertainty. The circled points indicate the simulations match the experimental heat flux, given in table 2. The dashed lines indicate the experimental values and the shaded areas the associated error at $r = 0.8$ obtained from interpolating between experimental measurements seen in figure 22, which correspond to the local equilibrium configuration studied in these simulations.

is high-energy radiation (e.g., neutron, gamma ray, or hard X-ray) impinging on the BES detectors. These photons cause high-amplitude spikes in the time series, which are typically confined to a single detector channel and, therefore, uncorrelated with other channels. These radiation spikes then give rise to large auto-correlations at zero time delay, which are unrelated to the turbulent field that is being measured. A numerical "spike filter" is normally used to remove radiation spikes by identifying changes above a certain threshold between one time point and the next, and replacing the high-intensity value with the value of a neighbouring point [21, 57]. This "spike filter" is an important component of the experimental analysis of BES data and, while our simulations do not include spurious sources of radiation, we have included the "spike filter" in the analysis of our simulated density fluctuations for consistency with experimental analysis. The results without the "spike filter" are given in appendix E. These results show little difference to those with the "spike filter" except for the value of

l_Z. We found that in some cases, fast-moving structures in the poloidal direction (especially the long-lived structures found in our simulations close to the turbulence threshold) were removed by the "spike" filter and, therefore, did not contribute to the poloidal correlation function, resulting in a drop in l_Z. This is an important caveat for a future programme of experimental detections of these structures. For a more detailed discussion, see appendix E.

4.4 Correlation analysis of raw GS2 data

Having considered the structure of turbulence processed through a synthetic BES diagnostic, we now want to investigate the raw GS2 density fluctuations, which will allow us to (i) study the (distorting) effect of the synthetic diagnostic, (ii) study the parallel correlations using GS2 data along the field line, and (iii) consider our entire parameter scan to understand how the structure of turbulence in MAST might change with the equilibrium parameters κ_T and γ_E. This extends the previous analysis and comparison with simulations performed for this MAST discharge [26], which only considered the nominal equilibrium parameters and simulations with a synthetic diagnostic applied. The only operations applied here to the raw GS2 density-fluctuation field output are the transformation to the laboratory frame, as explained in appendix C.1, and the transformation from the GS2 parallel coordinate θ to the real-space coordinate λ, as explained in appendix C.3. Our perpendicular correlation analysis is performed over a square (R, Z)-plane 20×20 cm^2 in size, located at the centre of our computational domain (see appendix C.2). We do this to analyse a region of similar size to that probed by the BES diagnostic and also to avoid the real-space remapping effect at the edges of the radial domain inherent to the GS2 implementation of flow shear (see appendix D).

4.4.1 Correlation parameters for cases within experimental-uncertainty range

We start by considering the correlation analysis results for simulations with values of κ_T and γ_E within the experimental-uncertainty range. Figure 24 shows the radial correlation length l_R^{GS2}, the poloidal correlation length l_Z^{GS2}, the correlation time τ_c^{GS2}, and the RMS density fluctuation $(\delta n_i/n_i)_{\mathrm{rms}}^{\mathrm{GS2}}$ calculated for our GS2 density-fluctuation field. The results shown in figure 24 are for a range of values of κ_T and for $\gamma_E = [0.14, 0.16, 0.18]$, with circled points describing the simulations that match the experimental value of the heat flux.

We find that the radial correlation length is $l_R^{\mathrm{GS2}} \sim$ 1–1.5 cm, increasing with κ_T and decreasing with γ_E. This suggests that l_R^{GS2} has a tendency to increase with Q_i/Q_{gB}, as we will show explicitly later. In comparison with the synthetic-diagnostic results shown in figure 23(a), where $l_R^{\mathrm{SYNTH}} \sim 2$ cm, the true radial correlation length of the turbulence l_R^{GS2} is below 2 cm and, therefore, below the resolution threshold of the BES diagnostic (discussed in section 4.3).

Figure 24(b) shows that the poloidal correlation length is $l_Z^{\mathrm{GS2}} \sim$ 13–20 cm (to be compared with $l_Z^{SYNTH} =$ 10–15 cm), keeping the poloidal wavenumber k_Z^{GS2} fixed to $k_Z^{\mathrm{GS2}} = 2\pi/l_Z^{\mathrm{GS2}}$ (giving $k_Z^{\mathrm{GS2}} \sim$ 30–50 m^{-1}). We see that l_Z^{GS2} decreases rapidly as κ_T is increased from its value at the turbulence threshold. The correlation time [figure 24(c)] is in the range $\tau_c^{\mathrm{GS2}} \sim$ 1–6 μs. Finally, figure 24(d) shows that $(\delta n_i/n_i)_{\mathrm{rms}}^{\mathrm{GS2}} \sim$ 0.01–0.08 and increases with increasing κ_T or decreasing γ_E, i.e., has an upward tendency as the heat flux increases.

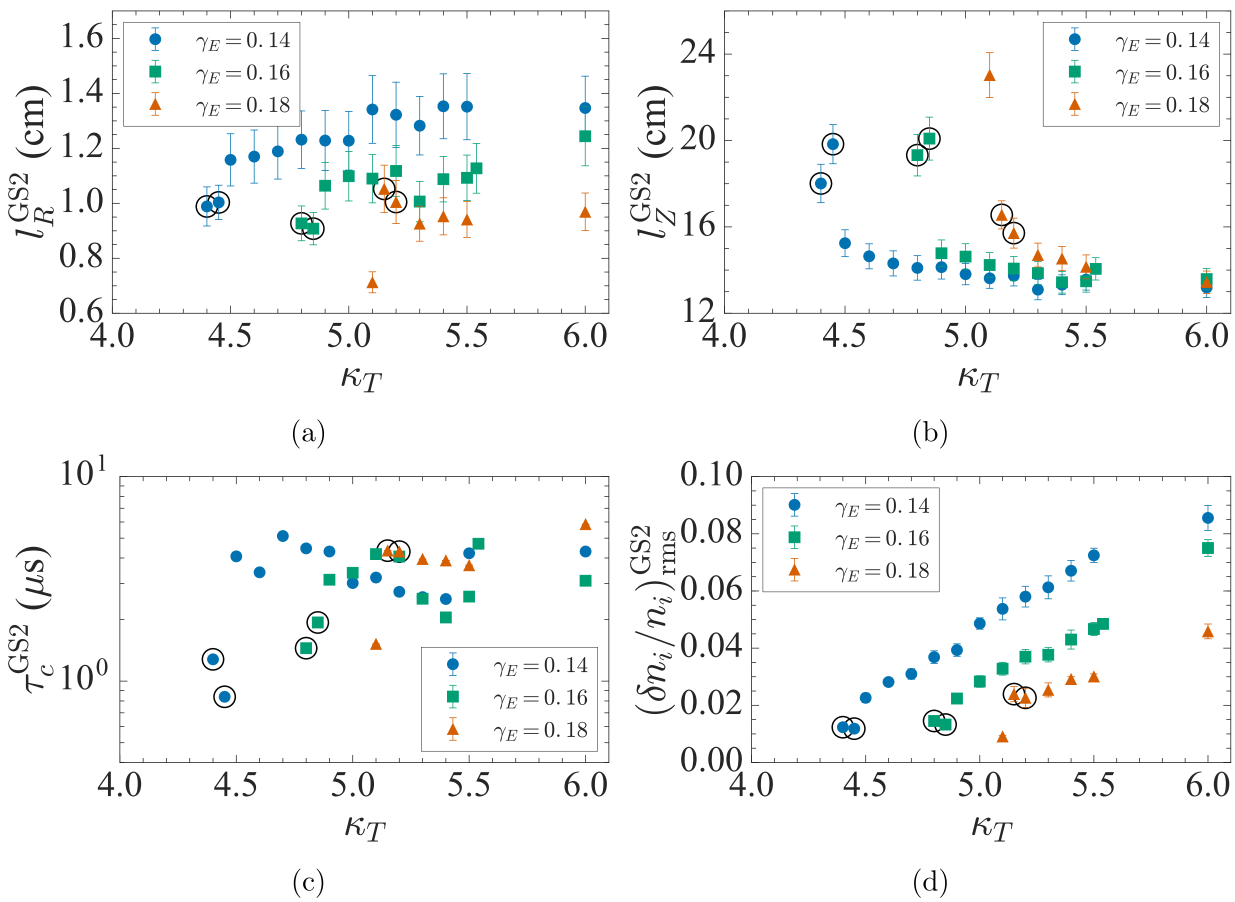

Figure 24: Correlation parameters calculated for raw GS2 density fluctuations for (κ_T, γ_E) within the range of experimental uncertainty indicated in figure 5(a): (a) radial correlation length l_R^{GS2}, (b) poloidal correlation length l_Z^{GS2} keeping k_y fixed to $k_y = 2\pi/l_Z$, (c) correlation time τ_c^{GS2}, and (d) RMS density fluctuations $(\delta n_i/n_i)_{\mathrm{rms}}^{\mathrm{GS2}}$.

4.4.2 Comparisons between experimental and GS2 correlation properties

We have presented the correlation parameters measured (i) by the BES diagnostic in section 4.2, (ii) from GS2 density fluctuations with the synthetic diagnostic applied in section 4.3, and (iii) from the raw GS2 density fluctuations. We show the results from all these analyses in table 3. We can thus summarise the comparison between simulation results and experimental measurements as follows. Comparing the results of the correlation analysis of the GS2 density fluctuations ("SYNTH" and "GS2" in table 3) with the experimental measurements ("EXP"), we see that all the experimental values, except for the radial correlation length l_R, fall within the ranges found for the simulation results. This is particularly important in the case of τ_c, which was significantly overestimated in the previous modelling effort for this MAST discharge [26]. It is clear that the correlation parameters vary with the equilibrium parameters and there is no single simulation, i.e., no single combination of (κ_T, γ_E), that perfectly matches the BES measurements in all four parameters (see figure 24).

Considering the difference between the GS2 density fluctuations with (SYNTH) and without (GS2) the synthetic diagnostic gives us an indication of the effect of the PSFs on

Table 3: Summary of results for the correlation parameters l_R, l_Z, τ_c, and $(\delta n_i/n_i)_{\rm rms}$ from experimental BES measurements (EXP), from the correlation analysis of GS2 density fluctuations with synthetic diagnostic applied (SYNTH; using an identical correlation analysis to that used on the BES data), and from the correlation analysis of raw GS2 density fluctuations (GS2).

Parameter	EXP	SYNTH	GS2
l_R (cm)	3 ± 0.4	1.5–2.5	1–1.5
l_Z (cm)	14.06 ± 0.09	10–15	13–20
τ_c (μs)	3.2 ± 0.4	2–15	1–6
$(\delta n_i/n_i)_{\rm rms}$	0.0214 ± 0.0006	0.005–0.03	0.01–0.08

the measurement of turbulence correlation properties. Given that the value of l_R measured from the raw GS2 density fluctuations is below the approximate resolution threshold, it is unclear what effect the PSFs have on the radial correlation length l_R. We see from table 3 that the ranges of values of the poloidal correlation length l_Z are comparable in the SYNTH and GS2 cases. However, figure 23(b) shows that, with the synthetic diagnostic applied, there are not the clear trends with κ_T that we see in figure 24(b). This may be because the limited poloidal resolution, while sufficient to resolve the measured correlation lengths, is not sensitive enough to recover the trend of decreasing l_Z with κ_T seen in figure 24(b). The measurement of the correlation time τ_c is, again, less certain in the case of the correlation analysis of density fluctuations with a synthetic diagnostic applied, but there is reasonable agreement with the correlation time measured from the raw GS2 density fluctuations. Finally, the application of the synthetic diagnostic leads to a reduction of roughly 50% of the RMS fluctuation amplitude, i.e., from $(\delta n_i/n_i)_{\rm rms}^{\rm GS2} \sim 0.01$–$0.08$ for the raw density fluctuations to $(\delta n_i/n_i)_{\rm rms}^{\rm SYNTH} \sim 0.005$–$0.03$. This observation is consistent with a recent detailed analysis [24] of the effect of PSFs on the measurement of MAST turbulence using a subset of GS2 simulations reported here.

4.4.3 Poloidal and parallel correlation parameters

We now consider two further diagnostics, which were not available to us experimentally: poloidal and parallel correlation functions parametrised by the poloidal and parallel correlation lengths and wavenumbers (defined in appendix B) independently fitted as free parameters (although the poloidal correlation length was calculated previously in section 4.4.1, the resolution of the BES diagnostic necessitated fixing the poloidal wavenumber k_Z).

Figures 25(a) and (b) show the result of such fitting for the poloidal correlations: $l_{Z,\rm free}^{\rm GS2}$ and $k_Z^{\rm GS2}$ versus κ_T. As supported by figure 31 in appendix B.2, we see a roughly 50% decrease in $l_{Z,\rm free}^{\rm GS2}$ compared to $l_Z^{\rm GS2}$ [figure 24(b)], from 13–20 cm to 7–10 cm, again decreasing as κ_T increases or γ_E decreases. Surprisingly, the value of $k_{Z,\rm free}^{\rm GS2}$ is still in the 35–45 m^{-1} range – comparable to one obtained via the fitting procedure where $k_Z = 2\pi/l_Z$. Regardless of the fitting method, figure 24(b) and figure 25(a) show a similar dependence of l_Z on κ_T and γ_E.

The results of the parallel correlation analysis, given in figure 25(c) and (d), are the values $l_\parallel^{\rm GS2}$ and $k_\parallel^{\rm GS2}$ versus κ_T and γ_E. We see that $l_\parallel^{\rm GS2} \sim 6$–$12$ m and decreases with increasing κ_T and decreasing γ_E. Based on this measurement of the parallel correlation length, it is

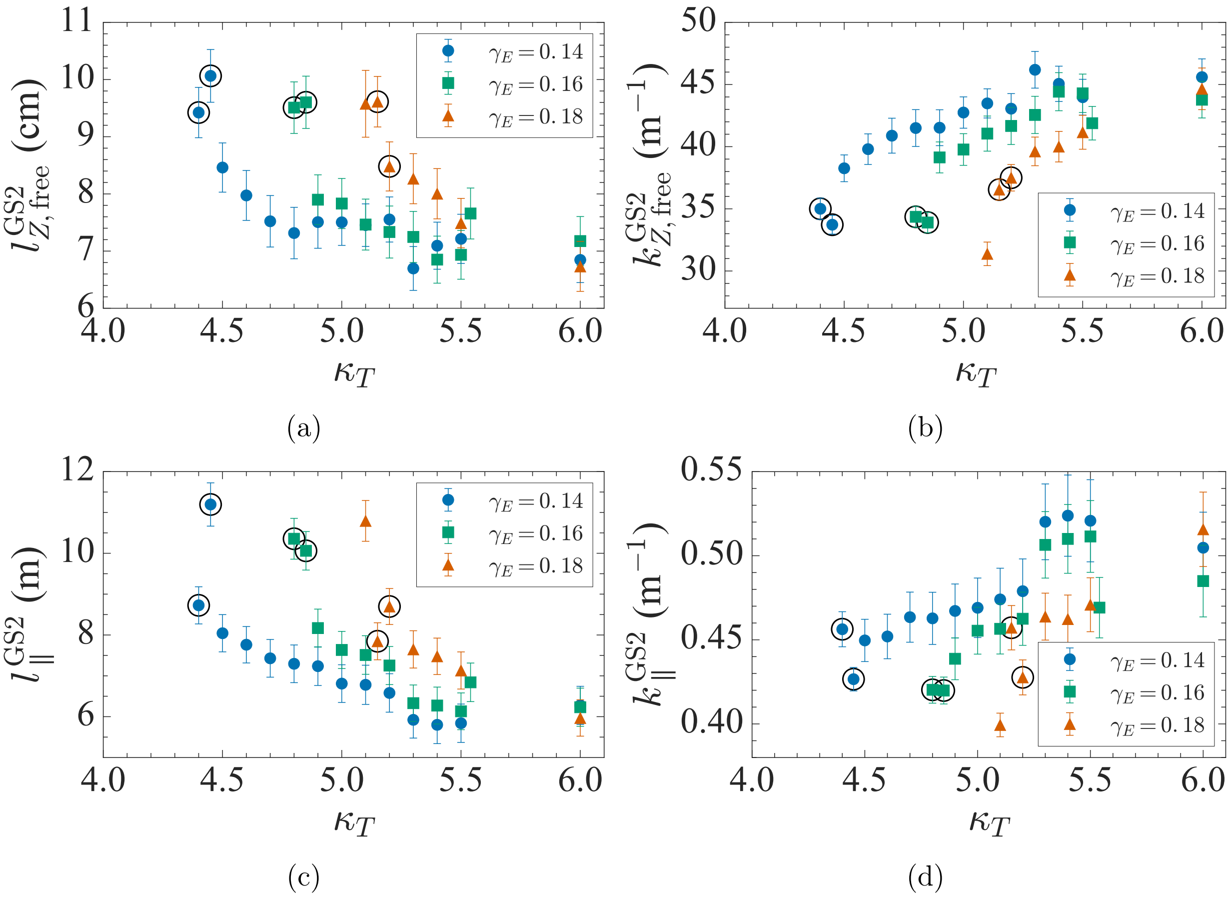

Figure 25: Correlation parameters calculated for raw GS2 density fluctuations for (κ_T, γ_E) within the range of experimental uncertainty indicated in figure 5(a): (a) poloidal correlation length $l_{Z,\mathrm{free}}^{\mathrm{GS2}}$ with k_y as a free fitting parameter, (b) poloidal wavenumber $k_{Z,\mathrm{free}}^{\mathrm{GS2}}$ (section B.2), (c) parallel correlation length $l_{\parallel}^{\mathrm{GS2}}$, and (d) parallel wavenumber $k_{\parallel}^{\mathrm{GS2}}$ (section B.4).

clear that the turbulence is highly anisotropic, i.e., $l_\parallel \gg l_\perp$, as it is expected to be [17].

Using the measurement of $l_{\parallel}^{\mathrm{GS2}}$, we can return to, and confirm, the assumption upon which the calculation of τ_c depends. Namely, in appendix B.3, we assume that reliably estimating the correlation time requires that the temporal decorrelation be dominant over effects due to the finite parallel correlation length [condition (28)]. Using the value of $l_\parallel$ reported above, we estimate $l_\parallel \cos\vartheta / u_\phi \sim 80$–$160\ \mu$s, where we have used the experimental parameters $R = 1.32$ m, $\omega = 4.71 \times 10^4$ s^{-1}, and $\vartheta \approx 0.6$. This confirms that the values of τ_c summarised in table 3 are smaller than $l_\parallel \cos\vartheta / u_\phi$ by more than an order of magnitude and that our time correlation analysis is valid in this MAST configuration.

Currently the BES diagnostic on MAST is not capable of determining both l_Z and k_Z, but the above estimates may be used for future comparisons between experimental measurements and numerical results if higher-resolution BES measurements become available. Similarly, there is currently no diagnostic on MAST capable of measuring the parallel correlation length, but our estimates may guide future attempts at designing diagnostics to measure it.

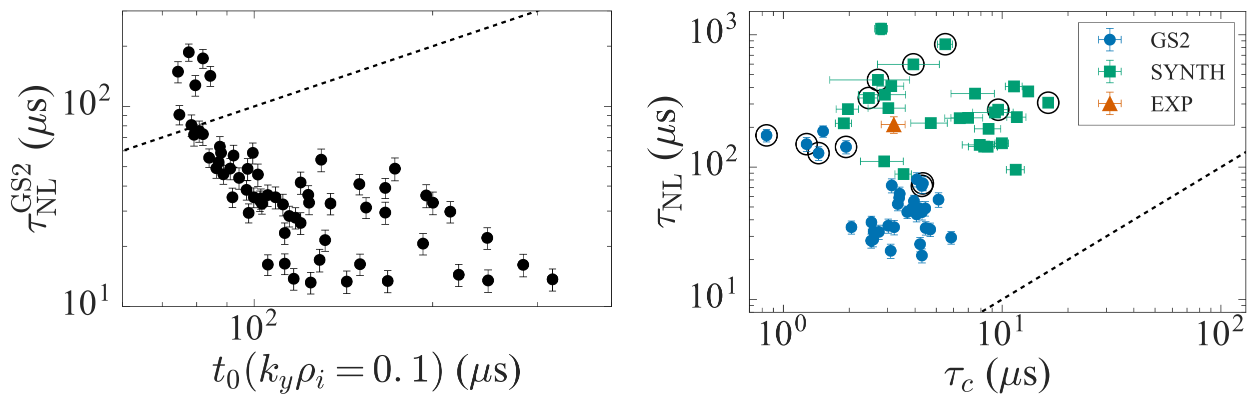

(a) (b)

Figure 26: (a) Nonlinear interaction time of the raw GS2 density fluctuations $\tau_{\rm NL}^{\rm GS2}$, calculated using (22), versus the transient-growth time t_0, defined by (12). We have taken t_0 at $k_y\rho_i = 0.1$, where t_0 is largest (see figure 9). We show here all simulations in our parameter scan with $\gamma_E > 0$. (b) $\tau_{\rm NL}$ versus τ_c for the correlation parameters calculated from the raw GS2 density fluctuations (GS2), from density fluctuations with the synthetic diagnostic applied (SYNTH), and from experimental measurements (EXP). The cases shown are for values of (κ_T, γ_E) within the experimental-uncertainty range and the circled simulations indicate the simulations that match the experimental heat flux. The dashed lines in each plot indicate where the time scales are equal.

4.4.4 Comparison between linear and nonlinear time scales

With the knowledge of the correlation parameters, we can return to the comparison of the transient-growth time t_0 and nonlinear time $\tau_{\rm NL}$ discussed in section 3.2. In particular, we want to determine one of the two conditions for the onset of subcritical turbulence [equation (13)] proposed in [12]. We also want to compare $\tau_{\rm NL}$ with the correlation time of the turbulence τ_c; we then discuss the corresponding experimental results in [26].

The non-zonal nonlinear interaction time is estimated to be [25]:

$$\tau_{\rm NL}^{-1} = \frac{v_{{\rm th}i}\rho_i}{l_R l_Z}\frac{T_e}{T_i}\left(\frac{\delta n_i}{n_i}\right)_{\rm rms}, \tag{22}$$

where we have assumed $l_Z \approx l_y$ (where l_y is the correlation length in the binormal direction as defined in [25]) because $l_Z = l_y \cos\vartheta$, where ϑ is the magnetic field pitch-angle, and $\cos\vartheta \sim 1$ for this magnetic equilibrium. The transient-growth time t_0 was calculated from linear simulations and plotted in figure 9, showing that, at ion scales, the longest transient growth occurred at $k_y\rho_i \sim 0.1$. Figure 26(a) shows $\tau_{\rm NL}^{\rm GS2}$ versus t_0 (at $k_y\rho_i = 0.1$) for all simulations with $\gamma_E > 0$, where the dashed line indicates $\tau_{\rm NL}^{\rm GS2} = t_0$. We see that the majority of simulations are below the line defined by $\tau_{\rm NL}^{\rm GS2} = t_0$, showing that at the very least the condition (13) is approximately satisfied in most turbulent states, i.e., that $t_0 \gtrsim \tau_{\rm NL}$. The inverse relationship between $\tau_{\rm NL}$ and t_0 is explained simply: as the strength of the drive increases and we move away from the turbulence threshold, the growth time of the transient amplification increases, the nonlinear interaction becomes more vigorous, and so the nonlinear time goes down.

Figure 26(b) shows $\tau_{\rm NL}$ versus τ_c for nonlinear simulations with values of (κ_T, γ_E) within experimental uncertainty. The values of $\tau_{\rm NL}$ were calculated from correlation parameters of raw GS2 density fluctuations (GS2), from correlation parameters calculated from GS2 density fluctuations with a synthetic diagnostic applied (SYNTH), and from the experimental BES measurements at $r = 0.8$ (EXP). The dashed line corresponds to $\tau_{\rm NL} = \tau_c$. First, we see that $\tau_{\rm NL} > \tau_c$ for both the GS2 and SYNTH cases, and for the experimental case (EXP). Secondly, $\tau_{\rm NL}$ for the raw GS2 density fluctuations tends to be below the experimental value, whereas the SYNTH cases are comparable. The results shown in figure 26(b) are consistent with the experimental results in [25, 26] that showed $\tau_{\rm NL} \gg \tau_c$ for this and other experimental cases.

It might appear strange that eddies would be able to interact nonlinearly with each other over a much longer time than it takes them to decorrelate. These results suggest either that (22) is a gross overestimate of the nonlinear interactions and/or that the value of τ_c that we measure from the turbulent density field captures some decorrelation process that is otherwise invisible to our synthetic diagnostic ([25] speculated that this might involve zonal flows). However, what is reassuring about these results is that GS2 simulations and BES measurements of turbulence in MAST appear to be consistent with each other in exhibiting this thus far unexplained feature.

4.4.5 Correlation parameters versus $Q_i/Q_{\rm gB}$

The correlation analysis results shown in figures 24 and 25, in particular $l_Z^{\rm GS2}$, $(\delta n_i/n_i)_{\rm rms}^{\rm GS2}$, and $l_\parallel^{\rm GS2}$, exhibit similar trends versus κ_T for different values of γ_E. As we showed in figure 5(a), increasing κ_T or decreasing γ_E effectively amounts to controlling the distance from the turbulence threshold. Furthermore, our investigations of the transition to turbulence (see [14] and section 3.2) and the effect of flow shear on its structure [57] suggest that the key determining factor is the distance from the threshold. This can be quantified by the ion heat flux $Q_i/Q_{\rm gB}$, which increases monotonically with this distance and can be interpreted as an order parameter for our system. Here we describe the results of our correlation analysis of raw GS2 density fluctuations recast as a function of this parameter.

Figures 27 and 28 show the correlation parameters from figures 24 and 25 as functions of $Q_i/Q_{\rm gB}$ for our entire parameter scan, including the cases with $\gamma_E = 0$. These figures support the notion that it is distance from threshold that determines the structure of turbulence and characterise this structure for a realistic MAST configuration and for a large range of $Q_i/Q_{\rm gB}$. We start by discussing the $\gamma_E > 0$ cases.

In figure 27(a), we see a roughly monotonic increase in the radial correlation length $l_R^{\rm GS2}$ with increasing $Q_i/Q_{\rm gB}$, this makes sense because the formation of larger radial structures is one way the turbulence can transport heat more effectively.

Figure 27(b) [along with figures 28(a) and (b)] shows the poloidal correlation length $l_Z^{\rm GS2}$ decreasing with increasing $Q_i/Q_{\rm gB}$. This is consistent with (17) (note that, according to figure 28(b), k_Z, and therefore k_y, increases as l_Z decreases). Though figure 27(b) shows that $l_Z^{\rm GS2}$ decreases to roughly 14 cm for $Q_i/Q_{\rm gB} \sim O(10)$, it starts *increasing* again for $Q_i/Q_{\rm gB} \sim O(100)$. This is perhaps in line with the theoretical and numerical estimates of the scaling of l_Z far from the turbulence threshold predicting that $l_Z \sim q\kappa_T$ [56]. It stands to reason that at such high values of $Q_i/Q_{\rm gB}$, the system is entering a strongly driven regime, but further simulations at higher κ_T are necessary to confirm whether our simulations adhere

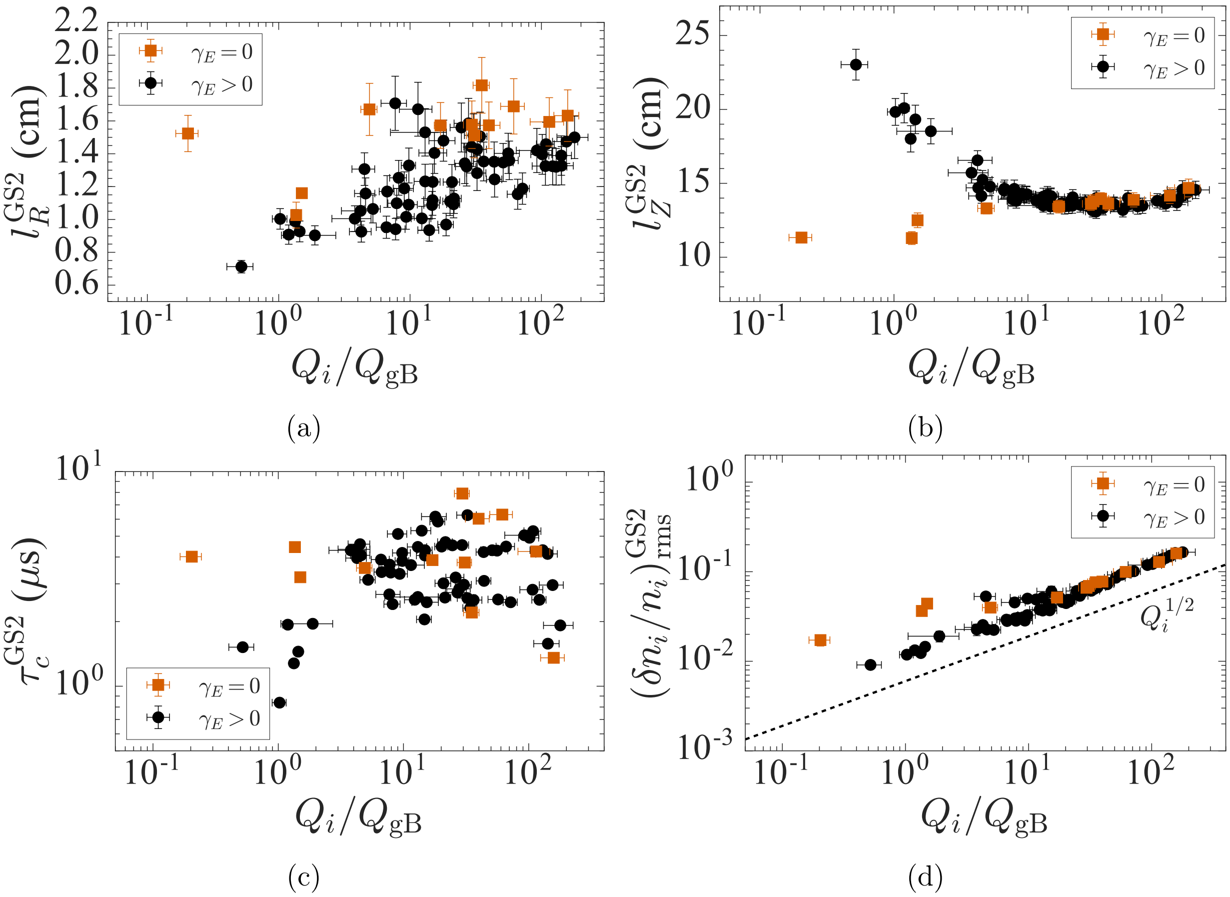

Figure 27: Correlation parameters as functions of Q_i/Q_{gB}, calculated for raw GS2 density fluctuations for the entire parameter scan: (a) radial correlation length l_R^{GS2}; (b) poloidal correlation length; l_Z^{GS2} keeping k_y fixed to $k_y = 2\pi/l_Z$; (c) correlation time τ_c^{GS2}; and (d) RMS density fluctuations $(\delta n_i/n_i)_{\mathrm{rms}}^{\mathrm{GS2}}$, where the dashed line indicates the scaling (17).

to the scaling predicted by [56].

The RMS density fluctuations $(\delta n_i/n_i)_{\mathrm{rms}}^{\mathrm{GS2}}$ shown in figure 27(d) increase as $(Q_i/Q_{\mathrm{gB}})^{1/2}$ far from threshold, as expected from the scaling (17). However, in contrast to the results in figure 17, we do not see a flattening of $(\delta n_i/n_i)_{\mathrm{rms}}^{\mathrm{GS2}}$ at low Q_i/Q_{gB} for $\gamma_E > 0$ cases. This is due to the relatively little volume taken up by the coherent structures and, hence, their small contribution to the RMS value. We verified this by calculating the RMS density fluctuations while excluding varying numbers of the turbulence structures (near the threshold) and found that the RMS value did not change very much, confirming that for the cases near the threshold the RMS value is dominated by the low-amplitude density fluctuations.

Finally, in figure 28(c), we see that the parallel correlation length $l_\parallel^{\mathrm{GS2}}$ decreases towards a constant value as the system is taken away from the turbulence threshold. Theoretical and numerical estimates of $l_\parallel$ for strongly driven ITG turbulence [56] indeed predicted that $l_\parallel$ should be constant and proportional to the connection length, viz. $l_\parallel \sim \pi q R$. This estimate is indicated by the dashed line in figure 28(c) and shows reasonably good agreement with the data.

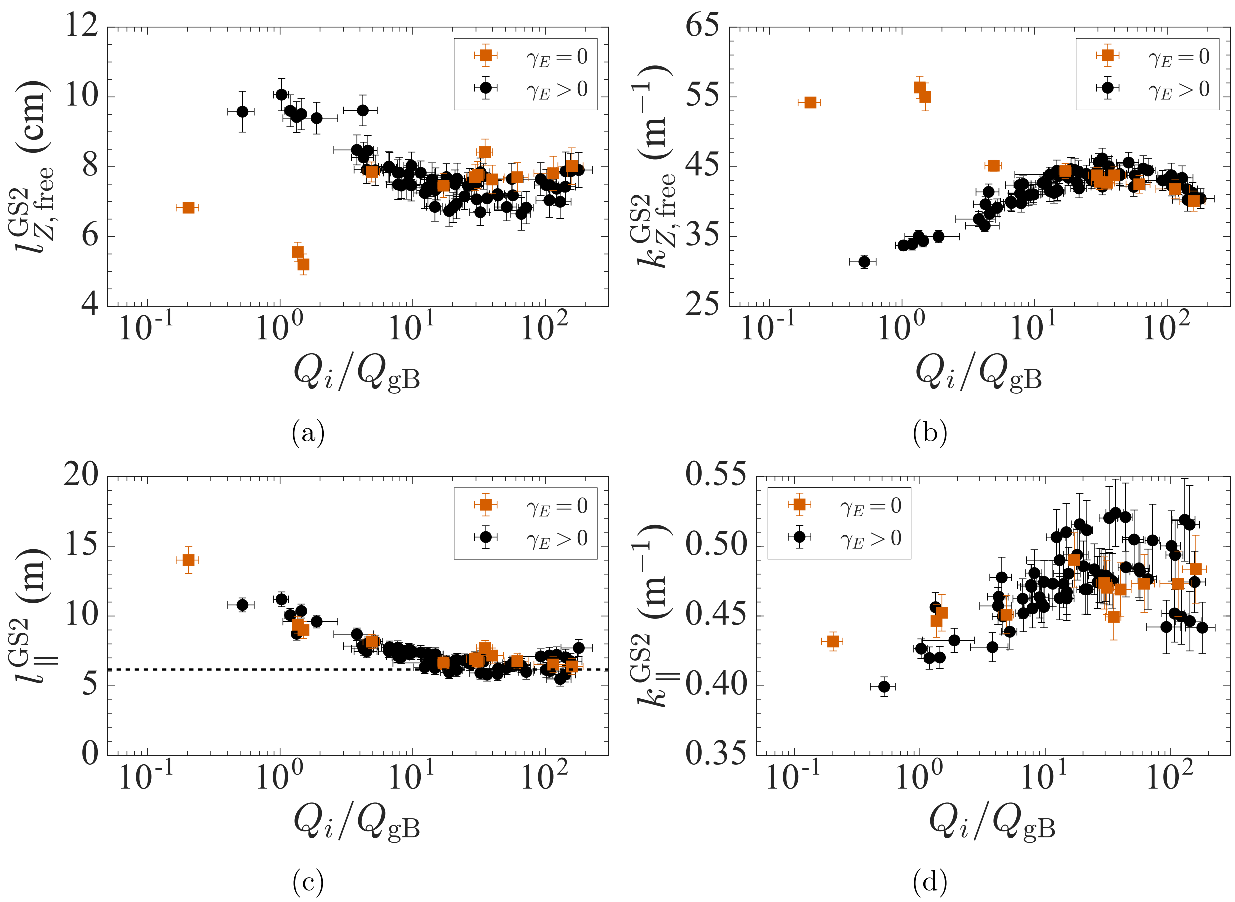

Figure 28: Correlation parameters as functions of Q_i/Q_{gB}, calculated for raw GS2 density fluctuations for the entire parameter scan: (a) poloidal correlation length $l_{Z,\text{free}}^{\text{GS2}}$ with k_y as a free fitting parameter and (b) poloidal wavenumber $k_{Z,\text{free}}^{\text{GS2}}$; (c) parallel correlation length $l_{\parallel}^{\text{GS2}}$ and (d) parallel wavenumber $k_{\parallel}^{\text{GS2}}$. The dashed line in (c) indicates a line of $l_{\parallel} \sim \pi q R$ (see main text and [56]).

We have included both the cases for which $\gamma_E = 0$ (red) and those with $\gamma_E > 0$ (black) in figures 27 and 28 to highlight two important features of unsheared versus sheared turbulence previously discussed in section 3.3. First, close to the turbulence threshold, the cases with $\gamma_E = 0$ represent a different regime of turbulence to those with $\gamma_E > 0$. In particular, l_Z^{GS2} shown in figure 27(b) [as well as in figures 28(a) and (b)], shows an *increasing* trend for cases with $\gamma_E = 0$: from ~ 10 cm near the turbulence threshold (which is significantly lower than the sheared case at the experimentally relevant Q_i/Q_{gB}) to ~ 15 cm far away from the threshold. In contrast, l_Z^{GS2} in cases with $\gamma_E > 0$ *decreases* from ~ 23 cm near marginality to ~ 15 cm far away from it, before starting to increase in a similar trend to the $\gamma_E = 0$ cases. Furthermore, figure 27(c) shows that τ_c^{GS2} predicted by $\gamma_E = 0$ simulations stays roughly constant over a large range of Q_i/Q_{gB} whereas for $\gamma_E > 0$ simulations, τ_c^{GS2} diminishes rapidly for small Q_i/Q_{gB}. Secondly, we see that far from the threshold, the $\gamma_E = 0$ and $\gamma_E > 0$ cases for *all* correlation parameters show the same dependence on Q_i/Q_{gB}. This suggests that far from the threshold there is little difference between sheared and unsheared (by a background flow) turbulence.

The above two observations highlight an important finding of this work: close to the turbulence threshold, the background flow shear has a significant effect on the turbulence leading to reduced heat transport, whereas far from the threshold, the turbulence appears to be similar to the conventional ITG-driven turbulence in the absence of flow shear. This result is consistent with the results in section 3.3 and with the conclusions of the related work in Ref. [57], which argued a similar case in terms of the reflection (up-down) symmetry of the turbulence being broken by the flow shear close to the threshold but effectively restored far from it.

5 Conclusions

We have simulated the plasma microturbulence in an equilibrium configuration corresponding to MAST discharge #27274 using local gyrokinetic simulations and performed a systematic parameter scan in the ITG length scale κ_T and the flow shear γ_E. We demonstrated in section 3.1 that, within experimental uncertainty, our simulations reproduce the experimental ion heat flux, and that the experimentally measured equilibrium gradients lie close to the turbulence threshold inferred from the simulations. This is one of the first numerical demonstrations that a MAST plasma is close to the turbulence threshold. The parameter scan performed in this work has clearly shown that κ_T and γ_E are useful control parameters (and in particular, that experimental values of γ_E do matter for the turbulent state), supporting several previous experimental and numerical studies [49, 37, 58, 7].

We showed in section 3.2 that the system is subcritical for all values of $\gamma_E > 0$, i.e., in the linear approximation, perturbations grow only transiently before decaying, and in the nonlinear system, finite initial perturbations, which we assume are available in the experiment, are required in order to achieve a non-zero saturated state. Subcriticality is a defining feature of this system: for $\gamma_E > 0$, even cases with the largest values of κ_T that we considered required large initial perturbations to ignite turbulence. Using linear and nonlinear simulations, we have estimated the conditions necessary for the onset of subcritical turbulence: we require that maximum transient-amplification factor be $N_{\gamma,\mathrm{max}} \gtrsim 0.4$, and that the transient-growth time t_0 be approximately greater than the nonlinear interaction time, i.e., $t_0 \gtrsim \tau_{\mathrm{NL}}$ (section 4.4.4). These conditions were comparable to those in previous work for simpler geometric configurations [12, 41]. Furthermore, we have showed that the linear dynamics do not change in any quantitatively obvious way as the turbulence threshold is passed, and so nonlinear simulations are essential in predicting the onset of subcritical turbulence and mapping out the turbulence threshold in the parameter space.

Our simulations have shown that, near the turbulence threshold, a previously unreported turbulent state exists in which fluctuation energy is concentrated into a few coherent, long-lived structures, which have a finite minimum amplitude (section 3.3.1). We have argued that this phenomenon is due to the subcriticality of the system, which cannot support arbitrarily small-amplitude perturbations (in contrast to supercritical turbulence). We have investigated the changes in the nature of these nonlinear structures by tracking the maximum fluctuation amplitude (section 3.3.3) and the number of structures (section 3.3.4) as we changed our equilibrium parameters, and have arrived at the following picture of the transition to turbulence. Near the turbulence threshold, the system is comprised of just a few finite-amplitude structures, which are not volume-filling. As the system is taken away from the turbulence threshold, the number of these structures increases (while their amplitude stays the same). Upon increasing in number sufficiently to fill the spatial simulation domain, they begin to increase in amplitude (at a roughly constant number of structures). They also become much less long-lived in time, presumably breaking up against each other as they overlap and interact. Interestingly, this scenario of evolution of our system as it is taken away from the turbulence threshold is reminiscent of the transition to subcritical turbulence via localised structures in pipe flows [59].

We have further shown that, in contrast to conventional ITG-driven turbulence regulated by zonal flows [35] (and their associated shear), in our system, close to the turbulence threshold, the shear due to the mean toroidal flow dominates over the shear due to the zonal flows (section 3.3.5). We have shown that the nominal experimental gradients lie close to the threshold, meaning that it is essential to include the background flow shear in simulations of MAST plasmas. Only reasonably far from the turbulence threshold do the zonal shear and the flow shear due to the background flow become comparable, and further still the turbulence becomes similar to ITG-driven turbulence in the absence of background flow shear (cf. [57]).

We have made quantitative comparisons between density fluctuations in our simulations and those measured by the MAST BES diagnostic [20, 21] (section 4). A correlation analysis [23] was previously performed on the measurements of density fluctuations from the BES diagnostic [26] (section 4.2), focusing on the following properties of the turbulence: the radial correlation length l_R, the poloidal correlation length l_Z, and the correlation time τ_c. We have performed two types of correlation analysis on our simulated density fluctuations: one after applying a synthetic BES diagnostic (section 4.3), and one directly on the raw GS2-generated density fluctuations (section 4.4). We have compared these results to experimental measurements and found reasonable agreement of the correlation lengths, time, and amplitude measurements, except for the radial correlation length, which was predicted by us to be lower than the resolution limit of the BES diagnostic. Notably, the simulated and experimentally measured correlation times were in good agreement, unlike in previous global, gyrokinetic simulations of the same MAST discharge [26].

Finally, we have argued that the nature of the turbulence is effectively a function of the distance from the turbulence threshold. We have quantified this distance from threshold by the magnitude of the ion heat flux Q_i/Q_{gB}, and have shown that it is this quantity, rather than the specific values of the equilibrium parameters κ_T and γ_E, that determines the properties of the turbulence. Throughout this work, we have presented our data as functions of the distance from threshold to highlight the two distinct nonlinear regimes that we have identified: close to the threshold, where coherent structures dominate the dynamics, and far from the threshold, where the turbulence appears to be similar to conventional strongly driven ITG turbulence in the absence of flow shear (e.g. [35, 9]). The experiment appears to be located at the boundary of these two regimes in parameter space. This suggests that this boundary is the most experimentally relevant one, as opposed to the boundary separating the laminar and turbulent states—the so-called "zero-turbulence manifold" [41].

Using the local gyrokinetic code GS2, we have been able to reproduce both the experimental heat flux and the quantitative measurements of turbulence obtained using the BES diagnostic. This should perhaps give some credence to the conclusion from the simulations that do not (yet) have direct experimental backing. More broadly, this should serve to increase one's confidence in the future use of local gyrokinetic simulations in predicting turbulence and transport in high-aspect-ratio spherical tokamaks such as MAST.

A key open question that results from this study is of the experimental existence of the long-lived, coherent structures near the turbulence threshold. Recent work on this topic provided some tentative but encouraging indications that such a regime might manifest itself in terms of experimentally observed skewed probability distributions of density fluctuations [57]. More extensive analysis of MAST BES measurements, and indeed more BES measurements are needed in future to identify these structures, if they do indeed exist.

Acknowledgements

We would like to thank M. Barnes, J. Ball, G. Colyer, and M. Fox for many useful discussions. Our simulations were carried out using the HELIOS supercomputer system at International Fusion Energy Research Centre, Aomori, Japan, under the Broader Approach collaboration between Euratom and Japan, implemented by Fusion for Energy and JAEA. Further computational resources were in part provided by the Plasma HEC Consortium (EP/L000237/1), the Collaborative Computational Project in Plasma Physics funded by UK EPSRC (EP/M022463/1), and the RCUK Energy Programme (EP/1501045). This work has been carried out within the framework of the EUROfusion Consortium and has received funding from the Euratom research and training programme 2014-2018 under grant agreement No 633053 and from the RCUK Energy Programme [grant number EP/P012450/1]. The views and opinions expressed herein do not necessarily reflect those of the European Commission. AAS's work was funded in part by grants from UK EPSRC and STFC.

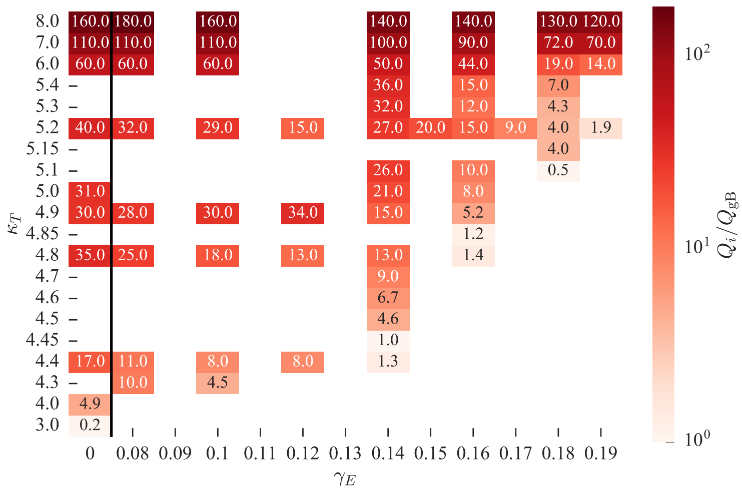

Figure 29: Ion heat flux Q_i/Q_{gB} as a function κ_T and γ_E explicitly showing the values of Q_i/Q_{gB}. Figure 5(a) is a smoothed version of this figure.

Appendices

A Full parameter scan

Our parameter scan in the equilibrium parameters κ_T and γ_E covered approximately $\kappa_T \in [3.0, 8.0]$ and $\gamma_E \in [0, 0.19]$, and consisted of approximately 76 simulations. Figure 29 shows the parameter values of κ_T and γ_E that we simulated, and the associated ion heat flux Q_i/Q_{gB}. To produce figure 5(a), we interpolated between the parameter values in figure 29.

B Correlation analysis

In this section, we give an overview of the correlation-analysis techniques used in Refs. [25, 26], which motivated the experimental comparisons presented in this paper. We will also present an alternative measurement of the poloidal correlation length l_Z, taking advantage of the increased resolution available in the poloidal direction from our simulations. While there is no experimental estimate of the parallel correlation length $l_\parallel$ available from the BES data, we are able to use the three-dimensional data available from GS2 to extend the correlation analysis to the parallel direction (see section 4.4.3).

The two-point spatio-temporal correlation function is defined to be

$$C(\Delta R, \Delta Z, \Delta\lambda, \Delta t) = \frac{\langle \delta n_i/n_i(R, Z, \lambda, t)\delta n_i/n_i(R+\Delta R, Z+\Delta Z, \lambda+\Delta\lambda, t+\Delta t)\rangle}{\left[\left\langle(\delta n_i/n_i)^2(R, Z, \lambda, t)\right\rangle\left\langle(\delta n_i/n_i)^2(R+\Delta R, Z+\Delta Z, \lambda+\Delta\lambda, t+\Delta t)\right\rangle\right]^{1/2}}, \quad (23)$$

where $\delta n_i/n_i$ is the density-fluctuation field, which has a mean of zero, calculated by GS2 and ΔR, ΔZ, $\Delta\lambda$ are the radial, poloidal, and parallel point separations, Δt is the time lag, and $\langle \ldots \rangle$ is an ensemble average, viz. an average over all possible pairs of points with the same separation and time lag. Note that the ensemble averages in the plane perpendicular to the magnetic field are calculated at $\theta = 0$, i.e., they are not averaged over θ. This is because in the laboratory coordinate system, correlation properties vary strongly with θ owing to the twisting of the magnetic field lines. Here we wish to capture what occurs at the outboard midplane, which is the location of the BES diagnostic. Note also that we divide our data in the time domain into windows of $\sim$ 100–400 μs, and calculate separate ensemble averages in each time window. We define the error bars on our correlation parameters by calculating variances between those values calculated over these time windows.

Instead of calculating the full correlation function (23), we will estimate individual correlation lengths and times (which are defined below) by performing one-dimensional correlation analyses separately in each direction, i.e., we calculate 1D versions of the correlation function (23), with respect to only one of its arguments. All of the representative correlation functions that are plotted in the sections that follow will be for the equilibrium parameters $(\kappa_T, \gamma_E) = (5.1, 0.16)$ over a real-space domain of 20×20 cm^2 (see figure 34).

B.1 Radial correlation length

The radial correlation length l_R is estimated by fitting the correlation function $C(\Delta R, \Delta Z = 0, \lambda(\theta = 0), \Delta t = 0)$ with a Gaussian function:

$$f_R(\Delta R) = \exp\left[-\left(\frac{\Delta R}{l_R}\right)^2\right]. \tag{24}$$

Following [25, 26], this fitting function is adopted on the assumption that fluctuations have no wave-like structure in the radial direction. Unlike in the treatment of experimental data [25, 26], no fitting parameters are necessary here to account for global offsets in density fluctuations, which are usually due to large-scale, global MHD modes: in our simulations, the mean density fluctuation over the whole domain is zero. A representative example of (24) for the radial correlation function is shown in figure 30. The points show the measured correlation function and the red line the fit (24). The ensemble average is over t and Z and we assume that radial correlations do not change with t and Z, i.e., that the system is statistically homogeneous in time and in the poloidal direction. The shaded region in figure 30 indicates the standard deviation calculated over the sum of t and Z. We expect that $C(\Delta R) \to 0$ as $\Delta R \to \infty$ (and similarly for subsequent correlation functions in the other directions).

B.2 Poloidal correlation length

The poloidal correlation length is calculated by assuming wave-like fluctuations in the poloidal direction and fitting $C(\Delta R = 0, \Delta Z, \lambda(\theta = 0), \Delta t = 0)$ with an oscillating Gaussian function of the form

$$f_Z(\Delta Z) = \cos(2\pi k_Z \Delta Z) \exp\left[-\left(\frac{\Delta Z}{l_Z}\right)^2\right], \tag{25}$$

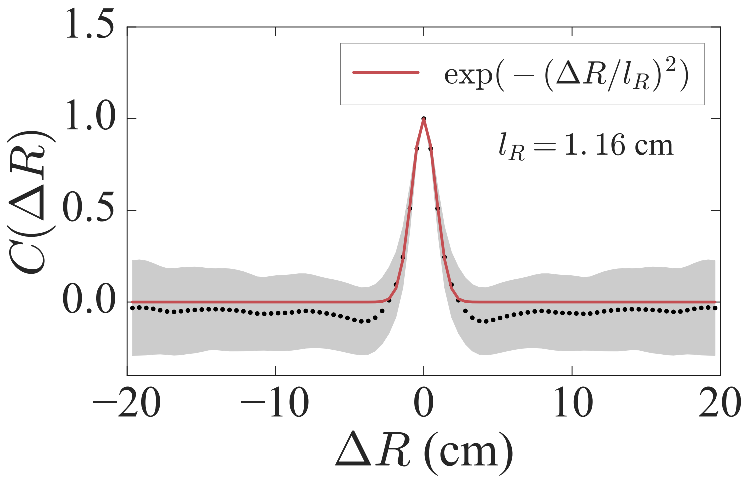

Figure 30: A representative radial correlation function fitted with the function (24) (red line). The points show the measured correlation function $C(\Delta R)$ averaged over t and Z and the shaded region shows the associated standard deviation.

where k_Z is the poloidal wavenumber. Refs. [25, 26] found that with only four poloidal channels, there was insufficient data from the BES diagnostic to fit l_Z and k_Z independently. As a result, when fitting experimental data (and the data with the synthetic diagnostic applied), the wavenumber is fixed to the value $k_Z = 2\pi/l_Z$. In the direct output of our GS2 simulations, on the other hand, there is a sufficient number of data points in the poloidal direction, to allow us to compare fits both with k_Z as a free fitting parameter and fixed in the way described above. Figure 31 shows a representative poloidal correlation function from our simulations along with a fitted function (25), both with fixed $k_Z = 2\pi/l_Z$ [figure 31(a)] and free k_Z [figure 31(b)]. The red lines in each plot indicate the fit (25) and the dashed lines indicate the Gaussian envelope $\exp\left[-(\Delta Z/l_Z)^2\right]$. The ensemble average is over t and R. We see that the fit with k_Z as a free parameter approximates the correlation function better and predicts a shorter l_Z. For consistency with previous work, we show the correlation results for both fitting schemes in section 4.4.

B.3 Correlation time

In the presence of toroidal rotation, turbulent structures are advected in the poloidal direction with an apparent velocity v_Z given by [23]

$$v_Z = R\omega_0 \tan\vartheta, \tag{26}$$

where ϑ is the magnetic-field pitch-angle (the angle that the field line makes with the mid-plane on the outboard side of the flux surface). Following [23], we can use this to calculate the correlation time τ_c by tracking turbulent structures as they move poloidally and measuring their temporal decorrelation. This "cross-correlation time delay" technique [22, 23, 24] is as follows. We calculate the correlation function $C_{\Delta Z}(\Delta t) = C(\Delta R = 0, \Delta Z, \lambda(\theta = 0), \Delta t)$ for several poloidal separations ΔZ, as shown in figure 32. As the structures are advected poloidally, they decorrelate and the peak of the correlation function at a given ΔZ, i.e., the

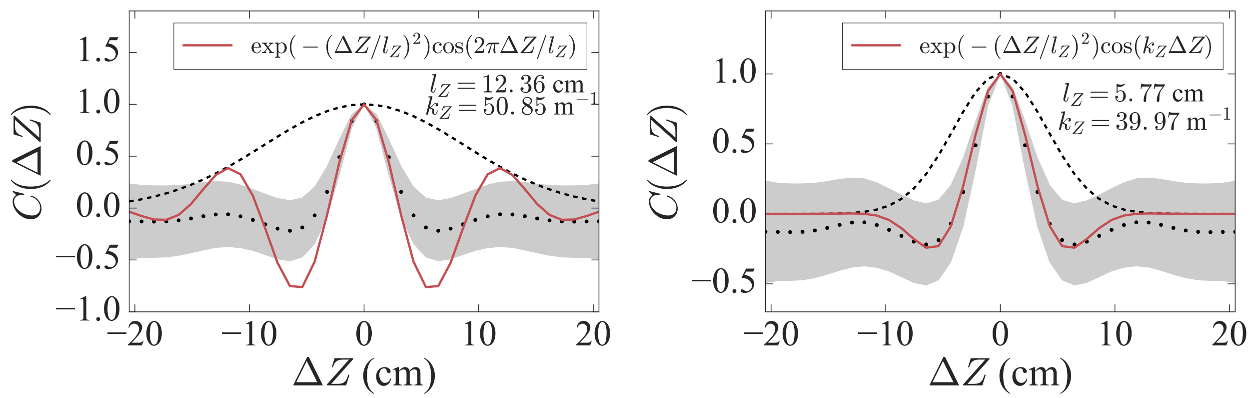

(a)

(b)

Figure 31: Representative poloidal correlation function fitted with the function (25) (red line) keeping the poloidal wavenumber k_Z (a) fixed to $k_Z = 2\pi/l_Z$, (b) as an independent fitting parameter. The points in each plot show the correlation function $C(\Delta Z)$ averaged over t and R and the shaded regions show the associated standard deviation. The dashed lines indicate the Gaussian envelope $\exp\left[-(\Delta Z/l_Z)^2\right]$.

value of $C_{\Delta Z}(\Delta t)$, decreases for increasing ΔZ. The correlation time τ_c is then defined as the characteristic exponential decay time of the peaks of the correlation functions. Namely, we fit $C_{\Delta Z}(\Delta t = \Delta t_{\text{peak}})$ with the function

$$f_\tau(\Delta Z) = \exp\left[-\left|\frac{\Delta t_{\text{peak}}(\Delta Z)}{\tau_c}\right|\right], \tag{27}$$

as shown for a representative correlation function in figure 32, where correlation functions $C_{\Delta Z}(\Delta t)$ for different poloidal separations are shown and the red line shows the fit (27).

This method assumes that the temporal decorrelation dominates over any effects due to the finite parallel correlation length, as we will now explain. While turbulent structures are extended along the field lines, they rotate rapidly in the toroidal direction. After accounting for the apparent poloidal motion, a measurement of the correlation time using data from a single poloidal plane will conflate two separate effect: (i) true decorrelation of turbulent structures in time, and (ii) structures of finite parallel length moving past the measurement point. With only data from a single poloidal plane, these two effects are indistinguishable. In order for the true decorrelation of structures in time (which is what we are interested in) to dominate over the movement of structures past the detector, it must be the case that [25]

$$\tau_c \ll l_\parallel \cos\vartheta / R\omega_0. \tag{28}$$

Since from GS2, unlike from the BES measurements, we can obtain the full 3D turbulence data, we are able to confirm in section 4.4.3 that this condition is indeed satisfied.

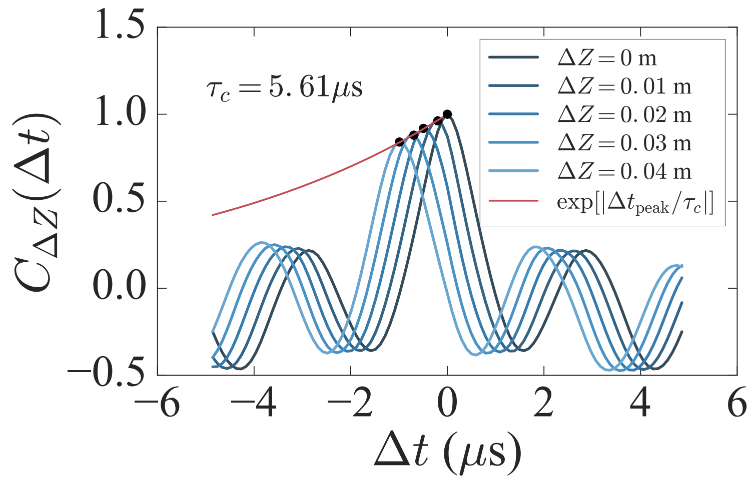

Figure 32: Time correlation functions $C_{\Delta Z}(\Delta t)$ for several poloidal separations ΔZ. The points indicate the maximum value of $C(\Delta t)$ for a given ΔZ, and the red line indicates the function (27) fitted to those points.

B.4 Parallel correlation length

Since GS2 simulations supply the full 3D density-fluctuation field, we are able to study the parallel structure of the turbulence. To do this, we convert the fluctuation field from the GS2 parallel coordinate θ to a real-space coordinate $\lambda(\theta)$ along the field line, as discussed in Appendix C.3. We then calculate the correlation function $C(\Delta R = 0, \Delta Z = 0, \Delta\lambda, \Delta t = 0)$ and take an average over (R, Z, t). We fit the correlation function with an oscillating Gaussian function of the form

$$f_\parallel(\Delta\lambda) = \cos\left(2\pi k_\parallel \Delta\lambda\right) \exp\left[-\left(\frac{\Delta\lambda}{l_\parallel}\right)^2\right], \tag{29}$$

where $k_\parallel$ is the parallel wavenumber. A representative example of the fitting procedure for the parallel correlation function is shown in figure 33, where the red line indicates the fit (29) and the dashed line shows the Gaussian envelope $\exp\left[-(\Delta\lambda/k_\parallel)2\right]$.

B.5 Density-fluctuation amplitude

The final simulation prediction we can compare with the experimental results in [26], is the RMS density fluctuation at the outboard midplane ($\theta = 0$) averaged over (t, R, Z):

$$\left(\frac{\delta n_i}{n_i}\right)_{\text{rms}} = \left\langle \frac{\delta n_i^2(t, R, Z)}{n_i^2} \right\rangle_{t,R,Z}^{1/2}. \tag{30}$$

Formally in gyrokinetics, the quantity $\delta n_i/n_i$ is infinitesimal, and throughout this work, we have written $\delta n_i/n_i$ to mean $(\rho_i/a)\delta n_i/n_i$, i.e., the physical density-fluctuation field predicted by GS2.

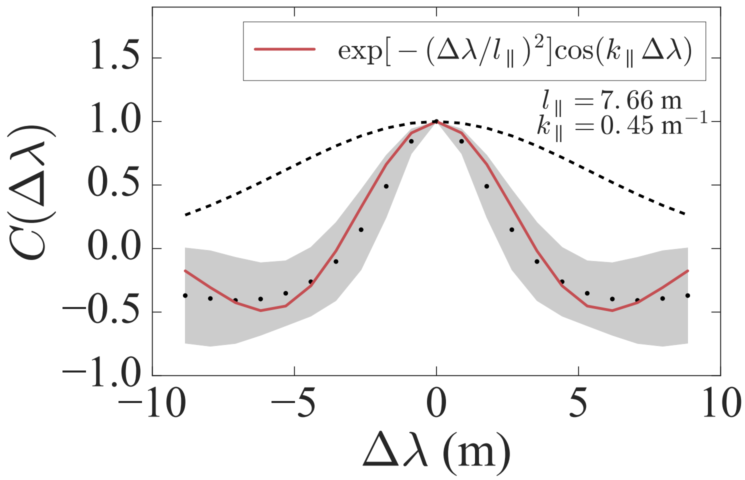

Figure 33: Representative parallel correlation function fitted with the oscillating Gaussian function (29) (red line). The points show the correlation function $C(\Delta\lambda)$ averaged over (t, R, Z) and the shaded region shows the associated standard deviation. The dashed line shows the Gaussian envelope $\exp\left[-(\Delta\lambda/k_\parallel)^2\right]$.

C Transforming to real space and laboratory frame

GS2 solves the gyrokinetic equation (6) in curvilinear coordinates [60] in a domain known as a "flux tube" (see figure 4), which rotates with the plasma. In order to analyse the real-space structure of turbulence and compare with BES measurements, we need to transform our data from the rotating plasma frame to the laboratory frame and from flux-tube geometry to real-space geometry, i.e., from the GS2 coordinates (x, y, θ) to (R, Z, λ) where R is the major radius, Z is poloidal height above the midplane of the machine, and λ is the distance along the field line (not the toroidal direction because correlations are meaningfully long-scale in the direction parallel to the field; see, e.g., [17]).

C.1 Laboratory frame

GS2 simulations are carried out in a frame rotating with the plasma, with toroidal rotation frequency ω_0, whereas the BES diagnostic measures turbulence in the laboratory frame. In order to make realistic comparisons with BES measurements, we applied the following transformation to the GS2-calculated distribution function, to transform from the rotating to the laboratory frame [61]:

$$\left(\frac{\delta n_i}{n_i}\right)_{\mathrm{LAB}}(t, k_x, k_y, \theta) = \left(\frac{\delta n_i}{n_i}\right)_{\mathrm{GS2}}(t, k_x, k_y, \theta)e^{-in\omega_0 t}, \tag{31}$$

where $(\delta n_i/n_i)_{\mathrm{LAB}}$ is the the fluctuating density field calculated by GS2 in the laboratory frame, $(\delta n_i/n_i)_{\mathrm{GS2}}$ is the density field in the rotating plasma frame, and

$$n = k_y\rho_i\frac{\mathrm{d}\psi_N}{\mathrm{d}r}\frac{a}{\rho_i} \tag{32}$$

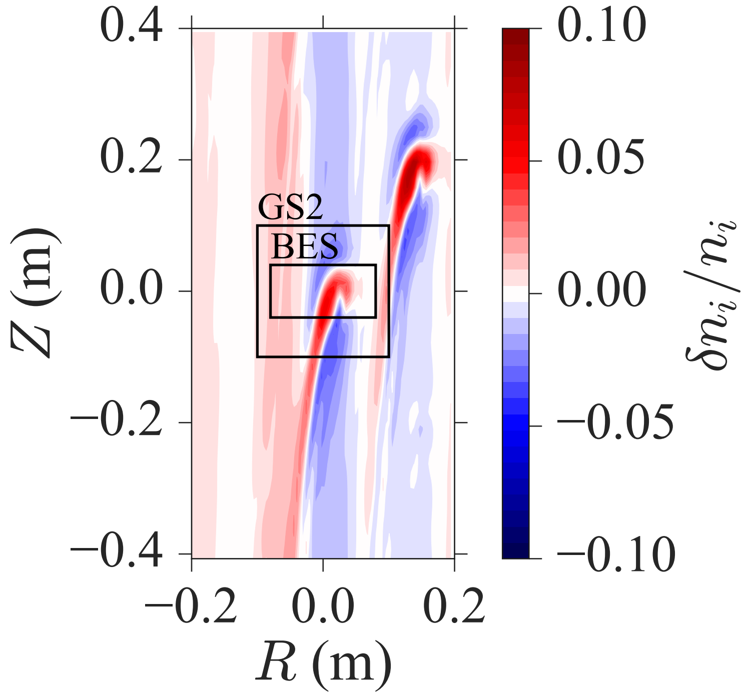

Figure 34: Density-fluctuation field $\delta n_i/n_i$ as a function R and Z for the same near-marginal case as shown in figure 12(a) for the equilibrium parameters $(\kappa_T, \gamma_E) = (4.8, 0.16)$. The indicated domains are those used for the correlation analysis of raw GS2 density fluctuations (GS2) and the approximate size of the BES viewing window (BES).

is the toroidal mode number of a given k_y mode, ψ_N is the normalised poloidal magnetic flux, $r = D/2a$ is the Miller [27] radial coordinate, D is the diameter of the flux surface, a is half the diameter of the last closed flux surface (LCFS), and ρ_i is the ion gyroradius.

C.2 Radial-poloidal domain size

The GS2 flux tube is approximately rectangular at the outboard midplane. Converting from the local GS2 coordinates (x, y) to the radial-poloidal coordinates (R, Z) (the plane of the BES measurement window) is a non-trivial procedure and the reader is referred to [62] for a detailed explanation. Here, we only note that the radial size of the domain is $L_R \approx 0.4$ m and the poloidal size of the domain is $L_Z \approx 0.81$ m. Figure 34 shows the same plot as in figure 12(a) at $\theta = 0$ in terms of the real-space poloidal coordinates R and Z. Also indicated in figure 34 are the domains used for the correlation analysis of BES data and raw GS2 data in sections 4.2 and 4.4, respectively.

C.3 Parallel coordinate

Finally, we calculate the parallel distance along the magnetic field line at the centre of our flux tube. This procedure is non-trivial for a general geometry because a uniform grid in θ does not map to a uniform spatial grid along the field line (as it would have done for circular flux surfaces). For our D-shaped geometry, we want to find $\lambda(\theta)$, the distance along the field

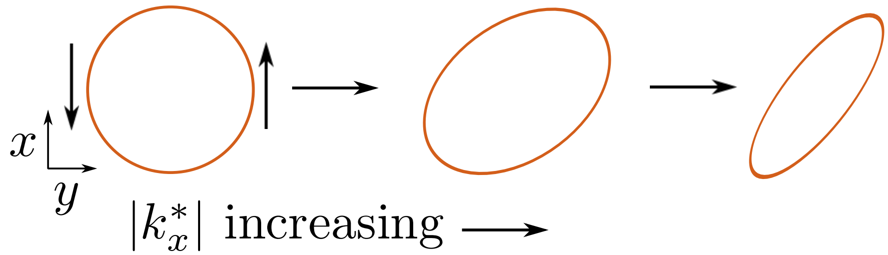

Figure 35: Illustration of the effect of flow shear of turbulent structures. As k_x^* increases in time there is increased radial structure and displacement in the y direction.

line parametrised by the poloidal angle θ. The differential arc length of a line element along the field line in terms of (R, Z, ϕ) is

$$d\lambda^2 = dR^2 + dZ^2 + (Rd\phi)^2, \tag{33}$$

where $R = R(\theta)$ and $Z = Z(\theta)$ are the coordinates of the magnetic field line at the centre of the flux tube, and ϕ is the toroidal angle. Therefore,

$$\lambda(\theta) = \int_0^\theta d\theta' \sqrt{\left(\frac{\mathrm{d}R}{\mathrm{d}\theta'}\right)^2 + \left(\frac{\mathrm{d}Z}{\mathrm{d}\theta'}\right)^2 + \left(R\frac{\mathrm{d}\phi}{\mathrm{d}\theta'}\right)^2}. \tag{34}$$

The quantities $R(\theta)$, $Z(\theta)$, $\mathrm{d}\phi/\mathrm{d}\theta$ are obtained from the specification of the equilibrium and we then calculate their numerical derivatives with respect to θ and then the integral (34) to determine $\lambda(\theta)$. With the knowledge of the real-space parallel grid, we can calculate correlation lengths in the parallel direction.

D Real-space effect of flow shear

Flow shear is implemented in GS2 by allowing the radial wavenumber of each Fourier mode to vary with time [63]:

$$k_x^*(t) = k_x - \gamma_E k_y t, \tag{35}$$

where k_x would be constant radial Fourier mode in the absence of flow shear. In simplified terms, GS2 shifts the fluctuation fields along the k_x dimension as a function of time (see [34] for a complete review of the GS2 flow shear algorithm). This leads to finer radial structure and a displacement of fluctuations in the y direction, as illustrated in figure 35. However, complications arise in this implementation as a result of the fixed k_x grid in GS2, which causes jumps in the displacement of fluctuations in the y direction at the radial extremes of the box as we will now explain.

When k_x^* changes by $\delta k_x = \gamma_E k_y \Delta t$, where Δt is a GS2 time step, the value of the GS2 fluctuation fields at k_x would ideally be shifted to $k_x \pm \delta k_x$. However, the k_x grid is fixed in GS2 (with a grid separation of Δk_x) and so the fluctuation fields cannot be shifted by less than Δk_x. This issue is resolved in GS2 by keeping track of the difference between the exact shift in k_x and the grid spacing Δk_x: when the exact shift is less than $\Delta k_x/2$, no shifting takes place but the value is recorded and added to the size of the shift at the next time step.

This process is repeated until the shift is greater than or equal to $\Delta k_x/2$, at which point all fluctuation fields are shifted by Δk_x. We will now calculate the effect of those shifts.

The distribution function calculated by GS2 is of the form

$$h \propto \exp[i(k_x^* x + k_y y)] = \exp[i(k_x x + k_y y - \gamma_E k_y x t)], \tag{36}$$

where we have substituted for k_x^* using (35). We can identify the wave frequency $\omega_h = \gamma_E k_y x$ to calculate the group velocity

$$\boldsymbol{v}_g = \frac{\partial \omega_h}{\partial \boldsymbol{k}} = -\gamma_E x \hat{\boldsymbol{y}}. \tag{37}$$

Writing $\boldsymbol{v}_g = \Delta y/\Delta t$, we find the local x-dependent displacement of fluctuations in the y direction, for an ideal k_x shift of $\delta k_x = \gamma_E k_y \Delta t$,

$$\Delta y = -\frac{\delta k_x x}{k_y}. \tag{38}$$

However, δk_x is forced to match the fixed k_x grid with the spacing $\Delta k_x = 2\pi/L_x$, where L_x is the size of the box in the x direction. Using $k_y = 2\pi/\lambda_y$, where λ_y is the wavelength of a given k_y mode, we can finally write the displacement due to the flow shear as,

$$\Delta y = \lambda_y \frac{x}{L_x}. \tag{39}$$

This means that at the edges of the radial domain, where $x = \pm L_x/2$, the displacement in the y direction for every shift in k_x due to the flow shear is $\Delta y = \pm\lambda_y/2$. The rate of shifting depends on k_y according to (35) and so the largest modes (smallest k_y's) will be acted on more infrequently than smaller modes (larger k_y's). However, the largest modes are then shifted by half the size of their wavelength according to (39). This causes visual separation (or multiplication) of structures at the edges of the GS2 domain in real space in a way that may affect the correlation analyses performed in section 4. For this reason, we have only analysed an area at the centre of the computational domain, shown in figure 34.

We emphasise that the separation of turbulent structures that we have described above is only present in the real-space representation of the GS2 distribution function. Given that GS2 performs calculations (apart from the calculation of nonlinear interactions) in Fourier space, this does not present a problem to the overall calculation. We note that the implementation of flow shear in GS2 is correct in the limit of infinitely small Δk_x and so it is sufficient to check convergence with Δk_x to be confident of our results. We performed convergence checks by varying Δk_x for a fixed maximum k_x and confirmed that our results were approximately the same. Ideally, some form of interpolation could be used to smooth out these shifts in k_x and a future program of work is planned to implement this in GS2.

E Correlation analysis without the spike filter

An important step in the analysis of experimental data involves the removal of high-energy radiation (e.g., neutron, gamma ray, or hard X-ray) impinging on the BES detector. This

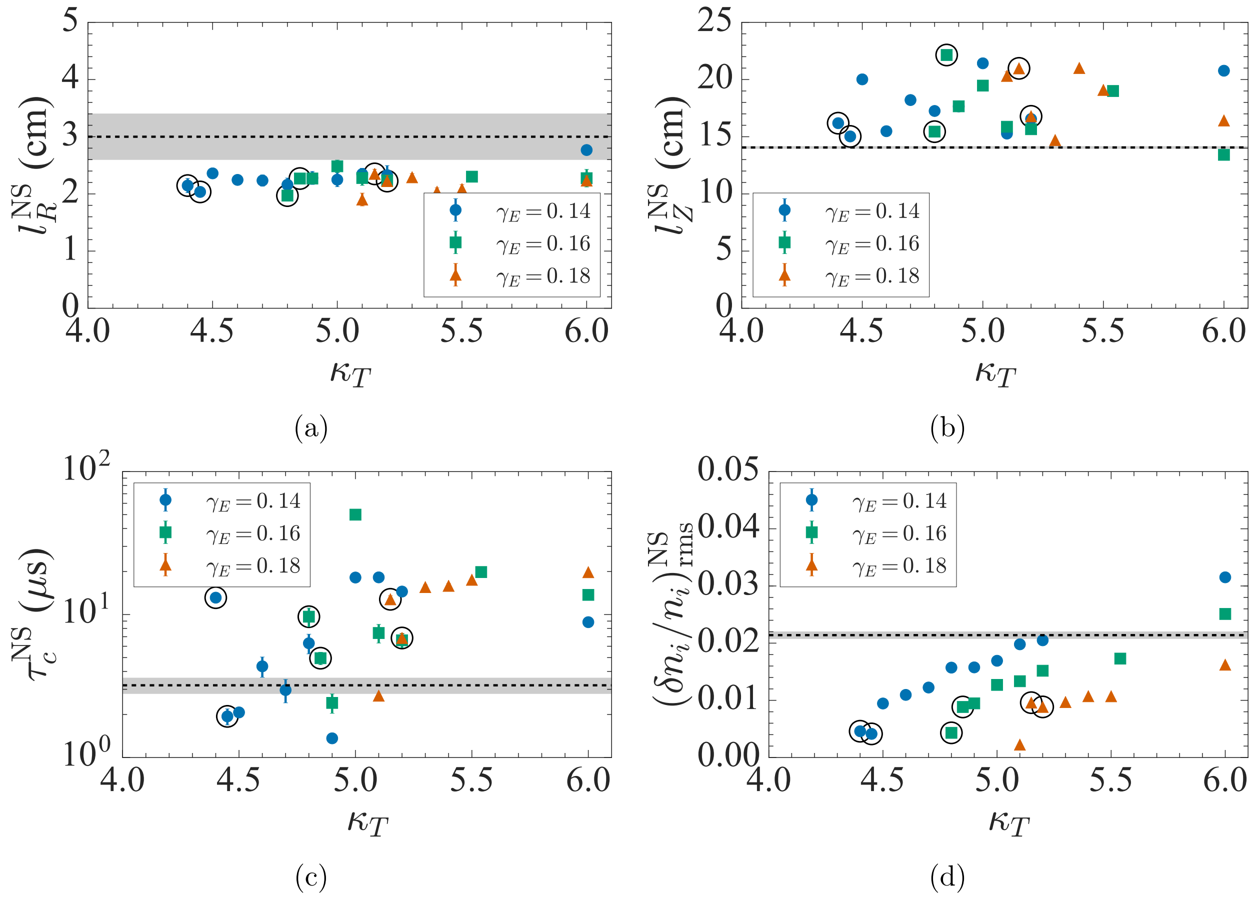

Figure 36: Correlation-analysis results calculated from the analysis of GS2 fluctuation data (within the region of experimental uncertainty) after applying the synthetic diagnostic, but without the spike filter normally applied to experimental data (see figure 23): (a) radial correlation length l_R^{NS} (section B.1), (b) poloidal correlation length l_Z^{NS} (section B.2), (c) correlation time τ_c^{NS} (section B.3), and (d) RMS fluctuation amplitude $(\delta n_i/n_i)_{\mathrm{rms}}^{\mathrm{NS}}$ (section B.5). The simulations that matched the experimental heat flux are circled. The quantities plotted here are discussed in appendix B.

radiation manifests itself as delta-function-like spikes in time, typically only on a single BES channel. These are removed via a numerical "spike filter" [21, 57], which was included in the main analysis (where the synthetic diagnostic was applied; see section 4.3) for consistency with experimental analysis. Here, we show the results of a correlation analysis of GS2 density fluctuations with the synthetic diagnostic applied, but without this spike filter. Figure 36 shows the correlation results for values of κ_T and γ_E within the experimental-uncertainty range: the radial correlation length l_R^{NS} [figure 36(a)], the poloidal correlation length l_Z^{NS} [figure 36(b)], the correlation time τ_c^{NS} [figure 36(c)], the RMS density fluctuation $(\delta n_i/n_i)_{\mathrm{rms}}^{\mathrm{NS}}$ [figure 36(d)].

Comparing these results to the results in section 4.3 with the spike filter, we see that it is mainly the poloidal correlation length that is affected: l_Z^{NS} is several centimetres lower with the spike filter compared to cases without it. We found that in some cases, fast-moving structures in the poloidal direction (especially the long-lived structures found in our near-marginal simulations; see section 3.3.1) were removed by the spike filter and, therefore, did not affect the poloidal correlation function thus copmputed, resulting in a drop in l_Z^{NS}. In particular, figure 36(b) shows that l_Z^{NS} increased significantly in near-marginal simulations compared to its values obtained with the spike filter. This observation of the vulnerability of coherent structures predicted by our simulations to the spike filter should inform future attempts to observe these structures experimentally.

References

[1] K. Krushelnick and S. Cowley. Reduced turbulence and new opportunities for fusion. *Science*, 309:1502, 2005.

[2] C. M. Roach, I. G. Abel, R. J. Akers, W. Arter, M. Barnes, Y. Camenen, F. J. Casson, G. Colyer, J. W. Connor, S. C. Cowley, D. Dickinson, W. D. Dorland, A. R. Field, W. Guttenfelder, G. W. Hammett, R. Hastie, E. G. Highcock, N. F. Loureiro, A. G. Peeters, M. Reshko, S. Saarelma, A. A. Schekochihin, M. Valovic, and H. R. Wilson. Gyrokinetic simulations of spherical tokamaks. *Plasma Phys. Control. Fusion*, 51(12):124020, 2009.

[3] A. R. Field, C. Michael, R. J. Akers, J. Candy, G. Colyer, W. Guttenfelder, Y.-c. Ghim, C. M. Roach, and S. Saarelma. Plasma rotation and transport in MAST spherical tokamak. *Nucl. Fusion*, 51(6):063006, 2011.

[4] B. Coppi, M. N. Rosenbluth, and R. Z. Sagdeev. Instabilities due to temperature gradients in complex magnetic field configurations. *Phys. Fluids*, 10(3):582, 1967.

[5] S. C. Cowley, R. M. Kulsrud, and R. Sudan. Considerations of ion-temperature-gradient-driven turbulence. *Phys. Fluids B*, 3(10):2767, 1991.

[6] T. Dannert and F. Jenko. Gyrokinetic simulation of collisionless trapped-electron mode turbulence. *Phys. Plasmas*, 12(7):1, 2005.

[7] K. H. Burrell. Effects of ExB velocity shear and magnetic shear on turbulence and transport in magnetic confinement devices. *Phys. Plasmas*, 4(5):1499, 1997.

[8] P. J. Catto. Parallel velocity shear instabilities in an inhomogeneous plasma with a sheared magnetic field. *Phys. Fluids*, 16(10):1719, 1973.

[9] M. Barnes, F. I. Parra, E. G. Highcock, A. A. Schekochihin, S. C. Cowley, and C. M. Roach. Turbulent transport in tokamak plasmas with rotational shear. *Phys. Rev. Lett.*, 106(17):175004, 2011.

[10] S. L. Newton, S. C. Cowley, and N. F. Loureiro. Understanding the effect of sheared flow on microinstabilities. *Plasma Phys. Control. Fusion*, 52(12):125001, 2010.

[11] E. G. Highcock, M. Barnes, F. I. Parra, A. A. Schekochihin, C. M. Roach, and S. C. Cowley. Transport bifurcation induced by sheared toroidal flow in tokamak plasmas. *Phys. Plasmas*, 18(10):102304, 2011.

[12] A. A. Schekochihin, E. G. Highcock, and S. C. Cowley. Subcritical fluctuations and suppression of turbulence in differentially rotating gyrokinetic plasmas. *Plasma Phys. Control. Fusion*, 54(5):055011, 2012.

[13] M. Landreman, G. G. Plunk, and W. D. Dorland. Generalized universal instability: transient linear amplification and subcritical turbulence. *J. Plasma Phys.*, 81(05):905810501, 2015.

[14] F. van Wyk, E. G. Highcock, A. A. Schekochihin, C. M. Roach, A. R. Field, and W. Dorland. Transition to subcritical turbulence in a tokamak plasma. *J. Plasma Phys.*, 82(6):905820609, 2016.

[15] E. A. Frieman and L. Chen. Nonlinear gyrokinetic equations for low-frequency electromagnetic waves in general plasma equilibria. *Phys. Fluids*, 25(3):502, 1982.

[16] H. Sugama and W. Horton. Nonlinear electromagnetic gyrokinetic equation for plasmas with large mean flows. *Phys. Plasmas*, 5(7):2560, 1998.

[17] I. G. Abel, G. G. Plunk, E. Wang, M. Barnes, S. C. Cowley, W. D. Dorland, and A. A. Schekochihin. Multiscale gyrokinetics for rotating tokamak plasmas: fluctuations, transport and energy flows. *Rep. Prog. Phys.*, 76(11):105, 2013.

[18] M. Kotschenreuther, G. Rewoldt, and W. M. Tang. Comparison of initial value and eigenvalue codes for kinetic toroidal plasma instabilities. *Comput. Phys. Commun.*, 88(2):128, 1995.

[19] W. Dorland, F. Jenko, M. Kotschenreuther, and B. N. Rogers. Electron temperature gradient turbulence. *Phys. Rev. Lett.*, 85(26):5579, 2000.

[20] A. R. Field, D. Dunai, N. J. Conway, S. Zoletnik, and J. Sárközi. Beam emission spectroscopy for density turbulence measurements on the MAST spherical tokamak. *Rev. Sci. Instrum.*, 80(7):073503, 2009.

[21] A. R. Field, D. Dunai, R. Gaffka, Y.-c. Ghim, I. Kiss, B. Mészáros, T. Krizsanóczi, S. Shibaev, and S. Zoletnik. Beam emission spectroscopy turbulence imaging system for the MAST spherical tokamak. *Rev. Sci. Instrum.*, 83(1):013508, 2012.

[22] R. D. Durst, R. J. Fonck, G. Cosby, H. Evensen, and S. F. Paul. Density fluctuation measurements via beam emission spectroscopy. *Rev. Sci. Instrum.*, 63(10):4907, 1992.

[23] Y.-c. Ghim, A. R. Field, D. Dunai, S. Zoletnik, L. Bardóczi, and A. A. Schekochihin. Measurement and physical interpretation of the mean motion of turbulent density patterns detected by the beam emission spectroscopy system on the Mega Amp Spherical Tokamak. *Plasma Phys. Control. Fusion*, 54(9):095012, 2012.

[24] M. F. J. Fox, A. R. Field, F van Wyk, Y.-c. Ghim, and A. A. Schekochihin. Experimental determination of the correlation properties of plasma turbulence using 2D BES systems. *Plasma Phys. Control. Fusion*, 59(4):044008, 2017.

[25] Y.-c. Ghim, A. A. Schekochihin, A. R. Field, I. G. Abel, M. Barnes, G. Colyer, S. C. Cowley, F. I. Parra, D. Dunai, and S. Zoletnik. Experimental signatures of critically balanced turbulence in MAST. *Phys. Rev. Lett.*, 110(14):145002, 2013.

[26] A. R. Field, D. Dunai, Y.-c. Ghim, P. Hill, B. F. McMillan, C. M. Roach, S. Saarelma, A. A. Schekochihin, and S. Zoletnik. Comparison of BES measurements of ion-scale turbulence with direct gyro-kinetic simulations of MAST L-mode plasmas. *Plasma Phys. Control. Fusion*, 56(2):025012, 2014.

[27] R. L. Miller, M. S. Chu, J. M. Greene, Y. R. Lin-Liu, and R. E. Waltz. Noncircular, finite aspect ratio, local equilibrium model. *Phys. Plasmas*, 5(4):973, 1998.

[28] N. J. Conway, P. G. Carolan, J. McCone, M. J. Walsh, and M. Wisse. High-throughput charge exchange recombination spectroscopy system on MAST. *Rev. Sci. Instrum.*, 77(10):10F131, 2006.

[29] R. Scannell, M. J. Walsh, M. R. Dunstan, J. Figueiredo, G. Naylor, T. O'Gorman, S. Shibaev, K. J. Gibson, and H. Wilson. A 130 point Nd:YAG Thomson scattering diagnostic on MAST. *Rev. Sci. Instrum.*, 81(10):10D520, 2010.

[30] L. L. Lao, H. St. John, R. D. Stambaugh, A. G. Kellman, and W. Pfeiffer. Reconstruction of current profile parameters and plasma shapes in tokamaks. *Nucl. Fusion*, 25(11):1611, 1985.

[31] R. J. Hawryluk. An emperical approach to tokamak transport. In B. Coppi, editor, *Phys. Plasmas Close to Thermonucl. Cond.*, volume 1, page 19. Elsevier, 1981.

[32] I. G. Abel, M. Barnes, S. C. Cowley, W. D. Dorland, and A. A. Schekochihin. Linearized model Fokker–Planck collision operators for gyrokinetic simulations. I. Theory. *Phys. Plasmas*, 15(12):122509, 2008.

[33] M. Barnes, I. G. Abel, W. Dorland, D. R. Ernst, G. W. Hammett, P. Ricci, B. N. Rogers, A. A. Schekochihin, and T. Tatsuno. Linearized model Fokker–Planck collision operators for gyrokinetic simulations. II. Numerical implementation and tests. *Phys. Plasmas*, 16(7):072107, 2009.

[34] E. G. Highcock. The zero turbulence manifold in fusion plasmas. 2012. arXiv:1207.4419.

[35] A. M. Dimits, G. Bateman, M. A. Beer, B. I. Cohen, W. D. Dorland, G. W. Hammett, C. Kim, J. E. Kinsey, M. Kotschenreuther, A. H. Kritz, L. L. Lao, J. Mandrekas, W. M. Nevins, S. E. Parker, A. J. Redd, D. E. Shumaker, R. Sydora, and J. Weiland. Comparisons and physics basis of tokamak transport models and turbulence simulations. *Phys. Plasmas*, 7(3):969, 2000.

[36] E. G. Highcock, M. Barnes, A. A. Schekochihin, F. I. Parra, C. M. Roach, and S. C. Cowley. Transport bifurcation in a rotating tokamak plasma. *Phys. Rev. Lett.*, 105(21):215003, 2010.

[37] P. Mantica, D. Strintzi, T. Tala, C. Giroud, T. Johnson, H. Leggate, E. Lerche, T. Loarer, A. G. Peeters, A. Salmi, S. Sharapov, D. Van Eester, P. C. De Vries, L. Zabeo, and K.-D. Zastrow. Experimental study of the ion critical-gradient length and stiffness level and the impact of rotation in the JET Tokamak. *Phys. Rev. Lett.*, 102(17):1, 2009.

[38] P. Mantica, C. Angioni, C. Challis, G. Colyer, L. Frassinetti, N. Hawkes, T. Johnson, M. Tsalas, P. C. DeVries, J. Weiland, B. Baiocchi, M. N. A. Beurskens, A. C. A. Figueiredo, C. Giroud, J. Hobirk, E. Joffrin, E. Lerche, V. Naulin, A. G. Peeters, A. Salmi, C. Sozzi, D. Strintzi, G. Staebler, T. Tala, D. Van Eester, and T. Versloot. A

key to improved ion core confinement in the JET tokamak: ion stiffness mitigation due to combined plasma rotation and low magnetic shear. *Phys. Rev. Lett.*, 107(13):135004, 2011.

[39] J. Citrin, F. Jenko, P. Mantica, D. Told, C. Bourdelle, R. Dumont, J. Garcia, J. W. Haverkort, G. M. D. Hogeweij, T. Johnson, and M. J. Pueschel. Ion temperature profile stiffness: non-linear gyrokinetic simulations and comparison with experiment. *Nucl. Fusion*, 54:023008, 2014.

[40] L. N. Trefethen, A. E. Trefethen, S. C. Reddy, and T. A. Driscoll. Hydrodynamic stability without eigenvalues. *Science*, 261(5121):578, 1993.

[41] E. G. Highcock, A. A. Schekochihin, S. C. Cowley, M. Barnes, F. I. Parra, C. M. Roach, and W. Dorland. Zero-turbulence manifold in a toroidal plasma. *Phys. Rev. Lett.*, 109(26):265001, 2012.

[42] H. Faisst and B. Eckhardt. Sensitive dependence on initial conditions in transition to turbulence in pipe flow. *J. Fluid Mech.*, 504:343, 2004.

[43] J. Peixinho and T. Mullin. Decay of turbulence in pipe flow. *Phys. Rev. Lett.*, 96(9):094501, 2006.

[44] B. Hof, J. Westerweel, T. M. Schneider, and B. Eckhardt. Finite lifetime of turbulence in shear flows. *Nature*, 443(7107):59, 2006.

[45] K. Avila, D. Moxey, A. de Lozar, M. Avila, D. Barkley, and B. Hof. The onset of turbulence in pipe flow. *Science*, 333(6039):192, 2011.

[46] M. Avila, A. P. Willis, and B. Hof. On the transient nature of localized pipe flow turbulence. *J. Fluid Mech.*, 646:127, 2010.

[47] E. L. Rempel, G. Lesur, and M. R. E. Proctor. Supertransient magnetohydrodynamic turbulence in keplerian shear flows. *Phys. Rev. Lett.*, 105(4):044501, 2010.

[48] R. E. Waltz. Three-dimensional global numerical simulation of ion temperature gradient mode turbulence. *Phys. Fluids*, 31(7):1962, 1988.

[49] A. M. Dimits, T. J. Williams, J. A. Byers, and B. I. Cohen. Scalings of ion-temperature-gradient-driven anomalous transport in tokamaks. *Phys. Rev. Lett.*, 77:71, 1996.

[50] B. N. Rogers, W. Dorland, and M. Kotschenreuther. Generation and stability of zonal flows in ion-temperature-gradient mode turbulence. *Phys. Rev. Lett.*, 85(25):5336–5339, 2000.

[51] S. van der Walt, J. L. Schönberger, J. Nunez-Iglesias, F. Boulogne, J. D. Warner, N. Yager, E. Gouillart, T. Yu, and the scikit-image contributors. scikit-image: image processing in Python. *PeerJ*, 2:e453, 2014.

[52] C. Fiorio and J. Gustedt. Two linear time Union-Find strategies for image processing. *Theor. Comput. Sci.*, 154(2):165, 1996.

[53] R. E. Waltz, G. D. Kerbel, and J. Milovich. Toroidal gyro-Landau fluid model turbulence simulations in a nonlinear ballooning mode representation with radial modes. *Phys. Plasmas*, 1(7):2229, 1994.

[54] Z. Lin, T. S. Hahm, W. W. Lee, W. M. Tang, and R. B. White. Turbulent transport reduction by zonal flows: massively parallel simulations. *Science*, 281(5384):1835–1837, 1998.

[55] P. H. Diamond, S.-I. Itoh, K. Itoh, and T. S. Hahm. Zonal flows in plasma—a review. *Plasma Phys. Control. Fusion*, 47(5):R35, 2005.

[56] M. Barnes, F. I. Parra, and A. A. Schekochihin. Critically balanced ion temperature gradient turbulence in fusion plasmas. *Phys. Rev. Lett.*, 107(11):115003, 2011.

[57] M. F. J. Fox, F. van Wyk, A. R. Field, Y-c Ghim, F. I. Parra, and A. A. Schekochihin. Symmetry breaking in MAST plasma turbulence due to toroidal flow shear. *Plasma Phys. Control. Fusion*, 59(3):034002, 2017.

[58] Ch. P. Ritz, H. Lin, T. L. Rhodes, and A. J. Wootton. Evidence for confinement improvement by velocity-shear suppression of edge turbulence. *Phys. Rev. Lett.*, 65(20):2543, 1990.

[59] D. Barkley, B. Song, V. Mukund, G. Lemoult, M. Avila, and B. Hof. The rise of fully turbulent flow. *Nature*, 526(7574):550, 2015.

[60] M. A. Beer, S. C. Cowley, and G. W. Hammett. Field-aligned coordinates for nonlinear simulations of tokamak turbulence. *Phys. Plasmas*, 2(7):2687, 1995.

[61] C. Holland, A. E. White, G. R. McKee, M. W. Shafer, J. Candy, R. E. Waltz, L. Schmitz, and G. R. Tynan. Implementation and application of two synthetic diagnostics for validating simulations of core tokamak turbulence. *Phys. Plasmas*, 16(5):052301, 2009.

[62] F. van Wyk. Subcritical turbulence in the mega ampere spherical tokamak. 2017. arXiv:1703.03397.

[63] G. W Hammett, W. Dorland, N. F. Loureiro, and T. Tatsuno. Implementation of large scale ExB shear flow in the GS2 gyrokinetic turbulence code. In *APS Meeting Abstracts*, 2006. Presented at the 48th Annual Meeting of the Division of Plasma Physics, Abstract No. VP1.00136.